Membrane Selection and Resistance Characterisation in Hydrogen-Iron Redox Flow Batteries

Integrating Experiments and Modelling

SET3901: Graduation Project

Rishab Gupta

Delft University of Technology



TUDelft

elestor

Membrane Selection and Resistance Characterisation in Hydrogen-Iron Redox Flow Batteries

Integrating Experiments and Modelling

by

Rishab Gupta

Student Number: 6138918

To obtain the degree of Master of Science in
Sustainable Energy Technology
at the Delft University of Technology,
to be defended publicly on the 26th of August 2026 at 1:30 PM.

Academic Supervisor:	Dr. ir. Ruud van Ommen, Professor, Department of Chemical Engineering, TU Delft
Company Supervisor:	Georges Jreij, Stack Architect, Elestor B.V.
External Committee Member:	Dr. Hanieh Bazyar, Assistant Professor, Department of Chemical Engineering, TU Delft
Project Duration:	January 2026 – August 2026
Faculty:	Faculty of Applied Sciences, TU Delft Faculty of Electrical Engineering, Mathematics and Computer Science, TU Delft

TU Delft

elestor

Preface

This report marks the completion of my master's thesis, carried out at TU Delft in collaboration with Elestor B.V., and with it the end of my two-year journey in the Sustainable Energy Technology programme.

First and foremost, I would like to thank my supervisor, Prof. Ruud van Ommen, for taking on this project and guiding me throughout the journey, and for always remaining calm and understanding. I would also like to thank my company supervisor, Georges Jreij, for instilling in me an attitude of critical thinking and for teaching me how to tackle challenges head-on.

My thanks go to all my colleagues at Elestor who contributed to this project, directly or indirectly, including the Decay team. In particular, I would like to thank Marco, who has been a friend, guide, and mentor, always engaged in thoughtful discussion and helping me in more ways than I can count. I am also grateful to Sreeraj, who was instrumental in supporting me across various activities, from operating the stacks to the SEM-EDS measurements. I would also like to thank my friend Sudarshan, who was always there for me throughout these two years and with whom I spent countless hours studying.

Last but not least, I would like to thank my family back home in India: my parents, my aunts, and my siblings, for supporting every decision I made and for never letting me lose hope in times of need.

Rishab Gupta
Delft, August 2026

Summary

Hydrogen–iron redox flow batteries are a promising option for long-duration energy storage, but their performance depends strongly on the ion-exchange membrane. This thesis attempted to develop an integrated experimental and modelling framework to screen membrane candidates, compare their behaviour under HyFe-relevant conditions, investigate retained iron, and evaluate whether an ex-situ-derived resistance-growth coefficient can be translated into an expected resistance under in-situ conditions.

A literature-informed screening procedure selected Nafion NR212, Selemion CMVN, and Membrane X for experimental evaluation. In their respective documented stack configurations, Membrane X and NR212 sustained approximately 477 and $965\ \mathrm{h}$ of cycling. Their apparent beginning-of-charge cell resistances increased by approximately 8% and 29%, respectively. Because the stack configurations and operating histories were not fully matched, these results are interpreted as candidate-level evidence. Within this scope, Membrane X showed the more favourable resistance response. The tested CMVN configuration did not sustain repeatable multi-cycle operation.

Controlled immersion experiments showed that the quantity and time dependence of water-wash-resistant, NaCl-exchangeable retained iron were membrane- and exposure-specific. On a charge-equivalent basis, the results did not indicate a universal preference for either the Fe^{2+}-rich or Fe^{3+}-rich condition. Post-cycling SEM–EDS produced Fe-related signals at selected locations on NR212 and Membrane X, but the measurements were interpreted qualitatively because they did not establish bulk loading, oxidation state, coordination, or through-thickness distribution.

A symmetric H-cell experiment yielded an effective concentration-normalised resistance-growth coefficient of

$$k_{\mathrm{block}} = 1.162 \times 10^{-9}\ \mathrm{m^3\,mol^{-1}\,s^{-1}},$$

with a fit-derived 95% confidence interval of $[1.076,\ 1.248] \times 10^{-9}\ \mathrm{m^3\,mol^{-1}\,s^{-1}}$. When transferred into a data-assisted hybrid $0\mathrm{D}$–$1\mathrm{D}$ transport model, the nominal coefficient captured the principal shape of the normalised Membrane X stack-resistance trajectory ($R^2 = 0.934$, NRMSE $= 6.78\%$). The result supports conditional use of the coefficient as a reduced-order interpretive parameter, but does not constitute an independent prediction of absolute cell resistance or uniquely confirm a microscopic fouling mechanism.

Overall, Membrane X is identified as the preferred candidate for further matched and replicated HyFe evaluation.

Contents

Preface i

Summary ii

List of Figures vi

List of Tables ix

Nomenclature xi

1 Introduction 1
- 1.1 Research Gap . . . 4
- 1.2 Research Questions . . . 5
- 1.3 Research Approach . . . 6
- 1.4 Thesis Outline . . . 6

2 Membrane Performance, Iron Interactions, and Resistance Characterisation in Redox Flow Batteries: A Focused Review 7
- 2.1 Membrane Properties, Material Classes, and Performance Trade-offs . . . 7
- 2.2 The Hydrogen-Iron Redox Flow Battery System . . . 8
- 2.3 Cation-Induced Fouling of Ion Exchange Membranes . . . 9
- 2.4 Other Degradation Phenomena in Redox Flow Batteries . . . 10
- 2.5 Spectroscopic and Elemental Characterisation of Membrane Iron Retention . . . 11
- 2.6 Methods for Resistance Characterisation . . . 11
- 2.7 Modelling Approaches for Membrane Transport and Resistance Evolution . . . 11

3 Experimental and Modelling Methodology 13
- 3.1 Systematic Membrane Screening and Selection . . . 13
  - 3.1.1 Initial Candidate Pool and Chemistry-Relevance Filtering . . . 13
  - 3.1.2 Transport Normalisation and Selectivity-Based Ranking . . . 14
  - 3.1.3 Practical Feasibility Assessment and Final Selection . . . 15
- 3.2 In-Situ Characterisation: Single-Cell Stack Testing . . . 16
  - 3.2.1 Electrolyte Composition and Preparation . . . 16
  - 3.2.2 Stack Assembly . . . 16
  - 3.2.3 Pre-Test Quality Verification . . . 17
  - 3.2.4 Membrane Pre-treatment . . . 18
  - 3.2.5 Operating Conditions and Cycling Protocol . . . 18
  - 3.2.6 Apparent Beginning-of-Charge Resistance Extraction . . . 18
  - 3.2.7 Cycling-Data and Exclusion Criteria . . . 19
- 3.3 SEM-EDS Sample Preparation . . . 20
- 3.4 Ex-Situ Iron Sorption Study: Membrane Immersion Test . . . 20
  - 3.4.1 Membrane pretreatment . . . 20
  - 3.4.2 Electrolyte immersion and iron extraction . . . 21
  - 3.4.3 Iron quantification and data reduction . . . 21
- 3.5 Total Iron Quantification by UV-Vis Spectrophotometry . . . 21
  - 3.5.1 Sample preparation . . . 21
  - 3.5.2 Absorbance measurement and Concentration calculation . . . 22
- 3.6 Ex-Situ Characterisation: H-Cell Resistance-Growth Test . . . 22
  - 3.6.1 Setup Description and Assembly . . . 22
  - 3.6.2 Resistance Evolution in Iron-Containing Electrolyte . . . 24
- 3.7 Water Uptake Measurement . . . 25
- 3.8 Ion Exchange Capacity Measurement . . . 25

3.9 Transport Model: Formulation, Assumptions, and Governing Equations . . . 25
3.9.1 Timescale Separation and Quasi-Steady Membrane Transport . . . 26
3.9.2 Nernst-Planck Transport and Electric-Field Closure . . . 27
3.9.3 Extended-Ideal Donnan Partitioning and Boundary Conditions . . . 28
3.9.4 Zero-Dimensional Inventory Evolution and OCV Assimilation . . . 29
3.9.5 Effective Resistance-Growth State . . . 30
3.9.6 Model Scope, Boundaries, and Assumptions . . . 32

4 Membrane Performance, Retained Iron, Resistance Evolution, and Model-Experiment Comparison 33
4.1 Stack-Cycling Behaviour and Apparent Beginning-of-Charge Resistance . . . 33
4.1.1 Membrane X . . . 33
4.1.2 Nafion NR212 . . . 34
4.1.3 Selemion CMVN . . . 35
4.1.4 Discussion: Comparative Stack-Cycling Behaviour . . . 36
4.2 Post-Cycling SEM-EDS Analysis of Membranes . . . 36
4.2.1 Nafion NR212 . . . 37
4.2.2 Membrane X . . . 39
4.2.3 Discussion: Iron Occurrence and Interpretive Limits of SEM-EDS . . . 40
4.3 Ex-Situ Iron Uptake in Membranes . . . 42
4.3.1 Iron Uptake in Nafion NR212 . . . 42
4.3.2 Iron Uptake in Selemion CMVN . . . 43
4.3.3 Iron Uptake in Membrane X . . . 43
4.3.4 Cross-Membrane Comparison of Retained-Iron Ratios . . . 44
4.4 Resistance Evolution in the H-Cell . . . 44
4.5 Data-Assisted Model Results and Comparison with Experiment . . . 46
4.5.1 Nominal Model-Experiment Comparison . . . 46
4.5.2 Robustness to the Adopted Effective Membrane Ionic Conductivity . . . 48
4.5.3 Model Limitations and Domain of Applicability . . . 50

5 Conclusions and Recommendations 52
5.1 Conclusions . . . 52
5.2 Recommendations . . . 53

References 56

A List of membranes from literature 61

B Model Parameters and Derived Quantities 70
B.1 Holdup Volume . . . 70
B.2 Derivation of H-cell Fe Concentration . . . 70

C Ideal Donnan Equilibrium 72

D Evaluation of Resistance Measurement Techniques for In-Situ Stack Testing 75
D.1 Galvanostatic Polarisation . . . 75
D.2 Electrochemical Impedance Spectroscopy . . . 77
D.3 Summary and Conclusion . . . 82

E MATLAB Code for model 84

F Iron-Cation Interference in NaOH Titration of NaCl Extracts 85
F.1 Dummy-Solution Preparation . . . 85
F.2 Ferric-Iron Interference . . . 86
F.3 Ferrous-Iron and Handling-Dependent Interference . . . 87
F.4 Implication for IEC and Iron-Uptake Measurements . . . 87

G Model Verification: Comparison Against Known Analytical Limits and Exploratory Immobile Sink 89
G.1 Exploratory Mobile-to-Immobilised Iron Sink . . . 92

H Additional data and figures 94

I Declaration of the use of AI tools 105

List of Figures

1.1 Cumulative renewable electricity capacity additions by technology segment across three six-year periods. Adapted from [1], Licence: CC BY 4.0. . . . 1
1.2 Annual number of publications indexed in Scopus under the keyword *energy storage* (title, abstract, and keyword search; journal articles and reviews only), 2015–2025. Data retrieved June 2026. . . . 2
1.3 Annual number of publications indexed in Scopus under the keyword *redox flow battery* (title, abstract, and keyword search; journal articles and reviews only), 2015–2025. Data retrieved June 2026. . . . 3
1.4 The role of improved membranes in redox flow batteries [5]. . . . 3

2.1 Schematic representation of a hydrogen-iron redox flow battery. . . . 8

3.1 Schematic of the membrane screening and selection framework. Candidates are progressively filtered at three stages; those failing each criterion are excluded (dashed red boxes). The final shortlist comprises the three membranes evaluated experimentally in this work: Nafion NR212, CMVN, and Membrane X. . . . 14
3.2 Exploded-view schematic of the single-cell Fe–H_2 stack, showing all functional layers in assembly order. The ion-exchange membrane separates the electrolyte side (bottom) from the hydrogen side (top). . . . 17
3.3 Assembled H-cell used for the symmetric ex-situ resistance-growth experiment. The membrane was sealed between two double-walled glass half-cells using EPDM gaskets. Graphite rods served as the working electrode and the combined counter/reference electrode in the two-electrode impedance configuration. Temperature was controlled using a recirculating bath connected to the double walls. . . . 23
3.4 Schematic overview of the hybrid reduced-order $0\mathrm{D}$–$1\mathrm{D}$ model. Time-dependent bulk inventories and the resistance-growth state are represented by zero-dimensional ODEs, while Fe^{2+}/Fe^{3+} transport is solved quasi-steadily in one dimension across the membrane. The effective coefficient k_{block} is obtained from the Membrane X H-cell resistance-growth experiment under symmetric, zero-DC-bias exposure. The principal model comparison concerns the normalised stack-resistance trajectory. . . . 26

4.1 Beginning-of-charge (BOC) resistance of Membrane X during stack cycling as a function of total cycling time. The solid line shows the fitted saturating exponential (Equation 3.6). 34
4.2 Beginning-of-charge (BOC) resistance of Nafion NR212 during stack cycling as a function of total cycling time. The solid line shows the fitted saturating exponential (Equation 3.6). . . . 35
4.3 Current and voltage response of the CMVN stack during the stepped-power cycling protocol. The stack completed several full charge–discharge cycles, but repeated abrupt cutoff-limited transitions occurred between cycles, and stable uninterrupted multi-cycle operation was not maintained. . . . 35
4.4 Secondary-electron image of pristine (uncycled) NR212, showing the characteristic anisotropic ridge (“tiger-stripe”) surface texture used as the morphological reference . . . 37
4.5 EDS analysis of pristine NR212 (15 kV, 600×). Spectrum 2, acquired on the plain membrane matrix, shows only C, O, F, and trace Si; no iron is detected. The Spectrum 1 particulate is reported in Figure H.3. . . . 37

4.6 EDS analysis of cycled NR212, Field 1 (15 kV, 190×). Spectrum 1, acquired on the plain matrix, is iron-dominated (86.09 at%, 95.53 mass norm.%). Spectrum 2, acquired on the bright particulate visible in the SEM context image, having substantial Pt contribution (2.24 at%, 25.66 mass norm.%), identifying this feature as catalyst-derived contamination rather than an iron deposit. . . . 38
4.7 EDS analysis of cycled NR212, Field 2 (15 kV, 139×). Spectrum 3, acquired on the plain matrix, is again iron-dominated (49.85 at%, 69.26 mass norm.%), reproducing a strong Fe signal at a second spatially separated off-particle location. (Figure 4.6). Spectra 1 and 2, acquired on the bright particulates visible in the SEM context image, identified further Pt/S-bearing contamination and are reported in Figure H.4 and Figure H.5 39
4.8 Comparison of pristine and cycled Membrane X surfaces (5 kV). The pristine surface (a) shows ridges with no resolvable morphological feature, precluding a pristine SEM-EDS baseline for this membrane. The cycled surface (b) is comparatively stable and resolves discrete surface features. . . . 39
4.9 Representative off-particle (matrix) EDS point spectra for Membrane X, Field 1 (15 kV, 470×); SEM context for both points is shown in Figure 4.8b. Spectrum 2 (Fe 0.52 at.%, Fe 2.12 mass norm.%) additionally shows a minor Ca signal; Spectrum 3 (Fe 0.68 at.%, 2.77 mass norm.%) is dominated by C, O, and S. The remaining EDS Spectra 1, 4 and 5 are reported in Figure H.7 . . . 40
4.10 Representative off-particle (matrix) EDS point spectrum for Membrane X, Field 2, Spectrum 2 (15 kV). This independent field of view again shows a C/O/S-dominated matrix with a modest Fe signal (1.98 at.%, 7.59 mass norm.%), the highest matrix reading recorded across all three fields. The remaining spectra 1,4, 5 and 6 are presented in Figure H.8 and H.9 . . . 40
4.11 Highest-iron on-particle EDS point spectrum for Membrane X, Field 3, Spectrum 1 (15 kV, 650×). Despite the on-particle placement, the Fe signal (6.37 at.%, 19.40 mass norm.%) remains modest, and the raw measured mass fractions sum to only 45.95% of the expected total, indicative of degraded X-ray collection from a small, charging-affected feature. 41
4.12 Iron uptake in Nafion NR212 as a function of immersion time under SoC $= 0$ (Fe^{2+}, blue) and SoC $= 100$ (Fe^{3+}, red) conditions. Each data point corresponds to an independently immersed membrane sample. . . . 42
4.13 Iron uptake in Selemion CMVN as a function of immersion time under SoC $= 0$ (Fe^{2+}, blue) and SoC $= 100$ (Fe^{3+}, red) conditions. Each data point corresponds to an independently immersed membrane sample. . . . 43
4.14 Iron uptake in Membrane X as a function of immersion time under SoC $= 0$ (Fe^{2+}, blue) and SoC $= 100$ (Fe^{3+}, red) conditions. Each data point corresponds to an independently immersed membrane sample. . . . 44
4.15 Evolution of the apparent high-frequency H-cell resistance during symmetric exposure of Membrane X to the 50% SoC iron electrolyte. Blue points denote the measured resistance and the red line denotes the nonlinear least-squares fit of Equation (4.5). . . . 45
4.16 Measured operating history used in the data-assisted Membrane X simulation. The current history is imposed directly. The Fe^{2+}/Fe^{3+} inventory evolves continuously between OCV checkpoints and is re-anchored at the indicated rest-to-cycling transitions. . . . 48
4.17 Measured apparent BOC cell resistance and calculated resistance-growth trajectories obtained using the nominal k_{block} and the lower and upper bounds of its H-cell fit-derived 95% confidence interval. The shaded region represents propagation of the H-cell fit uncertainty in k_{block} only. Because R_0 and $\Delta R_{\max}$ are stack-derived, the comparison evaluates the temporal resistance-growth trajectory rather than an independent prediction of the absolute resistance scale. . . . 49
4.18 Effect of the adopted effective membrane ionic conductivity on the calculated Membrane X resistance-growth trajectory. The three curves represent discrete conductivity scenarios and are not a confidence interval. The goodness-of-fit metrics were evaluated over the comparison interval, 80-400 h. . . . 50

D.1 Polarization test plan . . . 75
D.2 Voltage versus current plot from polarization . . . 76

D.3 Linear region of polarization . . . 77
D.4 EIS measuremnts for NR212 . . . 78
D.5 Equivalent circuit fit for NR212, Spectrum 1. . . . 78
D.6 Equivalent circuit fit for NR212, Spectrum 2. . . . 79
D.7 Equivalent circuit fit for NR212, Spectrum 3. . . . 79
D.8 Equivalent circuit fit for NR212, Spectrum 4. . . . 79
D.9 Equivalent circuit fit for NR212, Spectrum 5. . . . 80
D.10 Erratic, self-intersecting trace with no resolvable arc. . . . 80
D.11 Small axis-crossing loop followed by an anomalous excursion. . . . 81
D.12 Monotonically declining trace, no discernible capacitive arc. . . . 81
D.13 Overlapping, self-crossing loops indicative of drift during acquisition. . . . 81
D.14 Large-amplitude excursion dominating the spectrum. . . . 82
D.15 Near-featureless trace confined to an anomalously narrow impedance range. . . . 82

G.1 State of charge in the electrolyte tank over 100 h at zero applied current. The brief initial adjustment corresponds to the holdup reservoir filling from its initial empty state toward a quasi-steady partitioned concentration, and involves only a small fraction of the tank's total iron inventory. . . . 90
G.2 State of charge versus time for charge and discharge at 25 A and 50 A, starting from SoC $= 50\%$. . . . 91
G.3 Resistance versus time over 100 h with $k_{\mathrm{block}} = 0$. . . . 92

H.1 Resistance evolution recorded for the NR212 stack, showing anomalous behavior possibly attributed to a valve and system faults during the experiment. Due to this, the dataset was excluded from the main analysis. . . . 94
H.2 Resistance evolution recorded for the Membrane X , showing the resistance during initial lower power cycles at 35W. Due to this issue, the initial dataset was excluded from the main analysis. . . . 94
H.3 EDS spectrum of Spectrum 1, the particulate visible in Figure 4.5a (pristine NR212), containing Al, S, and Cl. This feature is attributed to external contamination. . . . 95
H.4 EDS spectrum of Spectrum 1, a Pt/S-bearing particulate visible in Figure 4.7a (cycled NR212, Field 2), consistent with the catalyst-derived contamination reported in Figure 4.6. 95
H.5 EDS spectrum of Spectrum 2, a Pt/S-bearing particulate visible in Figure 4.7a (cycled NR212, Field 2), consistent with the catalyst-derived contamination reported in Figure 4.6. 96
H.6 Secondary-electron images of the same field of view on Membrane X, acquired consecutively (15 kV, 180$\times$). Left: first acquisition. Right: second acquisition. . . . 96
H.7 Remaining EDS point spectra from Field 1 of fouled Membrane X; SEM context for this field is shown in Figure 4.9a. Spectrum 1 is the only point in the full dataset with a detectable F signal (F 6.70 at%, Fe 0.35 at%). Spectra 4 and 5 are plain C/O/S-dominated matrix points (Fe 0.83 and 1.01 at%, respectively), consistent with Spectra 2 and 3 of the same field shown in Figure 4.9. . . . 97
H.8 Remaining EDS point spectra from Field 3 of fouled Membrane X (part 1 of 2); SEM context for this field is shown in Figure 4.10a. Spectra 1 and 4 are plain C/O/S-dominated matrix points (Fe 0.73 and 0.80 at%, respectively). . . . 98
H.9 Remaining EDS point spectra from Field 3 of fouled Membrane X (part 2 of 2). Spectrum 5 is the Si-contaminated point discussed in Section 4.2.2 (Si 18.81 at%, Cr 0.38 at%, Fe 0.95 at%, unnormalized sum 119.48%), attributed to an external contaminant rather than an iron-bearing deposit. Spectrum 6 is a plain matrix point (Fe 0.80 at%). . . . 99
H.10 Model verification checks on Fe mass conservation and holdup dynamics (part 1 of 2). . 103
H.11 Model verification checks on Fe mass conservation and holdup dynamics (part 2 of 2). . 104

List of Tables

3.1 Final shortlist of membranes selected for experimental evaluation in this work. 15
3.2 Summary of in-situ cycling conditions for each membrane. 18

4.1 Comparison of representative EDS matrix (off-particle) point spectra for pristine and cycled NR212. Values are atomic percent (at.%), normalized basis. Dashes indicate elements not detected. 38
4.2 Comparison of a representative off-particle EDS spectrum and the highest software-reported on-particle Fe spectrum for Membrane X. The raw analytical total of the on-particle spectrum was 45.95%; software-normalised values are included for qualitative reference only. 41
4.3 Measured mole and charge-equivalent uptake ratios (Fe^{2+}-rich vs.Fe^{3+}-rich) at day 16, compared with the ideal-Donnan-theory prediction 44
4.4 Effect of the H-cell fit-derived k_{block} interval on model agreement over the Membrane X comparison interval, 80-400 h. 47
4.5 Model agreement for the three adopted conductivity scenarios over the Membrane X comparison interval, 80-400 h. 49

A.1 Reference Nafion selectivity $\Phi_{\mathrm{Naf}} = \sigma/P$ used to normalise the selectivity ratio column in Table A.2, organised by battery chemistry. Values marked † were not directly available and were estimated from the nearest compatible chemistry or source (see notes). . . . 61
A.2 Membrane candidate list screened for Fe–H_2 RFB application. Selectivity S = σ/P and ratio Ψ/Ψ_{Naf} are calculated quantities (†). Conductivity values converted from reported ASR are marked ‡. 62

B.1 Summary of all numerical parameters used in the computational model for Membrane X. Source classification: M = measured in this work; L = literature; D = derived from measured quantities; F = fitted to H-cell experimental data. Entries marked † are assumed equal to the NR211 literature value pending direct measurement. 71

C.1 Bulk electrolyte speciation, common to all three membranes, at SoC $= 0$, 0.5, and 1. All concentrations in $\mathrm{mol\,L^{-1}}$. 72
C.2 Ideal Donnan equilibrium results for Nafion NR212 ($c_{\mathrm{fix}} = 1.96\ \mathrm{mol\,L^{-1}}$). All concentrations in $\mathrm{mol\,L^{-1}}$. 73
C.3 Ideal Donnan equilibrium results for Membrane X ($c_{\mathrm{fix}} = 2.368\ \mathrm{mol\,L^{-1}}$). All concentrations in $\mathrm{mol\,L^{-1}}$. 73
C.4 Ideal Donnan equilibrium results for CMVN ($c_{\mathrm{fix}} = 5.264\ \mathrm{mol\,L^{-1}}$). All concentrations in $\mathrm{mol\,L^{-1}}$. 73
C.5 Fixed-charge concentration and cross-endpoint Fe^{2+}/Fe^{3+} partition ratio for all three membranes, ideal Donnan model. 74

D.1 Comparison of resistance measurement techniques evaluated for in-situ stack monitoring. 82

F.1 NaOH consumption by the iron-containing dummy solutions after subtraction of the common acid contribution. 87

G.1 Observed time and migratory-flux scaling ratios between 25 A and 50 A, compared against the value of 2 expected from Faraday's law and the linear field–current relationship in Eq. (G.1). 91
G.2 Influence of the exploratory mobile-iron sink on the model–experiment agreement for the common valid comparison interval with $t \geq 80$ h. 93

H.1 UV-Vis-derived Fe uptake for the NR212 and Membrane X samples collected from the affected stacks (Section 3.2.7). Values are provided for completeness; not used for quantitative analysis due to the unreliability of the source samples. 95
H.2 Full EDS point spectrum dataset for fouled Membrane X (17 points, 3 fields of view). Values are atomic percent (at.%), normalized basis. “Sum (raw)” is the unnormalized mass total prior to renormalization; values below 100% indicate degraded X-ray collection. Dashes: element not detected. Bold rows: spectra presented in full in Section 4.2.2. Field 3, Point 6 shows a high Si signal, indicating an unrelated contamination particle. . 100
H.3 Water uptake measurements for Membrane X. Five samples were pre-treated per supplier recommendation, dried at 80 °C overnight, and soaked in ultrapure water for at least 4 hours between each wet mass measurement. The water uptake of each sample is calculated from the average of the three wet mass readings; the reported value is the mean across all five samples. 100
H.6 Ion exchange capacity measurements for CMVN. 100
H.4 Water uptake measurements for CMVN. Five samples were dried at 80 °C overnight, and soaked in ultrapure water for at least 4 hours between each wet mass measurement. The water uptake of each sample is calculated from the average of the three wet mass readings; the reported value is the mean across all five samples. 101
H.5 Area density of Nafion NR212 and Membrane X, determined from circular punched samples of diameter 3.195 cm (area $= 8.018\ \mathrm{cm}^2$). The resulting area density and dry mass are used to determine the iron uptake in the membrane samples from the stack (mol $\mathrm{g}_{\mathrm{dry}}^{-1}$). 101

Nomenclature

List of Abbreviations

Abbreviation	Definition
AEM	Anion-exchange membrane
AqORFB	Aqueous organic redox flow battery
ASR	Area-specific resistance
BOC	Beginning of charge
BOD	Beginning of discharge
BVP	Boundary-value problem
CCCV	Constant-current constant-voltage
CE	Coulombic efficiency
CEM	Cation-exchange membrane
CFD	Computational fluid dynamics
CI	Confidence interval
CPE	Constant-phase element
DC	Direct current
EDS	Energy-dispersive X-ray spectroscopy
EIS	Electrochemical impedance spectroscopy
EP	Equivalence point
GDE	Gas-diffusion electrode
H-cell	Two-compartment H-shaped diffusion cell
HyFe	Hydrogen–iron redox flow battery
ICP–MS	Inductively coupled plasma mass spectrometry
ICP–OES	Inductively coupled plasma optical emission spectrometry
ICRFB	Iron–chromium redox flow battery
IEC	Ion-exchange capacity
LDL	Liquid-diffusion layer
MAE	Mean absolute error
NRMSE	Normalised root-mean-square error
OCV	Open-circuit voltage
ODE	Ordinary differential equation
PEIS	Potentiostatic electrochemical impedance spectroscopy
PEM	Proton-exchange membrane
PFAS	Per- and polyfluoroalkyl substances
PFSA	Perfluorosulfonic acid
PNP	Poisson–Nernst–Planck
PSIRFB	Polysulfide redox flow battery
PTFE	Polytetrafluoroethylene
RFB	Redox flow battery
RMSE	Root-mean-square error
SE	Secondary-electron imaging mode
SEM	Scanning electron microscopy
SHE	Standard hydrogen electrode
SoC	State of charge
SPEEK	Sulfonated poly(ether ether ketone)
TMS	Teorell–Meyer–Sievers
UP	Ultrapure
UV–Vis	Ultraviolet–visible spectrophotometry
VRFB	Vanadium redox flow battery

WU	Water uptake
XAS	X-ray absorption spectroscopy
XPS	X-ray photoelectron spectroscopy

List of Symbols

Symbol	Definition	Unit
A	Active membrane area	m^2
A_{510}	UV–Vis absorbance at $510\ \mathrm{nm}$	–
A_0	UV–Vis calibration intercept	–
a_i	Activity of ionic species i	–
a_2	CPE exponent in the EIS equivalent circuit	–
b	Fitted slope parameter in the OCV–SoC calibration	V
c_i	Molar concentration of species i in the transport model	$\mathrm{mol\,m^{-3}}$
c_i^{sol}	Bulk-electrolyte concentration used in the Donnan calculation	$\mathrm{mol\,L^{-1}}$
c_i^{mem}	Membrane-water concentration used in the Donnan calculation	$\mathrm{mol\,L^{-1}}$
c_{fix}	Fixed-charge concentration per unit membrane-water volume	$\mathrm{mol\,L^{-1}}$
$c_{\mathrm{Fe,tot}}$	Total analytical iron concentration	$\mathrm{mol\,m^{-3}}$
$C_{\mathrm{H_2SO_4}}$	Analytical sulfuric-acid concentration	$\mathrm{mol\,L^{-1}}$
$C_{\mathrm{Fe,mem}}^{\text{H-cell}}$	Total mobile Fe concentration in membrane water under the H-cell condition	$\mathrm{mol\,m^{-3}}$
$C_{\mathrm{Fe},R}^{\mathrm{eff}}$	Effective total Fe concentration at the hydrogen-side boundary state	$\mathrm{mol\,m^{-3}}$
C_{NaOH}	NaOH titrant concentration	$\mathrm{mol\,L^{-1}}$
D_i	Effective membrane-phase diffusivity of species i	$\mathrm{m^2\,s^{-1}}$
D_i^{aq}	Solution diffusivity of species i in the aqueous reference electrolyte	$\mathrm{m^2\,s^{-1}}$
E	Signed one-dimensional electric field, $E = -\partial\phi/\partial x$	$\mathrm{V\,m^{-1}}$
$E^{\circ\prime}$	Fitted formal potential in the OCV–SoC calibration	V
F	Faraday constant	$\mathrm{C\,mol^{-1}}$
f	Frequency	Hz
f_{dil}	Overall dilution factor in the UV–Vis analysis	–
I	Cell current; $I > 0$ for charge and $I < 0$ for discharge	A
IEC	Ion-exchange capacity	$\mathrm{meq\,g^{-1}}$
j	Membrane current density, $j = I/A$	$\mathrm{A\,m^{-2}}$
K_i	Donnan partition coefficient of species i	–
$K_{a,2}$	Concentration-based second dissociation constant of $\mathrm{HSO_4^-}$	$\mathrm{mol\,L^{-1}}$
k_{obs}	Observed pseudo-first-order resistance-growth coefficient	$\mathrm{s^{-1}}$
k_{block}	Effective concentration-normalised resistance-growth coefficient	$\mathrm{m^3\,mol^{-1}\,s^{-1}}$
m_{dry}	Dry membrane mass	g
m_{wet}	Wet membrane mass	g
N_i	Molar flux of species i through the membrane	$\mathrm{mol\,m^{-2}\,s^{-1}}$
n_i	Moles of species i in a model compartment	mol
n_{drag}	Electro-osmotic drag coefficient (moles H_2O per mole H^+)	–
n_{Fe}	Total moles of extracted or modelled iron, as specified	mol
$\dot{n}_{\mathrm{rxn}}$	Faradaic Fe^{2+}/Fe^{3+} conversion rate, I/F	$\mathrm{mol\,s^{-1}}$
P	Permeability of the undesired active species	$\mathrm{m^2\,s^{-1}}$
Pe	Péclet number, ratio of convective to diffusive transport	–

q	Retained total iron per unit dry membrane mass	$\mathrm{mol\,g_{dry}^{-1}}$
Q_2	CPE magnitude in the EIS equivalent circuit	$\mathrm{F\,s^{a_2-1}}$
R_g	Ideal gas constant	$\mathrm{J\,mol^{-1}\,K^{-1}}$
$R(t)$	Apparent time-dependent cell resistance	Ω
R_app	Apparent resistance obtained from a current step	Ω
$R_\mathrm{BOC,10s}$	Apparent BOC resistance evaluated $10\ \mathrm{s}$ after charge begins	Ω
$R_\mathrm{\Omega,H}$	Apparent high-frequency H-cell resistance	Ω
R_0	Fitted resistance intercept or resistance baseline at $t = 0$	Ω
R_sat	Fitted asymptotic resistance	Ω
R_1	High-frequency ohmic resistance in the EIS equivalent circuit	Ω
R_2	Charge-transfer resistance in the EIS equivalent circuit	Ω
R_pol	Resistance obtained from the polarisation-curve slope	Ω
R_tot	Total equivalent-circuit resistance, $R_1 + R_2$	Ω
R^2	Coefficient of determination	–
RMSE	Root-mean-square error	Ω
NRMSE	Normalised root-mean-square error	%
$\mathcal{R}_\mathrm{mol}$	Late-time molar retained-iron ratio, $q_{\mathrm{Fe^{2+}\text{-}rich}}/q_{\mathrm{Fe^{3+}\text{-}rich}}$	–
$\mathcal{R}_\mathrm{eq}$	Charge-equivalent retained-iron ratio, $2q_{\mathrm{Fe^{2+}\text{-}rich}}/(3q_{\mathrm{Fe^{3+}\text{-}rich}})$	–
$\mathcal{R}_D$	Extended-ideal Donnan cross-endpoint partition ratio	–
S	Membrane selectivity, $S = \sigma/P$	$\mathrm{S\,s\,m^{-3}}$
S_T	Total analytical sulfate-moiety concentration	$\mathrm{mol\,L^{-1}}$
s_E	Sign-convention factor for electric-field orientation	–
T	Temperature	K
t	Time	s
$t_{\mathrm{diff},i}$	Through-thickness diffusion timescale of species i, δ^2/D_i	s
t_{99}	Fit-derived time to reach 99% of the asymptotic resistance increment	s
u_i	Mobility coefficient with respect to the electrochemical-potential gradient	$\mathrm{mol\,m^2\,J^{-1}\,s^{-1}}$
V	Cell voltage	V
V_L	Iron-electrolyte tank volume	$\mathrm{m^3}$
$V_{R,\mathrm{eff}}$	Effective hydrated hydrogen-side boundary-volume scale	$\mathrm{m^3}$
V_sample	Aqueous sample volume used in UV–Vis analysis	L
V_NaOH	NaOH volume delivered at the equivalence point	L
v	Bulk convection velocity in the membrane	$\mathrm{m\,s^{-1}}$
WU	Water uptake, expressed as water mass per dry-polymer mass	$\mathrm{g\,g^{-1}}$
x^*	Positive physical root of the Donnan electroneutrality equation	–
z_i	Charge number of species i	–
$Z(f)$	Complex impedance as a function of frequency	Ω

Greek Symbols

Symbol	Definition	Unit
δ	Membrane thickness	m
ΔI	Applied-current change across a current step	A
ΔV	Cell-voltage change across a current step	V
ΔR_max	Fitted asymptotic resistance increment	Ω

ε_{510}	UV–Vis calibration slope for ferroin at $510\ \mathrm{nm}$ with a $1\ \mathrm{cm}$ path length	$\mathrm{L\,mol^{-1}}$
θ	Dimensionless effective resistance-growth state	–
κ_{eff}	Adopted effective membrane ionic conductivity in the field closure	$\mathrm{S\,m^{-1}}$
μ_i	Electrochemical potential of species i	$\mathrm{J\,mol^{-1}}$
μ_i^0	Standard chemical potential of species i	$\mathrm{J\,mol^{-1}}$
ρ_{water}	Density of water	$\mathrm{g\,cm^{-3}}$
σ	Membrane ionic conductivity used in literature screening	$\mathrm{S\,m^{-1}}$
σ_{app}	Apparent through-plane conductivity estimated from δ/ASR	$\mathrm{S\,m^{-1}}$
σ_{areal}	Dry membrane areal mass density	$\mathrm{g\,cm^{-2}}$
ϕ	Local electric potential	V
ϕ_D	Donnan potential, $\phi_{\mathrm{mem}} - \phi_{\mathrm{sol}}$	V
Ψ	Relative selectivity factor, $S_{\mathrm{candidate}}/S_{\mathrm{Nafion,matched}}$	–

Subscripts and Superscripts

Notation	Meaning
$(\cdot)_0$	Fitted baseline or value at the chosen time origin
$(\cdot)_2$, $(\cdot)_3$	Fe^{2+} and Fe^{3+} species, respectively
$(\cdot)_L$	Iron-electrolyte tank or left membrane boundary
$(\cdot)_R$	Effective hydrogen-side boundary state or right membrane boundary
$(\cdot)_{\mathrm{eff}}$	Effective reduced-order quantity
$(\cdot)_{\mathrm{fix}}$	Fixed-charge quantity
$(\cdot)_{\mathrm{tot}}$	Total quantity
$(\cdot)_{\mathrm{dry}}$, $(\cdot)_{\mathrm{wet}}$	Dry- and wet-membrane quantities
$(\cdot)_{\mathrm{areal}}$	Quantity normalised by membrane area
$(\cdot)_{\mathrm{BOC}}$	Beginning-of-charge quantity
$(\cdot)_{\mathrm{OCV}}$	Open-circuit-voltage-derived quantity
$(\cdot)_{\mathrm{sat}}$	Fitted asymptotic value
$(\cdot)_{\mathrm{pol}}$	Quantity obtained from polarisation analysis
$(\cdot)_{\mathrm{exp}}$	Experimentally derived quantity
$(\cdot)_{\mathrm{model}}$	Model-calculated quantity
$(\cdot)^{\mathrm{sol}}$	Bulk-electrolyte solution phase
$(\cdot)^{\mathrm{mem}}$	Membrane-water phase
$(\cdot)^{\mathrm{aq}}$	Aqueous reference solution
$(\cdot)^{\text{H-cell}}$	H-cell condition
$(\cdot)_{\mathrm{Fe}}$	Total iron quantity
$(\cdot)_{\mathrm{H^+}}$, $(\cdot)_{\mathrm{Fe^{2+}}}$, $(\cdot)_{\mathrm{Fe^{3+}}}$	Species-specific quantities
$(\cdot)_{\mathrm{HSO_4^-}}$, $(\cdot)_{\mathrm{SO_4^{2-}}}$	Bisulfate- and sulfate-specific quantities
$(\cdot)^\circ$	Standard-state quantity
$(\cdot)^{\circ\prime}$	Fitted formal electrochemical quantity
$(\cdot)^*$	Positive physical root of a nonlinear constraint

1

Introduction

The global energy system is undergoing a fundamental structural transition driven by the accelerating deployment of solar photovoltaic and wind power. Renewable electricity generation has grown at an unprecedented rate over the past decade, with cumulative capacity additions reaching approximately 2,400 GW between 2019 and 2024 alone, more than double the additions recorded in the preceding six-year period [1]. Solar photovoltaic technology has been the dominant driver of this growth, and its share of new capacity additions is projected to increase further through 2030, with the cumulative capacity addition of renewables set to double again between 2025-2030, as illustrated in Figure 1.1.

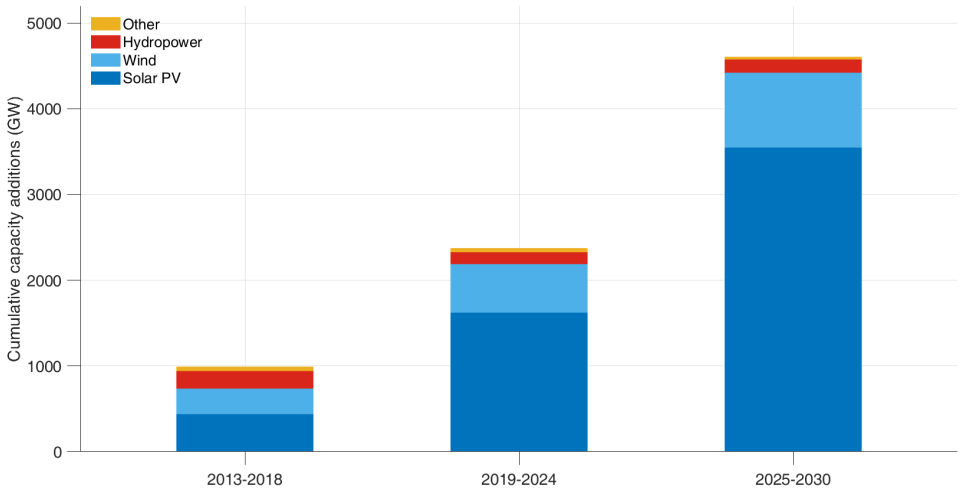


Figure 1.1: Cumulative renewable electricity capacity additions by technology segment across three six-year periods. Adapted from [1], Licence: CC BY 4.0.

Despite this progress, the inherently intermittent and non-dispatchable nature of solar and wind resources introduces a structural mismatch between generation and demand: solar output peaks at midday while residential demand peaks in the evening, and wind generation can be absent for extended periods regardless of grid load. Bridging this mismatch at scale requires technologies capable of storing energy over hours to days and releasing it on demand, a capability that is increasingly recognised as a prerequisite for high-penetration renewable grids [2].

The increasing penetration of variable renewable generation creates storage requirements across multiple timescales. Lithium-ion batteries are well established for many short- and medium-duration applications; however, multi-hour to multi-day storage with a large energy-to-power ratio also motivates technologies in which energy capacity can be increased without a proportional increase in power-conversion

hardware. Long-duration energy storage has therefore become an important area of technology development, with the appropriate duration threshold depending on the application and system context [3]. This requirement has driven sustained and accelerating research interest across the energy storage field. As shown in Figure 1.2, publications indexed under the keyword *energy storage* grew from approximately 15,500 per year in 2015 to over 65,000 per year in 2025, a more than fourfold increase over a single decade, reflecting the urgency with which the scientific community is responding to this challenge.

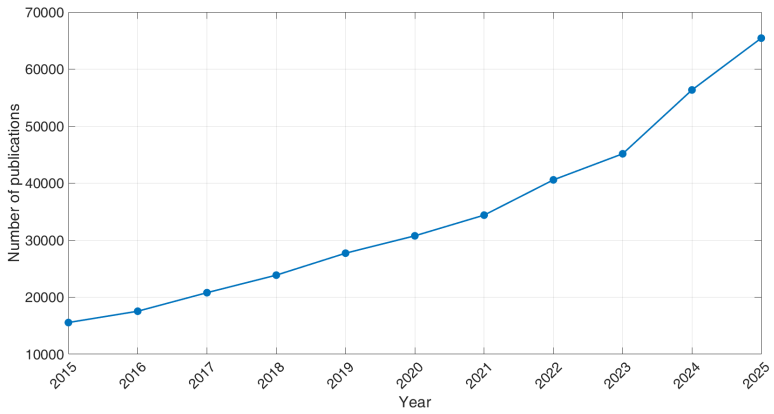


Figure 1.2: Annual number of publications indexed in Scopus under the keyword *energy storage* (title, abstract, and keyword search; journal articles and reviews only), 2015–2025. Data retrieved June 2026.

Among the candidate technologies for long-duration grid storage, redox flow batteries (RFBs) have attracted particular attention due to a combination of properties that distinguish them from solid-state battery systems. In an RFB, electroactive species are stored in external fluid reservoirs and supplied to the electrochemical cell stack during operation. In conventional RFBs these species are dissolved in liquid electrolytes, whereas hybrid configurations may additionally employ a gaseous reactant. The physical separation of the energy-storing electrolyte from the power-converting cell stack allows energy capacity and power output to be scaled largely independently: capacity scales with tank volume and electrolyte concentration, while power scales with cell stack area. This decoupling makes RFBs particularly well suited to long-duration applications, where the energy-to-power ratio must be large and the cost of additional storage capacity must remain low [2], [3]. Additional potential advantages include long cycle life, reduced exposure to degradation mechanisms associated with repeated bulk solid-state phase transformations, and the possibility of estimating state of charge from electrolyte composition or electrochemical measurements.

The growing recognition of the advantages of RFBs is clearly reflected in the research literature. As shown in Figure 1.3, publications indexed under the keyword *redox flow battery* grew from approximately 316 per year in 2015 to 926 per year in 2025, nearly a threefold increase over the same period. This sustained growth demonstrates increasing research attention toward RFBs and motivates continued investigation of their key components and performance limitations.

A critical component of any RFB system is the ion-exchange membrane, which physically separates the positive and negative electrolyte compartments while enabling selective ionic transport to maintain charge balance during operation. The membrane plays a central role in determining the overall efficiency, durability, and cost of the system, as illustrated in Figure 1.4. Its performance is governed by several interdependent properties: high ionic conductivity is required to minimise ohmic losses and improve voltage efficiency, while low permeability to active species is essential to reduce crossover, which leads to capacity fade and reduced Coulombic efficiency. In addition, membranes must exhibit sufficient mechanical and chemical stability to withstand prolonged operation under highly oxidative and acidic conditions. These requirements are inherently conflicting, resulting in trade-offs that complicate membrane selection and optimisation [4]. A membrane that performs well in one respect may remain unsuitable if it fails in another: a highly selective membrane may suffer from poor conductivity leading to increased resistive losses, whereas a highly conductive membrane may allow excessive species

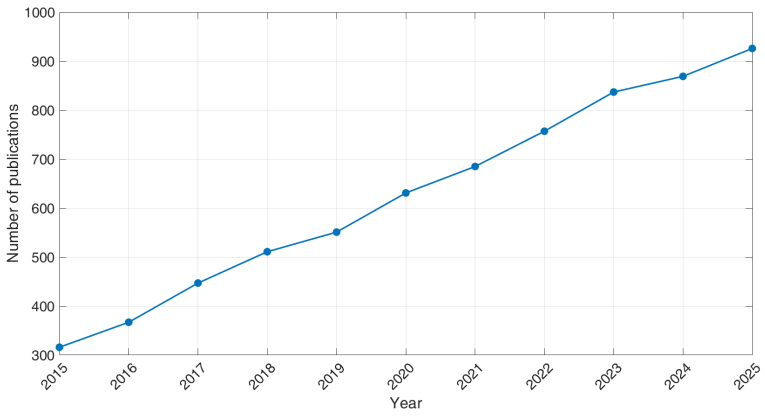


Figure 1.3: Annual number of publications indexed in Scopus under the keyword *redox flow battery* (title, abstract, and keyword search; journal articles and reviews only), 2015–2025. Data retrieved June 2026.

crossover, compromising efficiency and capacity retention.

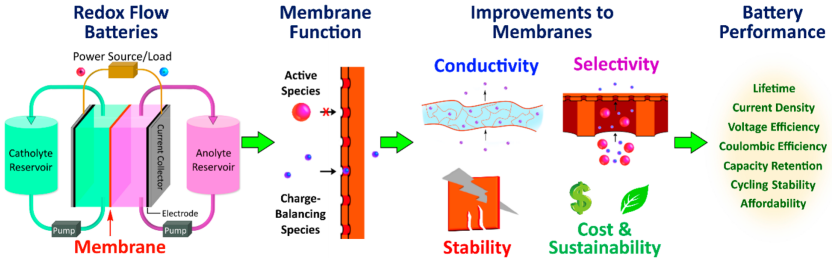


Figure 1.4: The role of improved membranes in redox flow batteries [5].

To date, most membrane studies in RFB systems have been conducted in the context of vanadium redox flow batteries (VRFBs), where perfluorosulfonic acid (PFSA)-based membranes such as Nafion are widely used due to their high proton conductivity and chemical stability. However, PFSA membranes exhibit several well-documented limitations, including high cost, significant species crossover, and environmental concerns associated with fluorinated polymers [4]. These challenges have motivated increasing interest in alternative membrane materials, particularly hydrocarbon-based membranes, which offer potential advantages in terms of cost, sustainability, and tunability of physicochemical properties.

Despite these developments, the extension of these insights to alternative RFB chemistries remains limited. In particular, hydrogen–iron (HyFe) redox flow batteries represent a promising system that has not been studied as extensively as VRFBs. Although general trends observed in VRFB systems provide a useful foundation, direct translation is not always valid due to differences in redox species, electrolyte composition, and transport mechanisms.

Furthermore, the majority of existing studies have focused on cation exchange membranes (CEMs), with comparatively limited attention given to anion exchange membranes (AEMs), especially in acidic environments. AEMs exhibit fundamentally different charge transport mechanisms compared to CEMs, leading to distinct performance characteristics. In principle, AEMs can suppress cation crossover through Donnan exclusion; however, they may also exhibit lower ionic conductivity due to the nature of their charge carriers [6], [7]. The resulting trade-off between reduced crossover and increased resistance remains insufficiently understood, particularly in the context of HyFe systems.

In addition to experimental investigations, modelling approaches play a crucial role in understanding membrane behaviour and guiding material selection. However, many existing models rely on computationally intensive methods such as computational fluid dynamics (CFD), which may not be suitable for rapid screening or comparative evaluation of membrane candidates. The development of simplified, computationally efficient models that capture the dominant transport phenomena is therefore of

significant practical interest.

In light of these considerations, a structured investigation of membrane performance, material selection, and resistance modelling in HyFe redox flow batteries is required to enable informed decision-making and advance the development of this technology.

1.1. Research Gap

Despite extensive research on membrane materials for redox flow batteries (RFBs), significant gaps remain in the understanding and evaluation of membrane performance, particularly in the context of emerging chemistries such as hydrogen–iron (HyFe) systems. Most membrane studies have been conducted in vanadium redox flow batteries (VRFBs), where perfluorosulfonic acid (PFSA)-based membranes such as Nafion are widely used due to their high proton conductivity and chemical stability [7], [8], [9]. However, the direct transferability of these findings to HyFe systems is limited due to differences in redox species, electrolyte composition, and transport behaviour. As a result, a systematic and comparative evaluation of membrane performance specifically in HyFe chemistry remains lacking.

Both cation- and anion-exchange membranes were considered during the initial literature screening because their fixed-charge chemistries produce different conductivity and crossover characteristics. However, the experimental programme ultimately focused on selected cation-exchange membranes after the available AEM candidates were not advanced beyond the practical screening stage due to poor performance in the HyFe system. The central experimental comparison in this thesis therefore concerns PFSA and hydrocarbon CEM candidates rather than a controlled CEM–AEM material comparison.

Furthermore, PFSA-based membranes continue to dominate RFB applications despite known limitations, including high cost, considerable crossover, and environmental concerns associated with fluorinated polymers. Recent studies have highlighted increasing regulatory pressure on fluorinated materials, motivating the need for alternative membrane chemistries [9], [10]. Hydrocarbon-based membranes, such as sulfonated aromatic polymers, have emerged as promising candidates; however, their performance is strongly influenced by structural factors such as degree of sulfonation, which introduces a trade-off between conductivity, swelling, and permeability [9], [11]. Comparative evidence for PFSA and hydrocarbon membranes under clearly documented, HyFe-relevant conditions is therefore needed to assess their potential as alternative membrane classes.

Although iron-associated membrane fouling is frequently invoked to explain resistance growth in proton-conducting electrochemical systems, direct HyFe-specific evidence remains limited. In particular, relatively few studies combine long-duration resistance measurements with controlled retained-iron quantification and post-cycling elemental observations. Consequently, the relationship between apparent cell-resistance evolution, water-wash-resistant retained iron, and local Fe-related signals on cycled membranes remains insufficiently resolved. The techniques used in the present work provide complementary but different information. Controlled immersion and subsequent extraction quantify the total iron retained after defined Fe^{2+}-rich and Fe^{3+}-rich exposure conditions, while SEM–EDS provides local elemental observations within selected electron-interaction volumes.

A further gap concerns the transfer of resistance-growth kinetics between controlled ex-situ measurements and an operating stack. Under symmetric, zero-DC-bias H-cell conditions, the membrane is exposed to an approximately constant iron concentration without a sustained migration field. During stack cycling, by contrast, the membrane experiences changing Fe^{2+}/Fe^{3+} composition, time-dependent boundary concentrations, and a periodically reversing electric field. It is therefore unclear whether an effective concentration-normalised resistance-growth coefficient derived under the controlled H-cell condition retains descriptive value during stack operation.

Detailed multiphysics models can resolve local flow, concentration, potential, and reaction distributions, but require substantial parameterisation and computational effort. A reduced-order formulation is therefore appropriate for repeatedly simulating the measured hundreds-of-hours operating history while retaining the dominant effects of diffusion, electromigration, interfacial partitioning, and changing electrolyte composition. No model combining these elements with a dynamic resistance-growth state for long-duration iron-based RFB operation was identified in the literature reviewed for this thesis to the best of the author's knowledge.

1.2. Research Questions

Based on the identified gaps, comparative evidence for membrane behaviour in hydrogen–iron redox flow battery systems remains limited. In particular, membrane candidates have rarely been assessed within a common framework combining retained-iron uptake, long-term stack resistance evolution, post-cycling elemental observations, and reduced-order transport modelling. Furthermore, to the best of the author's knowledge, no published model couples iron transport with a dynamic resistance-growth state for long-duration operation in an iron-based RFB.

This thesis develops and applies an integrated experimental and modelling framework to three selected membrane candidates: Nafion NR212 as a PFSA baseline, CMVN and Membrane X as hydrocarbon cation-exchange membranes. The framework is intended to support comparative evaluation and model–experiment interpretation rather than to provide a fully controlled intrinsic material ranking or unique mechanistic identification. The main research question is therefore formulated as follows:

> **How do selected PFSA and hydrocarbon cation-exchange membranes compare under documented HyFe-relevant conditions in terms of cycling stability, apparent cell-resistance evolution, and retained-iron behaviour, and to what extent can an H-cell-derived effective resistance-growth coefficient support interpretation of the normalised Membrane X stack-resistance trajectory when embedded in a data-assisted reduced-order transport model?**

In this context, *evaluation* refers to the comparative assessment of membrane behaviour using apparent cell-resistance evolution, retained iron uptake, cycling stability, and qualitative post-cycling elemental observations. The study combines controlled ex-situ exposure, post-mortem characterisation, and in-situ stack cycling. These measurements provide complementary information but do not all represent identical operating conditions or the same physical observable. *HyFe-relevant conditions* include controlled ex-situ environments designed to isolate selected phenomena and in-situ electrochemical cycling representative of stack operation.

In order to address the main research question in a structured and coherent manner, the following sub-questions are defined:

1. How do the selected membrane candidates perform under the tested HyFe conditions in terms of their ability to sustain cycling and their apparent cell-resistance evolution?
2. What qualitative elemental evidence does post-cycling SEM–EDS provide for iron occurence at the analysed membrane-surface locations?
3. Do Fe^{2+}-rich and Fe^{3+}-rich immersion conditions produce different retained-iron uptake in the selected membranes, and how do the observed trends vary across the selected membranes?
4. To what extent can a reduced-order, data-assisted transport model, using an effective rate parameter derived from ex-situ measurements, capture the normalised resistance-growth trend measured for Membrane X?

The first sub-question establishes an empirical comparison of the selected membranes under the documented test conditions. The comparison considers whether stable cycling was sustained and how the apparent cell-resistance indicator evolved over the available test window. Because the membrane tests were not performed under fully identical hardware and operating conditions, the results are interpreted as candidate-level performance evidence rather than as intrinsic material properties.

The second sub-question examines whether iron is detected at selected locations on the cycled membrane surfaces and whether visible surface features coincide with Fe-containing regions. SEM–EDS provides spatially resolved elemental observations at the analysed locations, but does not by itself identify the Fe oxidation state, binding mechanism, or through-thickness distribution. The observations are therefore interpreted qualitatively and considered alongside, rather than used to explain uniquely, the electrochemical resistance trends.

The third sub-question compares the retained-iron inventories obtained after separate Fe^{2+}-rich and Fe^{3+}-rich immersion conditions. The measured trends are compared with an extended-ideal Donnan baseline to assess whether ideal electrostatic partitioning alone is consistent with the observations.

The fourth sub-question evaluates whether the effective resistance-growth timescale inferred from the Membrane X ex-situ test remains consistent with the resistance trajectory measured in the Membrane X stack when embedded in the reduced-order transport framework. The calculation is classified as data-assisted because it uses the measured stack current history, OCV-derived SoC checkpoints, and stack-derived values of R_0(fitted basline cell resistance) and $\Delta R_{\max}$(fitted asymptotic resistance increment). Consequently, the primary comparison concerns the normalised resistance-growth trajectory rather than an independent prediction of the absolute resistance amplitude. Agreement would support the conditional transferability of the ex-situ-derived effective rate parameter to the tested Membrane X stack configuration.

1.3. Research Approach

To address these questions, a combined experimental and modelling approach is adopted. Three membrane candidates spanning different PFSA and hydrocarbon cation-exchange membrane classes are selected using the literature-based screening framework described in Section 3.1. All three membranes are evaluated by static immersion testing, while their stack behaviour is assessed under the relevant operating conditions applicable to each membrane. Post-cycling SEM–EDS is used as qualitative evidence of iron occurrence at selected surface locations.

All three candidates were evaluated using controlled immersion tests and stack cycling under their documented test configurations. The immersion experiments quantified water-wash-resistant, NaCl-exchangeable retained total iron following nominally Fe^{2+}-rich and Fe^{3+}-rich exposure. Post-cycling SEM–EDS was applied to the available NR212 and Membrane X samples to obtain qualitative elemental observations at selected surface locations.

Membrane X is additionally characterised in the H-cell under symmetric, zero-DC-bias iron-electrolyte exposure. The resulting resistance trajectory is fitted to obtain an effective concentration-normalised rate parameter, k_{block}, which is then used in the reduced-order Nernst–Planck transport and fouling model.

The stack simulation is driven by the measured current history and uses OCV-derived SoC checkpoints to limit cumulative oxidation-state drift. Furthermore, R_0 and $\Delta R_{\max}$ are taken from the measured stack resistance trajectory to map the modelled blocking state onto cell resistance. The calculation is therefore a data-assisted forward simulation, not a blind prediction. Its principal test is whether the H-cell-derived effective rate parameter, together with the modelled iron-exposure history, reproduces the normalised temporal evolution of the Membrane X stack resistance.

1.4. Thesis Outline

The thesis is structured as follows. Chapter 2 reviews membrane performance and resistance characterisation in redox flow batteries, including membrane material classes and trade-offs, the specific demands of the hydrogen–iron system, proposed mechanisms of iron-associated membrane resistance growth, and existing membrane-transport models. Chapter 3 presents the membrane screening framework, the reduced-order transport and resistance-growth formulation, and the ex-situ, in-situ, and post-cycling characterization methods. Chapter 4 reports the retained-iron uptake trends, stack resistance evolution, post-cycling elemental observations, and the comparison between the data-assisted model and the normalised Membrane X resistance trajectory. Finally, Chapter 5 presents the conclusions, study limitations, and recommendations for future work.

2

Membrane Performance, Iron Interactions, and Resistance Characterisation in Redox Flow Batteries: A Focused Review

The central design challenge for ion-exchange membranes in RFBs is the trade-off between high ionic conductivity, needed to sustain current flow, and high species selectivity, needed to suppress crossover between the two half-cells; this tension motivates the need for systematic, physically grounded evaluation frameworks. While substantial progress has been made in the development of advanced membrane materials, a comprehensive understanding of how intrinsic membrane properties translate into in-situ electrochemical behaviour, particularly under conditions of long-term operation and concentrated electrolyte exposure, remains limited. This chapter addresses this gap through a focused review of the membrane science most directly relevant to the present work.

Section 2.1 compares PFSA, anion-exchange, and hydrocarbon membrane classes and the conductivity–selectivity–stability trade-offs governing their suitability. Section 2.2 introduces the HyFe electrochemical operating principle and electrolyte chemistry, motivating why continuous iron exposure places distinct demands on the membrane. Section 2.3 reviews the evidence for iron-cation displacement of protons at sulfonate sites and its link to ohmic resistance growth. Section 2.4 situates membrane-associated resistance growth within the broader landscape of electrode, GDE, contact, and other cell-level degradation contributions. Section 2.5 reviews SEM–EDS and UV–Vis as complementary methods for obtaining local elemental observations and solution-based quantification of extracted total iron. Section 2.6 compares ex-situ and in-situ resistance-measurement techniques and motivates the voltage-step method adopted in this work. Finally, Section 2.7 reviews transport-modelling approaches of increasing fidelity, identifies the absence of dynamic fouling-coupled models for iron-based RFBs, and establishes the gap this thesis addresses.

2.1. Membrane Properties, Material Classes, and Performance Trade-offs

The performance of an ion-exchange membrane in an RFB is governed primarily by its ionic conductivity, species selectivity, and chemical stability under operating conditions [4], [8], [12]. These properties are strongly coupled: structural features that enhance ionic transport, such as higher ion exchange capacity or greater water uptake, also tend to increase the permeability of the membrane to redox-active species, while measures that suppress crossover typically come at the cost of higher ohmic resistance. This conductivity–selectivity trade-off has been consistently reported across membrane studies and constitutes the central optimisation challenge in membrane design [4], [13].

Perfluorosulfonic acid (PFSA) membranes, of which Nafion is the most widely used, are the benchmark material in RFB research owing to their high proton conductivity and chemical stability in strongly acidic electrolytes [4], [14]. Their sulfonate functional groups facilitate efficient proton transport through Grotthuss-type hopping, and their PTFE backbone provides chemical and mechanical durability. However, PFSA membranes exhibit relatively high permeability to multivalent cations including vanadium and iron, leading to crossover-related losses and, in iron-containing systems, the possibility of multivalent-cation exchange into the membrane and associated conductivity reduction [15], [16].

Anion exchange membranes (AEMs) transport anions rather than cations and offer different selectivity characteristics. By excluding cationic redox species through Donnan rejection, AEMs can substantially reduce crossover of dissolved metal cations, which has motivated their investigation as alternatives to PFSA membranes in vanadium and iron-based systems [7], [17]. Their conductivity depends strongly on the transported counter-ion and membrane chemistry, while long-term stability and swelling under strongly acidic conditions remain important material-specific considerations [6].

Hydrocarbon-based cation exchange membranes, such as sulfonated aromatic polymers, offer a lower-cost alternative to PFSA membranes while potentially retaining comparable conductivity. Their transport properties depend strongly on the degree of sulfonation, and excessive sulfonation can lead to membrane swelling and increased species permeability, reinforcing the fundamental conductivity–selectivity trade-off [9], [18]. For the Fe–H_2 system, the continuous contact between the membrane and a concentrated iron sulfate electrolyte across the full operational lifetime introduces an additional dimension to membrane selection: in addition to conductivity and selectivity, resistance to iron-induced conductivity decay is a critical performance criterion, as discussed in Section 2.3.

2.2. The Hydrogen-Iron Redox Flow Battery System

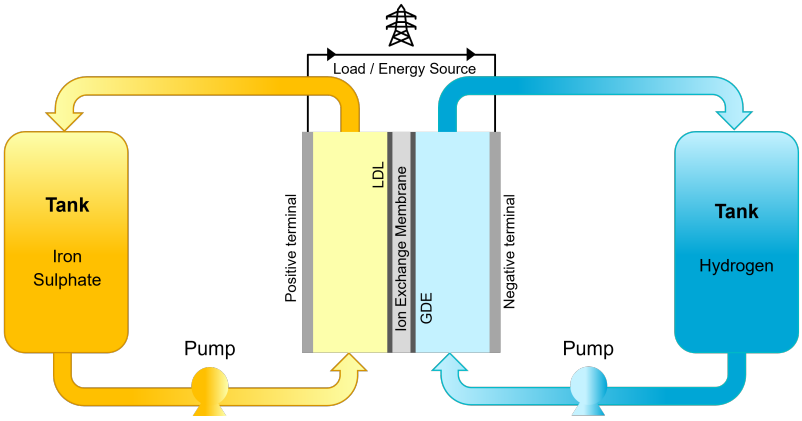


Figure 2.1: Schematic representation of a hydrogen-iron redox flow battery.

A schematic of a typical hydrogen-iron RFB is shown in Figure 2.1. The hydrogen–iron (HyFe) redox flow battery is an aqueous electrochemical energy storage system that employs the Fe^{2+}/Fe^{3+} redox couple at the positive electrode and the H^+/H_2 couple at the negative electrode. During charge and discharge, the electrochemical reactions at each electrode are:

$$\text{Positive electrode:} \quad \mathrm{Fe^{3+} + e^- \rightleftharpoons Fe^{2+}}, \qquad E^\circ = +0.77\ \mathrm{V\ vs.\ SHE}, \tag{2.1}$$

$$\text{Negative electrode:} \quad \mathrm{2H^+ + 2e^- \rightleftharpoons H_2}, \qquad E^\circ = 0.00\ \mathrm{V\ vs.\ SHE}. \tag{2.2}$$

During discharge, hydrogen is oxidised at the negative electrode and Fe^{3+} is reduced at the positive electrode, giving the overall reaction

$$\mathrm{H_2 + 2Fe^{3+} \longrightarrow 2H^+ + 2Fe^{2+}}. \tag{2.3}$$

yielding a theoretical equilibrium open-circuit cell voltage of approximately 0.77 V [12], [19]. The iron electrolyte consists of an aqueous iron sulfate solution in sulphuric acid, typically at iron concentrations of 0.5–1.0 mol L^{-1} and acid concentrations of 1–2 mol L^{-1}. The acidic environment is essential for maintaining the solubility of both Fe^{2+} and Fe^{3+} species and for suppressing the precipitation of ferric hydroxide, which can occur at pH $>$ 2 depending on iron concentration, temperature and sulfate complexation [12], [20].

Compared with the all-vanadium RFB, the HyFe system offers several practical advantages. Iron is earth-abundant, comparatively inexpensive, and the Fe^{2+}/Fe^{3+} redox reaction at the positive electrode is fast and kinetically reversible on carbon-based electrodes under acidic conditions [20]. The use of a hydrogen electrode at the negative side avoids the metal plating and stripping reactions inherent in all-iron hybrid systems, eliminating issues of iron dendrite formation, associated Coulombic efficiency losses, and the coupling of energy and power that limits hybrid architectures [19]. The H^+/H_2 electrode reaction proceeds rapidly on platinum-based catalysts, consistent with the extensive literature on proton-exchange-membrane fuel cells and electrolysers, and enables operation at higher current densities than those accessible with iron plating electrodes [19].

In the HyFe system, the electrolyte-facing membrane surface remains continuously exposed to concentrated acidic iron sulfate throughout operation and across the full operating SoC range. This sustained exposure creates the possibility that Fe^{2+} and Fe^{3+} partition into the hydrated membrane phase and exchange with protonic counter-ions at fixed sulfonate groups. Because multivalent iron counter-ions are less mobile than protons, such exchange can reduce effective proton transport and may contribute to a gradual increase in apparent cell resistance. The extent to which this mechanism controls the measured long-term resistance evolution is examined experimentally and through the reduced-order model in this thesis.

2.3. Cation-Induced Fouling of Ion Exchange Membranes

Multivalent metal cations can exchange with protons associated with the fixed sulfonate groups of proton-conducting ionomers. Such exchange changes the membrane counter-ion composition, hydration state, and charge-transport properties. In particular, Fe^{3+} contamination has been shown to reduce proton mobility and membrane conductivity in PFSA membranes [16], [21]. Sustained iron exposure can therefore contribute to membrane-associated resistance growth, although the measured cell response may also contain electrode, contact, electrolyte, and gas-diffusion-electrode contributions.

Under the specific electrolyte conditions examined by Okada et al., the reported counter-ion behaviour indicated stronger membrane affinity for the trivalent ion than for the divalent ions, while the effect on proton mobility remained cation-specific [21]. This preference has been confirmed both experimentally and computationally, and for both iron oxidation states relevant to the Fe–H_2 system. Molecular dynamics simulations of Nafion contaminated with Fe^{2+} show that the cation coordinates directly to the sulfonate groups, with its equilibrium position governed by the balance between the cation–sulfonate coordination energy and the energetic cost of side-chain rearrangement [22]. The strength of the analogous interaction has been characterised directly for Fe^{3+}: Raman and Fourier-transform infrared spectroscopy of Fe^{3+} ion-exchanged Nafion have been used to characterise changes in the local sulfonate environment following Fe^{3+} exchange, and thermogravimetric analysis showed that this bond is sufficiently strong to suppress the thermal desulfonation of the sulfonic end group that otherwise occurs in the proton form of the membrane [23]. Taken together, these studies support specific association of both iron oxidation states with sulfonate-containing ionomers. They do not, however, establish a universal desorption timescale under the concentrated sulfate conditions of the present system. The irreversible form adopted later in the reduced-order model is therefore treated as an effective net-resistance-growth approximation over the measured interval, rather than as a directly established molecular mechanism.

Replacement of highly mobile protonic counter-ions by less-mobile multivalent counter-ions changes the membrane hydration and mixed-ion transport environment. The conductivity reduction does not necessarily imply that current becomes dominated by the motion of iron complexes; proton transport through the remaining hydrated network may remain important, while the concentration and mobility of protonic charge carriers are reduced. A systematic study of the H^+-, Fe^{3+}-, and mixed H^+/Fe^{3+}-forms of several commercial membranes found the conductivity of the Fe^{3+}-form to be approximately

one order of magnitude lower than that of the corresponding proton form [16]. The effect was also cation-specific: Fe^{3+} strongly reduced proton mobility, whereas Cu^{2+} produced a different mixed-cation transport response under the conditions examined by Okada et al. [21].

A link between iron contamination and increased electrochemical losses has been demonstrated in operating PFSA-based electrolyser cells. In-situ contamination studies of solid-polymer-electrolyte water electrolysers, in which Nafion is exposed to iron-containing feed water, confirmed that Fe^{3+} introduced at the anode migrates through the full membrane cross-section and concentrates at the sulfonic acid groups; electrochemical impedance spectroscopy showed that ohmic resistance accounted for the dominant fraction of the increased cell voltage following contamination, consistent with proton site-blocking as the primary mechanism [24]. A subsequent PEM-electrolysis study found that trace Fe^{3+} contamination raised the cell-voltage degradation rate by roughly an order of magnitude relative to deionised-water operation, with post-mortem energy-dispersive X-ray spectroscopy confirming iron distributed across the membrane and both catalyst layers [25].These studies support a link between iron contamination and increased electrochemical losses in PFSA-based devices. The findings therefore do not imply that all resistance growth in an operating HyFe cell originates within the membrane, although membrane-associated ohmic loss may constitute one contribution.

Although these in-situ studies were conducted in PEM electrolysers rather than redox flow batteries, tthe studies provide mechanistically relevant analogues for the Fe–H_2 system because they involve similar PFSA chemistry and multivalent-cation exchange. Quantitative transfer is not automatic, however, because the electrolyte composition, iron concentration, electrode environment, and operating conditions differ. The key distinction is operational rather than mechanistic: in PEM electrolysers, iron contamination originates from dilute trace impurities, whereas in a Fe–H_2 RFB the membrane is in continuous contact with a concentrated iron sulfate electrolyte throughout its service life. This sustained, high-concentration exposure is expected to drive substantially larger cumulative cation uptake and a longer-timescale resistance evolution than the trace-contamination regime, motivating quantitative evaluation of the resistance-growth trajectory and its possible relationship to iron exposure. That modelling gap is addressed in Section 2.7.

2.4. Other Degradation Phenomena in Redox Flow Batteries

While membrane fouling and resistance growth are the focus of the present work, long-term performance decay in redox flow batteries arises from a broader set of coupled degradation mechanisms that operate simultaneously during cycling. An awareness of these phenomena is necessary to contextualise the scope of the present study and interpret results within the wider degradation landscape.

Electrode degradation is among the most widely documented degradation mechanisms in RFBs. Carbon-based electrodes, which are the standard porous electrode material in most aqueous RFB chemistries, undergo progressive surface oxidation under the harsh acidic and oxidising conditions present during operation. The resulting structural and morphological changes alter electrode wettability and charge-transfer characteristics, reduce the electrochemically active surface area through carbon fibre surface peeling, and lead to poor reaction kinetics, enhanced overpotentials, and reduced energy efficiency and capacity over extended cycling [26], [27].

In liquid–liquid RFB chemistries such as VRFBs, parasitic hydrogen evolution can additionally alter electrolyte balance and reduce Coulombic efficiency [28]. In the HyFe system, by contrast, hydrogen evolution and oxidation constitute the intended negative-electrode reaction. Relevant hydrogen-side degradation modes instead include changes in GDE hydration, catalyst or ionomer contamination, electrical contact evolution, and accumulation of crossed iron in the hydrogen-side assembly.

These processes are not fully decoupled in an operating stack. The beginning-of-charge voltage-step indicator used in this thesis reduces the influence of slower concentration and kinetic polarisation, but it remains a full-cell apparent resistance measurement. It may contain contributions from the membrane, electrolyte, electrodes, GDE, electrical contacts, and short-time interfacial response. Progressive resistance growth is therefore interpreted as membrane-associated and considered alongside the immersion, SEM–EDS, and H-cell results, rather than attributed uniquely to membrane fouling.

2.5. Spectroscopic and Elemental Characterisation of Membrane Iron Retention

Electrochemical measurements alone cannot determine whether an observed resistance change is associated with iron occurrence in the membrane. Elemental and solution-based analyses therefore provide complementary information, although each technique probes a different physical quantity and has distinct interpretive limits.

Scanning electron microscopy with energy-dispersive X-ray spectroscopy (SEM–EDS) provides local elemental information within the electron-beam interaction volume. Depending on sample preparation, it can be used for surface point analysis, elemental mapping, or cross-sectional analysis. EDS identifies elemental signature of Fe but does not determine its oxidation state, chemical coordination, binding mechanism, or bulk membrane concentration. Quantification can also be affected by specimen charging, topography, interaction-volume differences, and standardless normalisation [25], [29]. In the present work, SEM–EDS is therefore used to obtain qualitative elemental observations at selected surface locations rather than to determine through-thickness Fe distribution or total membrane loading.

UV–Vis spectrophotometry with 1,10-phenanthroline provides a sensitive solution-based method for iron determination. Fe^{2+} forms the coloured ferroin complex, while total iron can be measured by first reducing Fe^{3+} to Fe^{2+} [30].

2.6. Methods for Resistance Characterisation

Membrane resistance in redox flow batteries is commonly characterised using a combination of ex-situ and in-situ techniques. Ex-situ methods, including measurements of ionic conductivity and area-specific resistance in simplified cell configurations, are widely used for initial membrane screening due to their reproducibility and simplicity [31]. However, ex-situ conditions do not capture the interfacial and compositional effects present in an operating cell, and in-situ measurements are required to assess resistance behaviour under realistic conditions.

Among in-situ techniques, electrochemical impedance spectroscopy (EIS) is the most widely used method for quantifying internal resistance in redox flow batteries, as it can in principle separate ohmic, kinetic, and mass-transport contributions by analysing the cell response across a range of frequencies. However, the application of EIS in practical large-format stacks is complicated by inductive artefacts arising from cell geometry and cabling at high frequencies, limited usable frequency windows, and the requirement for stationarity during measurement, conditions that are difficult to satisfy during active cycling of a large electrochemical cell [32], [33]. Even when a high-frequency intercept is obtained, the measured resistance may include membrane, electrolyte, contact, current-collector, and geometric contributions unless these are separated through appropriate blank measurements or equivalent-circuit analysis. These limitations can compromise the physical interpretability of the high-frequency intercept that is commonly used to estimate ohmic resistance, particularly when comparing measurements across membranes or over long cycling periods.

Polarisation and current-step methods provide practically accessible alternatives for tracking resistance-related changes during operation. The slope of a quasi-linear polarisation region estimates the overall cell resistance under load [34], [35]. A current-step method instead infers an apparent resistance from the voltage change following a transition from rest to load.

2.7. Modelling Approaches for Membrane Transport and Resistance Evolution

Modelling complements experimental membrane characterisation by linking operating conditions to ionic transport, crossover, and resistance evolution. RFB models range from simple algebraic resistance expressions to multidimensional multiphysics simulations, with the appropriate level of complexity determined by the processes of interest, available parameters, and required simulation timescale.

At the simplest level, membrane ohmic losses can be represented using area-specific resistance, which relates membrane thickness and ionic conductivity [12]. Although useful for system-level analysis, this

approach does not resolve individual species or active-material crossover. More physically resolved models use the Nernst–Planck equation to describe ionic flux through diffusion, electromigration, and, where included, convection [36]. Such formulations have been widely applied to RFBs to calculate crossover, electrolyte imbalance, and the effect of current on membrane transport [37], [38].

A common charged-membrane formulation belongs to the Teorell–Meyer–Sievers class of solution–diffusion models. The membrane is represented as a macroscopically homogeneous charged phase, Nernst–Planck transport is combined with local electroneutrality, and Donnan equilibrium relates the membrane composition to an adjacent aqueous electrolyte [39]. These models are commonly parameterised using measurable properties such as water uptake, ion-exchange capacity, ionic conductivity, and species diffusivity [14], [40].

Higher-fidelity two- and three-dimensional models additionally resolve flow, concentration, potential, and reaction-current distributions across cell-scale domains [41], [42]. Although they provide detailed local information, they require extensive parameterisation and can be computationally demanding for operating histories extending over hundreds of hours. Reduced-order and compartmental models instead simplify the geometry while retaining the principal transport and inventory balances, allowing reservoir composition, state of charge, and crossover to be calculated at substantially lower computational cost [38], [43].

Many RFB transport models focus on crossover, electrolyte imbalance, and capacity fade while treating membrane diffusivity, conductivity, fixed-charge concentration, and partitioning behaviour as time-invariant. A gap therefore remains between models of time-dependent ionic transport and experimental observations of slowly evolving apparent cell resistance. In the literature reviewed for this thesis, no model was identified that combines time-dependent Fe^{2+}/Fe^{3+} membrane transport with an experimentally parameterised resistance-growth state for long-duration operation of an iron-based RFB.

3

Experimental and Modelling Methodology

This chapter presents the experimental and modelling methodology developed for this work. Section 3.1 screens and ranks candidate membranes by a conductivity-to-permeability figure of merit, narrowing the literature pool to NR212, CMVN, and Membrane X. Section 3.2 covers stack assembly, quality verification, and cycling protocol, along with the beginning-of-charge resistance-extraction and fitting method used to track resistance growth. Section 3.3 describes the SEM-EDS sample preparation and imaging conditions used to characterise cycled membrane surfaces. Section 3.4 presents a field-free immersion study isolating Fe^{2+}/Fe^{3+} binding affinity, with iron quantified via the UV-Vis method in Section 3.5. Section 3.6 describes the symmetric H-cell experiment used to extract the effective coefficient k_{block} later transferred to the stack model. Section 3.7 reports the water-uptake and Section 3.8 reports the ion-exchange-capacity measurements used to parameterise the Donnan boundary condition. Finally, Section 3.9 formulates the hybrid 0D–1D transport and fouling model, coupling Nernst–Planck flux, Donnan partitioning, and Langmuir-type kinetics to the measured resistance trajectory.

3.1. Systematic Membrane Screening and Selection

Membrane selection for redox flow batteries requires balancing high ionic conductivity, which minimises ohmic losses, against low active-species permeability, which limits capacity fade through crossover. This conductivity–crossover trade-off is well established in the membrane literature and motivates the use of selectivity as a comparative figure of merit [44], [45]. However, translating this trade-off into a practical selection decision is complicated by the fact that published transport data are obtained under widely varying conditions, different electrolytes, temperatures, pre-treatment protocols, and measurement techniques, making direct inter-study comparison unreliable. Moreover, many membranes reported in the academic literature are not commercially available, or are available only in formats unsuitable for laboratory-scale cell testing.

To address these challenges, a structured screening framework was developed with the objective of reducing a broad initial candidate pool to a practically relevant shortlist. The framework combined literature-derived transport and stability criteria with practical considerations including commercial availability, supplier guidance, and format suitability. The procedure is summarised schematically in Figure 3.1 and described in the subsections below.

3.1.1. Initial Candidate Pool and Chemistry-Relevance Filtering

An initial candidate pool was compiled from membranes reported for redox flow battery applications, encompassing commercial membranes (e.g., Nafion® variants, Selemion® series), chemically modified commercial membranes, and newly developed materials from the recent literature. For each candidate, the following properties were collected where available: membrane chemistry and backbone structure,

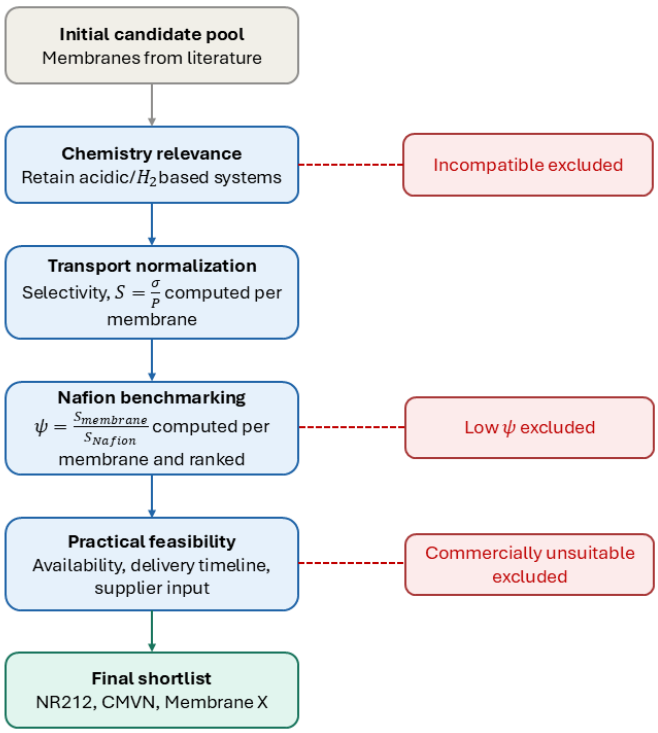


Figure 3.1: Schematic of the membrane screening and selection framework. Candidates are progressively filtered at three stages; those failing each criterion are excluded (dashed red boxes). The final shortlist comprises the three membranes evaluated experimentally in this work: Nafion NR212, CMVN, and Membrane X.

target battery chemistry, dry and hydrated thickness, ionic conductivity or area-specific resistance, permeability of relevant active species, water uptake and dimensional stability, reported chemical and mechanical stability, and the duration and conditions of any cycling or durability tests. The complete database is provided in Appendix A.

The first screening step retained only membranes with demonstrated operation in electrochemical environments considered chemically relevant to Fe–H_2 conditions, including acidic vanadium redox flow battery systems, iron-based flow battery chemistries, hydrogen-evolving or hydrogen-oxidising systems, and other strongly acidic electrochemical cells with comparable membrane demands. Membranes evaluated exclusively in alkaline or neutral-pH systems were excluded because membrane stability and transport behaviour can differ substantially between chemically distinct environments, and extrapolation from chemically dissimilar systems would introduce substantial uncertainty into the screening. Evidence from adjacent acidic electrochemical systems was used primarily to assess chemical stability and general ionic-transport suitability.

3.1.2. Transport Normalisation and Selectivity-Based Ranking

Both cation-exchange membranes (CEMs) and anion-exchange membranes (AEMs) were considered in the initial screening. The desired charge carrier differs between the two classes: protonic or cationic conduction is relevant for CEMs, whereas sulfate and bisulfate transport contributes to conduction in acidic AEMs. However, the permeability term used in the conductivity–crossover figure of merit must represent an undesired redox-active species. For the HyFe system, Fe^{2+} and Fe^{3+} permeability was therefore preferred for both membrane classes. Where direct iron-permeability data were unavailable, permeability data for surrogate metal-ion species were retained only as indirect screening evidence and were compared quantitatively only within closely matched studies. Sulfate or bisulfate permeability was not treated as the undesired crossover term because these anions constitute the intended charge carriers in an AEM.

Where ionic conductivity was not reported directly but area-specific resistance (ASR) and membrane thickness were available, an apparent through-plane conductivity was estimated from

$$\sigma_{\mathrm{app}} = \frac{\delta}{\mathrm{ASR}}, \tag{3.1}$$

where δ is the membrane thickness and ASR is expressed in $\Omega\,\mathrm{m}^2$. Wherever possible, thickness and ASR values corresponding to the same hydration and temperature conditions were used. The conversion assumes homogeneous through-plane transport and negligible contact and interfacial contributions. Values obtained in this manner were therefore used as comparative screening estimates rather than as intrinsic conductivity measurements.

Membrane selectivity was then defined as

$$S = \frac{\sigma}{P}, \tag{3.2}$$

where P is the permeability of the undesired active species ($\mathrm{m}^2\,\mathrm{s}^{-1}$). This ratio captures the essential design objective of high conductivity relative to low crossover and is widely adopted as a compact performance metric in the RFB membrane literature [44].

To reduce inter-study variability, Nafion was adopted as an internal reference membrane. The relative selectivity factor was calculated only when the candidate and Nafion data referred to the same permeating species and sufficiently matched electrolyte composition, temperature, hydration state, and measurement method. Same-publication measurements obtained under identical conditions were assigned the highest confidence. Where a same-study Nafion reference was unavailable, the closest chemically and experimentally matched literature value was used and the result was classified as lower-confidence, indicative evidence rather than as a strict quantitative rank. Candidates lacking sufficient conductivity or permeability data were retained for qualitative feasibility assessment but were not assigned a numerical relative-selectivity factor. A relative selectivity improvement factor was defined as

$$\Psi = \frac{S_{\mathrm{candidate}}}{S_{\mathrm{Nafion,matched}}}, \tag{3.3}$$

where $\Psi > 1$ indicates a more favourable conductivity–crossover trade-off than Nafion under comparable conditions, and $\Psi < 1$ indicates inferior performance relative to the benchmark.

3.1.3. Practical Feasibility Assessment and Final Selection

The transport-based ranking alone was insufficient for membrane selection, as highly ranked candidates are unusable if unavailable, discontinued, or incompatible with the intended cell format. Each shortlisted membrane was therefore also assessed for commercial availability, lead time, dimensions, and format suitability, with supplier consultation on acid handling, conditioning, and iron-electrolyte compatibility. The initial candidate pool spanned PFSA CEMs, hydrocarbon-based CEMs, and AEMs. Following the transport and practical-feasibility screening, the final experimental shortlist comprised one PFSA CEM and two hydrocarbon CEMs. Selected membranes are summarised in Table 3.1; the full screening database is given in Appendix A.

Table 3.1: Final shortlist of membranes selected for experimental evaluation in this work.

Membrane	Material class	Chemistry
Nafion NR212	PFSA CEM	Perfluorosulfonic acid
Selemion CMVN	Hydrocarbon CEM	Crosslinked styrene-divinylbenzene
Membrane X	Hydrocarbon CEM	Commercially confidential

AEMs were included in the initial screening but were not advanced to the experimental programme. Preliminary in-house evaluation by Elestor B.V. indicated that the tested candidates did not satisfy the combined performance and cost requirements for the present HyFe application. As the underlying internal evaluation is not reproduced quantitatively in this thesis, the exclusion of AEMs is treated as a

practical scope decision rather than as a general conclusion that AEMs are unsuitable for acidic HyFe systems. The comparatively low mobility or stronger fixed-site association of sulfate and bisulfate counter-ions may have contributed to the observed AEM performance, but this mechanism was not investigated in the present work.

The framework relies predominantly on literature transport data measured under beginning-of-life conditions. Permeability is species- and electrolyte-specific, so values obtained using vanadium or other surrogate redox species cannot be assumed to represent Fe^{2+}/Fe^{3+} crossover directly. Furthermore, the figure of merit $S = \sigma/P$ reduces a multidimensional selection problem to a single conductivity–crossover ratio and does not independently represent chemical durability, swelling, cost, manufacturability, or long-term resistance evolution. These simplifications are appropriate for the intended purpose of reducing a broad candidate pool to a manageable experimental shortlist. The selected candidates are subsequently assessed under HyFe-relevant ex-situ and stack conditions, which provide candidate-level performance evidence beyond the literature-based screening.

3.2. In-Situ Characterisation: Single-Cell Stack Testing

This section describes the experimental procedures used to characterise the three membranes under representative Fe–H_2 operating conditions. It covers electrolyte preparation, membrane pre-treatment, stack assembly and quality verification, and the electrochemical cycling protocol. A schematic exploded view of a single cell stack with components is shown in Figure 3.2

3.2.1. Electrolyte Composition and Preparation

The electrolyte used in all in-situ cycling experiments was an aqueous iron sulfate solution in sulfuric acid, prepared from reagent-grade $FeSO_4 \cdot 7\,H_2O$, $Fe_2(SO_4)_3 \cdot 5\,H_2O$, and concentrated H_2SO_4 (95–97 % w/w). A fixed volume of electrolyte was prepared per test and circulated continuously through the electrolyte compartment of the stack during cycling. The electrolyte was prepared at $0\,\%$ SoC, such that iron was present entirely as Fe^{2+}; at $100\,\%$ SoC the iron is fully oxidised to Fe^{3+} at the same total iron concentration, with the free acid concentration reduced accordingly due to the change in sulfate speciation. All solutions were prepared in deionised water and homogenised thoroughly before use.

3.2.2. Stack Assembly

A single-cell Fe–H_2 stack with an active area of approximately $700\,\mathrm{cm}^2$ was assembled following a standardised laboratory procedure. Prior to assembly, all components were inspected for cleanliness and mechanical integrity, and the assembly environment was conditioned to a relative humidity of $50\,\%$ to limit membrane dehydration during handling.

The cell was built up sequentially on an alignment fixture using four positioning pins to ensure accurate layer registration. The complete layer sequence, shown schematically in Figure 3.2, starts from the bottom end plate and proceeds as follows: end plate, insulation plate, current collector, carbon-sheet contact layers, bipolar plate (electrolyte flow-field side up), contact layers, bipolar plate (hydrogen flow-field side down), liquid-diffusion layers (LDL; uncoated then coated), the ion-exchange membrane under test, and gas-diffusion electrode (GDE, catalyst side toward membrane), followed by the mirror-image sequence returning to the top end plate.

The membrane was handled with particular care. For NR212 and Membrane X, protective films were removed immediately before placement. CMVN required continuous hydration during handling and was kept wet throughout by spraying with deionised water to prevent drying. In all cases the membrane was laid flat and wrinkle-free, and the stack was closed without interruption to minimise dehydration.

Once the stack was closed, eight threaded rods with self-locking nuts were fitted. The assembly was placed under a hydraulic press and compacted in two stages: an initial compaction to seat all layers uniformly, followed by a final compaction to the target clamping force. All fasteners were then torqued to a specified value in a cross-pattern sequence, repeated twice, to ensure uniform clamping pressure across the active area.

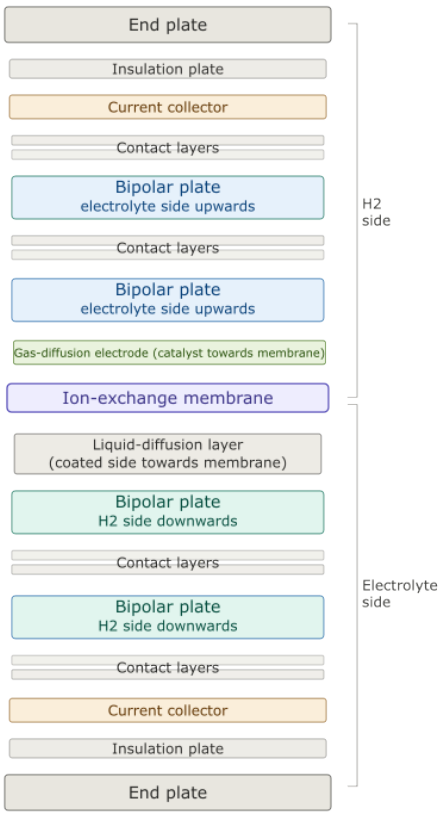


Figure 3.2: Exploded-view schematic of the single-cell Fe–H_2 stack, showing all functional layers in assembly order. The ion-exchange membrane separates the electrolyte side (bottom) from the hydrogen side (top).

3.2.3. Pre-Test Quality Verification

Before electrochemical testing, each assembled stack underwent three sequential quality checks to verify mechanical integrity, gas-tightness, and hydraulic pressure-drop. Only stacks passing all three checks proceeded to the cycling protocol; any non-conforming assembly was disassembled, inspected, and rebuilt.

The first check verified the leak-tightness of all sealing interfaces. Forming gas was applied to the hydrogen compartment and the electrolyte compartment was independently pressurised to defined gauge pressures. A calibrated hydrogen sniffer was traversed systematically along all external sealing surfaces; readings were required to remain below a specified threshold on all sides before the assembly was considered gas-tight.

The second check quantified the baseline hydrogen permeation rate through the membrane. Pure hydrogen was supplied to the hydrogen compartment at a defined gauge pressure while the electrolyte compartment was connected to a water-displacement volumetric cell. The volume of gas permeating through the membrane was measured over consecutive intervals and averaged to obtain a steady-state permeation rate. An acceptance criterion was applied; stacks exceeding this threshold were considered to have a damaged or improperly seated membrane.

The third check confirmed hydraulic continuity of the electrolyte flow circuit and established a single-cell pressure-drop baseline for later comparison with in-situ data collected during cycling. Deionised water was circulated through the electrolyte compartment at a defined flow rate and the steady-state pressure drop across the cell was recorded. Anomalous pressure drop values, relative to previously characterised stacks built with the same cell hardware, were taken as an indication of partial blockage

or misalignment in the flow field.

3.2.4. Membrane Pre-treatment

The three membranes required different pre-treatment procedures prior to stack assembly, reflecting differences in their as-received form and storage medium. Nafion NR212 and CMVN were used as received without further conditioning, as both are supplied in the proton form and are compatible with direct immersion in acidic electrolyte.

Membrane X is commercially supplied in a non-proton cationic form and stabilised with an alcohol, and therefore required conversion to the proton form before use. Pre-treatment was carried out in situ after stack assembly: rather than connecting the standard electrolyte supply, the stack was temporarily connected to a reservoir containing $1\,\mathrm{L}$ of $1\,\mathrm{mol\,L^{-1}}$ H_2SO_4 at $35\,^{\circ}\mathrm{C}$, which was circulated through the electrolyte compartment for $2\,\mathrm{h}$. The acid was then replaced with deionised water, which was circulated for $5\,\mathrm{min}$ to remove residual acid before the final electrolyte connections were made. This procedure establishes a well-defined, fully protonic starting state for Membrane X comparable to that of the other two membranes at the onset of cycling.

3.2.5. Operating Conditions and Cycling Protocol

The operating temperature differed across membranes and was set in accordance with each membrane's intended application range. NR212 and Membrane X were tested at $55\,^{\circ}\mathrm{C}$; CMVN was operated at $35\,^{\circ}\mathrm{C}$. The cycling protocol was otherwise identical for all three membranes and is summarised in Table 3.2. Nafion NR212 and Membrane X were tested using different single-cell stack systems, which

Table 3.2: Summary of in-situ cycling conditions for each membrane.

Membrane	Temperature (°C)	Electrolyte volume (L)	Break-in (×5 cycles)	Main cycling power
Nafion NR212	55	10	$35\,\mathrm{W}$	$45\,\mathrm{W}$
CMVN	35	5	-	-
Membrane X	55	5	$35\,\mathrm{W}$	$55\,\mathrm{W}$

differed in electrolyte reservoir volume ($10\,\mathrm{L}$ and $5\,\mathrm{L}$, respectively). As a result, at the same cycling power, each charge/discharge cycle took approximately twice as long in absolute time for NR212 as compared to Membrane X and CMVN. Consequently, the total cycling duration reported in hours (Section 4.1) is not directly comparable between these two membranes on a like-for-like basis. All stacks were cycled in constant-power mode using a battery-testing system (Neware, China). The upper cut-off voltage was 0.9V, whereas the lower cut-off voltage was 0.45V. For Membrane X, an initial break-in phase of five cycles at $35\,\mathrm{W}$ was applied to allow the electrolyte to equilibrate across the membrane and to condition the electrode–membrane interfaces before the primary test conditions were imposed. All subsequent cycles were performed at $55\,\mathrm{W}$. Similarly, for NR212, an initial break-in phase of five cycles at $35\,\mathrm{W}$ was applied, after which all cycles were at a constant power of $45\,\mathrm{W}$, whereas for CMVN, due to poor membrane performance, it was not possible to maintain a uniform power level which is discussed further in Section 4.1.3. Voltage, current, and power were logged continuously throughout. Ohmic cell resistance was extracted at regular intervals from voltage-step measurements during cycling, providing the in-situ $R(t)$ data used to quantify membrane resistance evolution, as described in Section 4.1.

3.2.6. Apparent Beginning-of-Charge Resistance Extraction

An apparent beginning-of-charge (BOC) cell-resistance indicator was extracted from the voltage response following each rest-to-charge transition. For a general current step, the resistance estimate is

$$R_{\mathrm{app}} = \frac{\Delta V}{\Delta I} = \frac{V(t_s) - V_{\mathrm{pre}}}{I(t_s) - I_{\mathrm{pre}}}, \tag{3.4}$$

where V_{pre} and I_{pre} are the voltage and current immediately before the transition, and $V(t_s)$ and $I(t_s)$ are evaluated at a specified time t_s after the transition.

Following the resistance definition implemented for the present Neware dataset, $t_s = 10\ \mathrm{s}$ was used. Because the current during the preceding rest step was approximately zero, the BOC resistance was calculated as

$$R_{\mathrm{BOC,10s}} = \frac{V_{\mathrm{10s}}^{\mathrm{chg}} - V_{\mathrm{OCV}}^{\mathrm{pre\text{-}chg}}}{I_{\mathrm{10s}}^{\mathrm{chg}}}, \tag{3.5}$$

where $V_{\mathrm{OCV}}^{\mathrm{pre\text{-}chg}}$ is the final voltage sample recorded during the immediately preceding rest step, and $V_{\mathrm{10s}}^{\mathrm{chg}}$ and $I_{\mathrm{10s}}^{\mathrm{chg}}$ are the voltage and current measured $10\ \mathrm{s}$ after the charge step begins. Positive current denotes charge.

The resulting quantity is referred to throughout this thesis as the *apparent BOC cell resistance*. It may include contributions from the membrane, electrolyte, electrical and interfacial contacts, electrodes, and short-time polarisation. Its value lies in providing a consistently defined indicator that can be tracked over long-duration cycling.

A usable apparent BOC resistance series was obtained for Membrane X and the selected NR212 comparison dataset. The unstable transitions observed during the CMVN test prevented extraction of a sufficiently consistent BOC resistance series for quantitative fitting.

To describe the long-term curvature of the usable resistance trajectories, the data were fitted to the empirical saturating exponential

$$R(t) = R_0 + \Delta R_{\max}\left[1 - \exp(-k_{\mathrm{obs}}t)\right], \tag{3.6}$$

where R_0 is the fitted resistance intercept at $t = 0$, $\Delta R_{\max}$ is the fitted asymptotic resistance increment, and k_{obs} is the observed pseudo-first-order rate coefficient. The parameters were estimated by nonlinear least-squares regression using `lsqcurvefit` in MATLAB.

Because the first valid BOC measurement may occur after the beginning of the recorded cycling interval, R_0 is interpreted as a fitted $t = 0$ intercept rather than necessarily as a directly measured initial resistance. The fitted asymptotic resistance is

$$R_{\mathrm{sat}} = R_0 + \Delta R_{\max}. \tag{3.7}$$

A characteristic fit metric, t_{99}, was defined as the time required for the fitted relationship to reach 99% of $\Delta R_{\max}$:

$$t_{99} = -\frac{\ln(0.01)}{k_{\mathrm{obs}}}. \tag{3.8}$$

Where t_{99} extends beyond the experimental observation window, it is reported as a fit-based extrapolation rather than as a directly observed saturation time. Equation (3.6) is used as a descriptive representation of the resistance curvature and does not, by itself, uniquely identify the physical mechanism responsible for the measured resistance evolution. The fitting procedure was applied to the Membrane X and NR212 datasets; it was not applied to CMVN because no reliable BOC resistance time series was available.

3.2.7. Cycling-Data and Exclusion Criteria

The NR212 stack assembled and operated during the present thesis did not yield a sufficiently reliable long-duration apparent BOC resistance series for quantitative comparison. The affected dataset was therefore excluded from the resistance-growth analysis. The corresponding measurement issue is documented in Figure H.1.

For the NR212 comparison, a historical HyFe cycling dataset from a separate single-cell stack assembled and operated independently at Elestor B.V. before the start of this thesis was used, after consultation with the project supervisors. The dataset was selected because it contained a continuous

long-duration BOC resistance series obtained using the same general resistance-extraction principle. It is identified throughout the thesis as a historical comparison dataset rather than as an experimental replicate generated in the present work. Relevant differences in stack configuration, electrolyte volume, operating power, and test duration are reported alongside the results. Consequently, the comparison with Membrane X is interpreted as candidate-level performance evidence under the respective documented test configurations, rather than as a fully controlled like-for-like material comparison.

The CMVN stack completed several isolated charge–discharge cycles, but stable uninterrupted cycling was not maintained. The abrupt and irregular transitions prevented extraction of a consistent apparent BOC resistance time series. CMVN is therefore evaluated from its observed current–voltage behaviour and operational stability, but is not included in the saturating-exponential resistance fitting.

3.3. SEM-EDS Sample Preparation

Following extraction from the stack, cycled membrane samples were cleaned prior to imaging to remove loosely-associated surface material. Each sample was first sonicated in ultrapure water for 10 minutes, then soaked in a fresh ultrapure water bath for at least 24 hours under static conditions. Samples were subsequently dried in a convection oven, as residual moisture is electrically conductive and interferes with SEM-EDS imaging and quantification. Drying was required for high-vacuum SEM analysis but may alter the hydrated membrane morphology and the chemical or spatial state of retained iron. In particular, residual mobile iron may oxidise, redistribute, or precipitate as water is removed. The SEM–EDS observations therefore represent the post-washing, oven-dried sample state rather than the original in-operando hydrated membrane state. Cleaned, dried samples were mounted on aluminium stubs using conductive carbon tape.

Imaging was performed on a Hitachi FlexSEM 1000. Pristine (uncycled) reference samples were imaged in secondary-electron (SE) mode at an accelerating voltage of 5 kV and a working distance of 5 mm, favouring spatial resolution of surface morphology. EDS analysis was performed at an accelerating voltage of 15 kV and a working distance of 10 mm, using a Bruker QUANTAX 80 EDS system with ESPRIT Compact software; the longer working distance corresponds to the system's designed analytical geometry, ensuring the sample is positioned along the detector's calibrated take-off angle for accurate quantification.

Three categories of location were analysed for each cycled sample: pristine (uncycled) reference points, used to establish a baseline and identify any pre-existing surface contamination; nominally featureless ("matrix") points on the cycled surface, showing no visible particulate; and visible surface particulates, analysed individually to determine their elemental identity.

3.4. Ex-Situ Iron Sorption Study: Membrane Immersion Test

An ex-situ membrane immersion study was conducted to quantify iron uptake into the membranes under purely diffusive and static conditions, that is, without an applied electric field, and to determine whether the membrane exhibits a preferential affinity for Fe^{2+} or Fe^{3+}. This distinction is relevant because in an operating Fe–H_2 cell, the iron speciation in the electrolyte changes continuously with SoC during cycling. If Fe^{3+} binds to sulfonate groups at a significantly higher rate than Fe^{2+}, resistance growth will be more pronounced during the charge half-cycle when Fe^{3+} dominates. The ex-situ setup isolates membrane-specific retained-iron behaviour under the two nominal exposure conditions.

Two electrolyte conditions were tested in parallel: a fully discharged electrolyte at SoC $= 0\%$, containing nominally pure Fe^{2+}, and a fully charged electrolyte at SoC $= 100\%$, containing nominally pure Fe^{3+}. Both electrolytes were prepared at a total iron concentration of 1 M in 2-2.5 M H_2SO_4. Iron uptake was measured at five time points: 1, 2, 5, 12, and 16 days, with a separate membrane sample allocated to each time point so that intermediate measurements did not disturb the equilibrium state of the remaining samples.

3.4.1. Membrane pretreatment

All samples were cut from a single sheet to minimise variability in thickness, IEC, and surface condition between samples. Prior to immersion, each sample was conditioned through a three-step sequence to establish a reproducible, protonated initial state. The sample was first dried in a convection oven

at 80 °C for a minimum of 4 hours to remove all residual water, and the dry mass m_{dry} was recorded immediately upon removal. It was then soaked in ultrapure water for at least 15 minutes to restore the water content of the membrane without introducing ionic contaminants. Finally, the rehydrated sample was transferred to 1 M H_2SO_4 and soaked for at least 2 hours, which converts ion exchange sites to the H^+ form. This acid conditioning step provides a well-defined starting point for the subsequent iron exchange and ensures that any iron detected in the final extract originated exclusively from the immersion step.

3.4.2. Electrolyte immersion and iron extraction

Immediately after acid conditioning, each sample was rinsed briefly with ultrapure water and transferred to the target electrolyte. Samples were immersed in sealed containers at 55 $\pm$ 1 °C for the designated period. At the end of the immersion period, each sample was subjected to a sequential extraction procedure designed to isolate only the iron that is retained in the membrane.

The sample was first rinsed with ultrapure water to remove bulk electrolyte adhering to the surface, then placed in a fresh ultrapure water bath and subjected to sonication for 10 minutes to dislodge loosely associated iron from the pore space. The sonicated sample was subsequently soaked in a further volume of fresh ultrapure water for 24 hours under static conditions, allowing residual pore-water iron to diffuse out by concentration-gradient equilibration. In the final step, the cleaned sample was transferred to 15 mL of 1 M NaCl solution and soaked for at least 48 hours; Na^+ ions competitively displace the iron ions occupying the sulfonate exchange sites, releasing them quantitatively into solution. The NaCl extract was then collected for iron quantification.

The rationale for this sequence is that the progressive water washes selectively remove iron that is electrostatically mobile and not site-bound, while the NaCl exchange releases only the iron that has displaced protons from the sulfonate groups.

3.4.3. Iron quantification and data reduction

The total iron concentration in each NaCl extract was determined using the UV-Vis spectrophotometric method described in Section 3.5, using the low-concentration sample preparation route. Since the immersion vials do not have accurate volumetric markings, the NaCl extract was first transferred to a 50 mL volumetric flask and filled to the mark before measurement. The total moles of iron extracted per sample were computed from Equation (3.11) with $V_{\mathrm{sample}} = 50$ mL.

The resulting time series $\{t_i,\, n_{\mathrm{Fe}}(t_i)\}$ for each SoC condition constitutes the primary experimental output. Comparison of the Fe^{2+} and Fe^{3+} curves could reveal whether the membrane exhibits a preferential binding affinity for either species.

3.5. Total Iron Quantification by UV-Vis Spectrophotometry

Total dissolved iron concentration in aqueous samples was determined by UV-Vis spectrophotometry using the 1,10-phenanthroline complexation method. The method is based on the quantitative formation of the iron(II)–phenanthroline complex (ferroin), which absorbs strongly at 510 nm according to:

$$\mathrm{Fe}^{2+} + 3\,\mathrm{C_{12}H_8N_2} \longrightarrow \left[\mathrm{Fe(C_{12}H_8N_2)_3}\right]^{2+} \tag{3.9}$$

Since only Fe^{2+} participates in complex formation, all Fe^{3+} present in the sample is first reduced to Fe^{2+} by hydroxylammonium chloride (NH_3OHCl) prior to complexation. The measured absorbance therefore reflects the total iron content regardless of speciation, making the method equally applicable to fully charged (Fe^{3+}-rich), fully discharged (Fe^{2+}-rich), and mixed-valence samples.

3.5.1. Sample preparation

All glassware was cleaned three times with 0.5–1.0 M H_2SO_4 followed by three rinses with ultrapure water before use. A reagent blank, prepared by performing all steps without sample addition, was included in each measurement batch to correct for background absorbance from the reagents. All samples were prepared in triplicate.

The preparation route depended on the expected iron concentration. For high-concentration samples such as bulk electrolyte ($[\mathrm{Fe}] \gtrsim 0.1$ mol L^{-1}), a primary dilution was first prepared by adding 1.0 mL of sample to a 100 mL volumetric flask pre-filled with approximately 50 mL ultrapure water and 2.5 mL concentrated H_2SO_4, then filled to the mark; 250 μL of this primary dilution was then taken forward. For low-concentration samples such as membrane extracts and crossover solutions, no primary dilution was performed and 250 μL of the undiluted sample was taken directly.

In both cases, the 250 μL aliquot was pipetted into a 50 mL volumetric flask and the following reagents were added sequentially, with 15 minutes of equilibration time after each addition: (1) 1.0 mL hydroxylammonium chloride solution (10 g per 100 mL), which reduces all Fe^{3+} to Fe^{2+}; (2) 2.5 mL of 1 g L^{-1} 1,10-phenanthroline solution, which forms the orange-red ferroin complex; and (3) 4.0 mL acetate buffer (0.065 M acetic acid – 0.035 M sodium acetate), which stabilises the complex at pH ≈ 4.5. The flask was subsequently filled to the mark with ultrapure water and homogenised.

3.5.2. Absorbance measurement and Concentration calculation

Measurements were performed on a Shimadzu UV-1900i spectrophotometer using a 10 mm path length quartz cuvette. The instrument was allowed to warm up for 30 minutes before use. Autocorrection was performed against the reagent blank at 510 nm prior to each sample series. Three absorbance readings were recorded per sample and averaged.

The total iron concentration was computed from the averaged absorbance using the calibration relationship established from standard solutions of known Fe^{2+} concentration:

$$[\mathrm{Fe}_{\mathrm{total}}] = \frac{A_{510} - A_0}{\varepsilon} \times f_{\mathrm{dil}} \tag{3.10}$$

where A_{510} is the measured absorbance, $A_0 = 8.1 \times 10^{-4}$ is the blank intercept, $\varepsilon = 478.8\ \mathrm{L\,mol^{-1}}$ is the molar absorptivity from the calibration line, and f_{dil} is the overall dilution factor accounting for all preparation steps. The total moles of iron in a sample of volume V_{sample} are then:

$$n_{\mathrm{Fe}} = [\mathrm{Fe}_{\mathrm{total}}] \times V_{\mathrm{sample}} \tag{3.11}$$

This procedure is used throughout this work wherever iron quantification from aqueous samples is required.

3.6. Ex-Situ Characterisation: H-Cell Resistance-Growth Test

A temperature-controlled H-cell was used to monitor the evolution of the apparent high-frequency cell resistance during symmetric exposure of Membrane X to iron-containing electrolyte. The experiment was conducted without an imposed DC current and without net electrochemical cycling, thereby removing the sustained migration field, Faradaic conversion, and changing state of charge present during stack operation.

The H-cell measurement nevertheless does not isolate the membrane resistance completely. Because a two-electrode configuration was used, the measured high-frequency resistance contains contributions from the membrane, electrolyte, graphite electrodes, electrical contacts, and cell geometry. These contributions were maintained as consistently as possible throughout the test. The time-dependent signal is therefore interpreted as an apparent high-frequency H-cell resistance-growth indicator.

The Membrane X resistance-growth experiment described here provides the experimental basis for estimating the effective concentration-normalised coefficient k_{block} used in the reduced-order model. The effective membrane ionic conductivity κ_{eff} used in the transport-field closure was not obtained from this resistance-growth fit; its adopted value and source are reported separately in Table B.1.

3.6.1. Setup Description and Assembly

The H-cell consisted of two symmetric double-walled glass half-cells clamped together with the membrane positioned between two EPDM gaskets. The O-ring aperture had a diameter of 14.47 mm, cor-

responding to an exposed membrane area of approximately $1.64\ \mathrm{cm}^2$. The O-rings defined the active area and provided a leak-tight seal between the two liquid compartments.

Temperature control was achieved by circulating thermostatic fluid through the double walls of both half-cells using a recirculating bath (Julabo). The bath setpoint was adjusted to obtain an electrolyte temperature of $55\ ^\circ\mathrm{C}$, which was verified periodically using a calibrated thermometer inserted through the PTFE lid of one half-cell.

Before assembly, Membrane X was converted to the proton form and hydrated using the membrane-specific conditioning procedure described in Section 3.2.4.

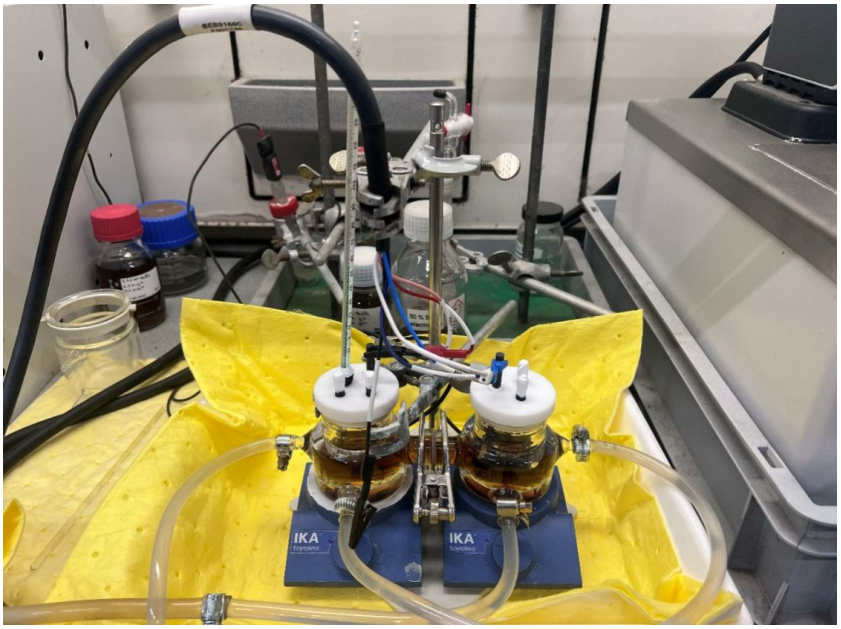


Figure 3.3: Assembled H-cell used for the symmetric ex-situ resistance-growth experiment. The membrane was sealed between two double-walled glass half-cells using EPDM gaskets. Graphite rods served as the working electrode and the combined counter/reference electrode in the two-electrode impedance configuration. Temperature was controlled using a recirculating bath connected to the double walls.

Each half-cell was equipped with a cylindrical graphite electrode inserted through a PTFE screw lid and sealed using O-rings and PTFE tape. The immersed length of each graphite electrode was fixed at $4.2\ \mathrm{cm}$, measured from the inner face of the PTFE lid. The inter-electrode spacing was recorded before each experiment and maintained throughout the corresponding test.

Both half-cells contained magnetic stir bars operated at the same low stirring rate. Stirring was used to reduce bulk concentration and temperature gradients while avoiding visibly vigorous flow near the membrane. This procedure does not imply the complete absence of convection; rather, the same hydrodynamic condition was maintained on both sides of the symmetric cell.

Electrochemical measurements were performed using a BioLogic SP-150e potentiostat in a two-electrode configuration. One graphite rod was connected as the working electrode, while the counter and reference leads were connected together to the opposing graphite rod. Potentiostatic electrochemical impedance spectroscopy was performed using an instrument-set sinusoidal amplitude of $50\ \mathrm{mV}$ over the frequency range $20\ \mathrm{kHz}$ to $140\ \mathrm{Hz}$, with logarithmic spacing of six points per decade. Instrument quality indicators were enabled to identify visibly non-stationary or non-linear responses.

The apparent high-frequency resistance, $R_{\Omega,\mathrm{H}}$, was obtained from the high-frequency real-axis intercept of the Nyquist response using EC-Lab. Because the complete two-electrode H-cell response was measured, the extracted value was not converted directly into an isolated membrane conductivity for the resistance-growth analysis.

3.6.2. Resistance Evolution in Iron-Containing Electrolyte

The resistance-growth experiment was performed using a nominally 50%-SoC iron electrolyte prepared by volumetrically mixing the fully ferrous and fully ferric stock electrolytes in equal proportions, as described in Section 3.2.1. Both half-cells were filled with $50\ \mathrm{mL}$ of the same electrolyte, preheated to $55\ ^\circ\mathrm{C}$.

Using identical bulk electrolyte compositions on both sides removes an imposed left-to-right concentration difference and therefore suppresses a sustained directional chemical-potential driving force across the membrane. The condition does not prevent iron from partitioning from each bulk solution into the membrane or interacting with membrane fixed-charge sites. The experiment is consequently described as a *symmetric, zero-DC-bias exposure* rather than as a strictly "zero-field diffusion" experiment, because the impedance measurement itself applies a small oscillatory electric perturbation.

Any visible air trapped at the membrane surface was removed immediately after filling by carefully tilting the cell and aspirating the bubble using a plastic pipette. PEIS measurements were initiated as soon as practicable after electrolyte addition. The time origin used for fitting was defined as the time of the first accepted impedance measurement; any uptake or hydration occurring before that measurement was therefore not resolved explicitly.

Spectra were acquired more frequently during the initial period and at longer intervals later in the experiment. The complete measurement-time sequence is retained in the experimental dataset. The resulting $R_{\Omega,\mathrm{H}}(t)$ trajectory is used as an apparent membrane-associated resistance-growth signal. The fixed cell geometry and symmetric electrolyte conditions support this interpretation, but the experiment does not uniquely separate changes in the membrane from slow changes in the electrodes, contacts, or electrolyte response.

The resistance trajectory was represented using the empirical saturating exponential

$$R_{\Omega,\mathrm{H}}(t) = R_0 + (R_{\mathrm{sat}} - R_0)\left[1 - \exp(-k_{\mathrm{obs}}t)\right], \tag{3.12}$$

where R_0 was fixed at the first accepted resistance measurement, R_{sat} was the fitted asymptotic resistance, and k_{obs} was the fitted pseudo-first-order resistance-growth coefficient. R_{sat} and k_{obs} were obtained by nonlinear least-squares regression using `lsqcurvefit` in MATLAB. Fit-based confidence intervals were calculated using `nlparci`.

Equation (3.12) has the same mathematical form as the finite-capacity resistance-growth relationship used in the reduced-order model. The fitted curvature is compatible with such a process but does not, by itself, demonstrate that iron–sulfonate site occupation is the unique cause of the measured resistance increase.

The external iron concentration was treated as effectively constant during the H-cell experiment. Each $50\ \mathrm{mL}$ half-cell contained approximately $50\ \mathrm{mmol}$ total iron, whereas the exchange capacity of the exposed membrane coupon was only of micromole order. Membrane uptake therefore represented a negligible fraction of the external iron inventory.

The concentration used to normalise k_{obs} was the extended-ideal Donnan estimate of the total mobile iron concentration in the membrane-water phase under the nominal 50%-SoC condition:

$$C_{\mathrm{Fe,mem}}^{\mathrm{H-cell}} = K_{\mathrm{Fe^{2+}}} c_{\mathrm{Fe^{2+}}}^{\mathrm{bulk}} + K_{\mathrm{Fe^{3+}}} c_{\mathrm{Fe^{3+}}}^{\mathrm{bulk}}. \tag{3.13}$$

The partition coefficients were calculated using the extended-ideal Donnan treatment described in Section 3.9.3 and Appendix C, including the sulfate–bisulfate electrolyte composition. All concentrations in Equation (3.13) were expressed in $\mathrm{mol\,m^{-3}}$ when calculating the rate coefficient.

Under the constant-concentration approximation,

$$k_{\mathrm{obs}} = k_{\mathrm{block}} C_{\mathrm{Fe,mem}}^{\mathrm{H-cell}}, \tag{3.14}$$

so that

$$k_{\mathrm{block}} = \frac{k_{\mathrm{obs}}}{C_{\mathrm{Fe,mem}}^{\mathrm{H-cell}}}. \tag{3.15}$$

The resulting k_{block} has units of $\mathrm{m^3\,mol^{-1}\,s^{-1}}$ and is interpreted as an *effective concentration-normalised resistance-growth coefficient*. It is not treated as an intrinsic microscopic adsorption constant.

The coefficient was transferred to the Membrane X stack model without additional fitting. This transfer is conditional on the selected concentration closure: the H-cell normalisation uses a symmetric membrane-phase Donnan concentration, whereas the nominal stack model uses the effective hydrogen-side boundary concentration defined in Section 3.9.5. The resulting comparison therefore tests whether the H-cell-derived effective timescale remains compatible with the normalised stack resistance trajectory under the adopted reduced-order description.

3.7. Water Uptake Measurement

Membrane samples were cut to the required size and pretreated where necessary, then dried in an oven at 80°C overnight to obtain the dry mass. Samples were subsequently immersed in ultrapure (UP) water overnight. Surface water was removed by gently shaking the membrane while holding it with plastic tweezers (cleaned prior to use), after which the wet mass was recorded. Samples were re-immersed in UP water for approximately 4 h and the wet mass measured again following the same procedure. This immersion-and-weighing step was repeated a third time, and the average of the three wet mass measurements was used to calculate the water uptake (WU):

$$\mathrm{WU} = \frac{m_{\mathrm{wet}} - m_{\mathrm{dry}}}{m_{\mathrm{dry}}} \times 100\% \tag{3.16}$$

Results are reported in Table H.3 (Membrane X) and Table H.4 (CMVN), Appendix H.

3.8. Ion Exchange Capacity Measurement

Membrane samples were dried in an oven at 80°C overnight and the dry mass recorded. Samples were then soaked in UP water for at least 15 min, followed by immersion in 1 M H_2SO_4 for at least 4 h to protonate the membrane. To exchange H^+ for Na^+, samples were subsequently soaked in 1 M NaCl for at least 48 h after being rinsed with UP water.

The H^+ released into the NaCl solution was quantified by titration with NaOH using a Metrohm Autolab autotitrator to determine the equivalence point (EP). The NaOH concentration was first standardised in triplicate against a precisely known oxalic acid concentration. The NaCl solutions were then titrated in triplicate with the standardised NaOH. The IEC was calculated as:

$$\mathrm{IEC} = \frac{C_{\mathrm{NaOH}} \cdot V_{\mathrm{NaOH}}}{m_{\mathrm{dry}}} \tag{3.17}$$

where C_{NaOH} and V_{NaOH} are the concentration and volume of NaOH added at the equivalence point, and m_{dry} is the dry mass of the membrane. Results are reported in Table H.6 (CMVN), Appendix H.

3.9. Transport Model: Formulation, Assumptions, and Governing Equations

The model is formulated as a physics-informed, hybrid reduced-order $0\mathrm{D}$–$1\mathrm{D}$ system. The slowly evolving iron inventories and resistance-growth state are represented by zero-dimensional ordinary differential equations, while the instantaneous Fe^{2+} and Fe^{3+} transport problem is resolved in one spatial dimension across the membrane thickness. At each ODE evaluation, a quasi-steady Nernst–Planck boundary-value problem (BVP) returns the membrane concentration profiles and species fluxes. The transport solution then drives a single lumped resistance-growth state.

The formulation is not intended as a complete multiphase model of the stack. Diffusion, electromigration, Faradaic conversion, and aqueous-side Donnan partitioning are represented explicitly. The hydrogen-side interface, supporting-ion transport, and resistance-growth relationship are introduced as reduced-order closures. The coupling is one-way: transport affects the resistance-growth state, but the calculated resistance increase does not update the diffusivities, effective ionic conductivity, fixed-charge concentration, or Donnan coefficients. Figure 3.4 summarises the model architecture, inputs, and outputs.

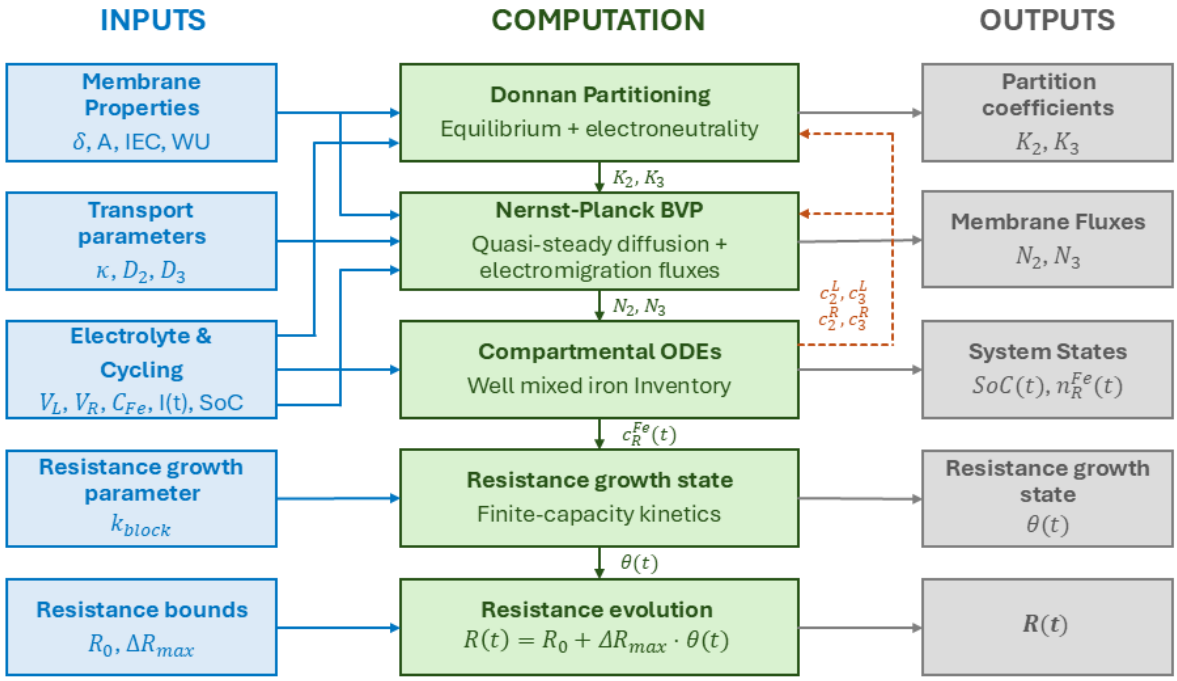


Figure 3.4: Schematic overview of the hybrid reduced-order 0D–1D model. Time-dependent bulk inventories and the resistance-growth state are represented by zero-dimensional ODEs, while Fe^{2+}/Fe^{3+} transport is solved quasi-steadily in one dimension across the membrane. The effective coefficient k_{block} is obtained from the Membrane X H-cell resistance-growth experiment under symmetric, zero-DC-bias exposure. The principal model comparison concerns the normalised stack-resistance trajectory.

3.9.1. Timescale Separation and Quasi-Steady Membrane Transport

The characteristic through-thickness diffusion time of species i is estimated as

$$t_{\mathrm{diff},i} = \frac{\delta^2}{D_i}, \tag{3.18}$$

where δ is the membrane thickness and D_i is the adopted effective membrane-phase diffusivity. For Membrane X, $\delta = 20\ \mu\mathrm{m}$, $D_{\mathrm{Fe}^{2+}} = 1.70 \times 10^{-10}\ \mathrm{m^2\,s^{-1}}$, and $D_{\mathrm{Fe}^{3+}} = 1.428 \times 10^{-10}\ \mathrm{m^2\,s^{-1}}$. Equation (3.18) therefore gives approximately $2.35\ \mathrm{s}$ for Fe^{2+} and $2.80\ \mathrm{s}$ for Fe^{3+}. These times are much shorter than the hours-scale cycling dynamics and the hundreds-of-hours resistance evolution.

Transient storage is therefore neglected within the spatial membrane subproblem. At each time, the membrane concentration profiles are assumed to have relaxed to quasi-steady, non-equilibrium profiles corresponding to the instantaneous boundary concentrations and applied current. The profiles may remain nonuniform and carry nonzero flux; the quasi-steady approximation does not imply a uniform membrane concentration or thermodynamic equilibrium.

The resulting architecture contains:

1. **Zero-dimensional dynamic states.** The iron-electrolyte tank, an effective hydrogen-side hydrated boundary state, and the global resistance-growth state are spatially lumped and evolve in time.

2. **One-dimensional quasi-steady membrane transport.** At each ODE evaluation, a steady Nernst–Planck BVP is solved across $0 \leq x \leq \delta$. The resulting Fe^{2+} and Fe^{3+} fluxes are returned to the inventory balances.

This hybrid treatment preserves the minimum spatial resolution required to represent membrane thickness, Donnan-partitioned boundary concentrations, diffusion, and electromigration, while remaining computationally tractable for long-duration cycling simulations.

3.9.2. Nernst-Planck Transport and Electric-Field Closure

The membrane subproblem belongs to the reduced solution–diffusion class of ion-exchange-membrane models commonly associated with the Teorell–Meyer–Sievers (TMS) framework. The hydrated membrane is represented as a macroscopically homogeneous charged phase, ionic transport is described using the Nernst–Planck equation, local electroneutrality is assumed within the membrane-water phase, and Donnan equilibrium is used to relate the membrane composition to an adjacent aqueous electrolyte phase [39]. Homogeneity refers to the adopted effective membrane properties; the Fe^{2+} and Fe^{3+} concentrations may still vary through the membrane thickness.

The present implementation retains these core TMS concepts but is not a complete multi-ion TMS model. Only Fe^{2+} and Fe^{3+} are resolved spatially, the electric field is represented by an effective Ohmic closure, and the dry-hydrogen-side boundary is treated using the model-specific reduced closure introduced in Section 3.9.3. The working Nernst–Planck expression is derived from electrochemical thermodynamics following Newman and Thomas-Alyea [36].

The electrochemical potential of species i is

$$\mu_i = \mu_i^0 + R_\mathrm{g} T \ln a_i + z_i F \phi, \tag{3.19}$$

where a_i is activity, z_i is charge number, F is Faraday's constant, R_g is the gas constant, T is temperature, and ϕ is electric potential. Within the framework of linear irreversible thermodynamics, the molar flux is proportional to the electrochemical potential gradient,

$$\mathbf{N}_i = -u_i c_i \nabla \mu_i + c_i \mathbf{v}, \tag{3.20}$$

where u_i is ionic mobility and $\mathbf{v}$ is bulk convection velocity. Bulk convection is neglected in the dense hydrated membrane phase ($\mathbf{v} = 0$), consistent with the low hydraulic permeabilities and small electro-osmotic velocities reported for Nafion-type membranes [40], [46]. Applying the Nernst–Einstein relation $u_i = D_i / R_\mathrm{g} T$, where D_i is an effective diffusivity for the hydrated membrane phase, gives

$$\mathbf{N}_i = -\frac{D_i c_i}{R_\mathrm{g} T} \nabla \mu_i. \tag{3.21}$$

Using the effective-ideality approximation $a_i \approx c_i$ gives the one-dimensional flux expression

$$N_i = -D_i \frac{\partial c_i}{\partial x} + z_i \frac{D_i F}{R_\mathrm{g} T} c_i E, \qquad i \in \{\mathrm{Fe}^{2+}, \mathrm{Fe}^{3+}\}, \tag{3.22}$$

where $E = -\partial \phi / \partial x$. No homogeneous reaction is included inside the transport domain, so

$$\frac{\partial N_i}{\partial x} = 0. \tag{3.23}$$

Equation (3.22) requires specification of the electric field E. In a full Poisson–Nernst–Planck formulation, this would be obtained by coupling the species-transport equations to Poisson's equation. The electroneutrality approximation already invoked above is appropriate at the homogenised membrane scale resolved in the present model: charge separation is confined primarily to interfacial or strongly

confined regions whose characteristic length and relaxation time are much smaller than the $20\ \mu\mathrm{m}$ membrane thickness and the seconds-to-hours timescales considered here, becoming questionable principally on nanometre and nanosecond scales [47]. Such local space-charge structure is not resolved explicitly in the present continuum model; its equilibrium effect at the aqueous electrolyte–membrane interface is instead represented through the Donnan boundary condition (Section 3.9.3).

The present BVP resolves only Fe^{2+} and Fe^{3+}, while proton, bisulfate, and sulfate transport are represented implicitly; the full multi-ion current balance is therefore not solved. Instead, under galvanostatic operation, the measured cell current is converted to the membrane current density,

$$j(t) = \frac{I(t)}{A}, \tag{3.24}$$

and the field is approximated using the effective Ohmic closure

$$E(t) = \frac{j(t)}{\kappa_{\mathrm{eff}}}, \tag{3.25}$$

where κ_{eff} is the adopted effective membrane ionic conductivity, with field orientation fixed by the physical cell geometry and electrode assignment. These supporting species' aggregate contribution to charge transport is represented through κ_{eff}, while their equilibrium concentrations enter the aqueous-side Donnan calculation. This algebraic relation avoids solving a separate potential equation and is consistent with treating the membrane as a homogeneous macroscopic ionic conductor [39]. This treatment is further supported by evidence that counter-ions immobilized at fixed-charge sites do not contribute proportionally to ionic transport [48]. It remains a reduced field closure rather than the complete multi-ion electrical description of the classical TMS model.

The adopted Fe^{2+} diffusivity is taken from measurements in water-saturated Nafion NR211, selected as the closest available PFSA analogue by thickness. In the absence of a direct Fe^{3+} measurement for Nafion or Membrane X, its diffusivity is estimated by scaling the measured Fe^{2+} value using the corresponding aqueous diffusivity ratio. The adopted values and sources are listed in Table B.1 [49], [50].

3.9.3. Extended-Ideal Donnan Partitioning and Boundary Conditions

Consistent with the TMS treatment of an ion-exchange membrane in contact with an aqueous electrolyte, equality of electrochemical potential is imposed at the iron-electrolyte–membrane interface [51]. Under the extended-ideal approximation used here, this gives the Donnan relation

$$K_i \equiv \frac{c_i^{\mathrm{mem}}}{c_i^{\mathrm{sol}}} = \exp\left(-\frac{z_i F \phi_D}{R_{\mathrm{g}} T}\right). \tag{3.26}$$

where $\phi_D = \phi_{\mathrm{mem}} - \phi_{\mathrm{sol}}$. The bulk electrolyte contains H^+, Fe^{2+}, Fe^{3+}, HSO_4^-, and SO_4^{2-}. Sulfate–bisulfate speciation is calculated from the prescribed analytical electrolyte composition and

$$K_{a,2} = \frac{c_{\mathrm{H^+}}^{\mathrm{sol}} c_{\mathrm{SO_4^{2-}}}^{\mathrm{sol}}}{c_{\mathrm{HSO_4^-}}^{\mathrm{sol}}}. \tag{3.27}$$

The Donnan potential is obtained by enforcing electroneutrality in the membrane-water phase:

$$c_{\mathrm{H^+}}^{\mathrm{mem}} + 2c_{\mathrm{Fe^{2+}}}^{\mathrm{mem}} + 3c_{\mathrm{Fe^{3+}}}^{\mathrm{mem}} - c_{\mathrm{HSO_4^-}}^{\mathrm{mem}} - 2c_{\mathrm{SO_4^{2-}}}^{\mathrm{mem}} = c_{\mathrm{fix}}. \tag{3.28}$$

The fixed-charge concentration per unit membrane-water volume is estimated from IEC and water uptake as

$$c_{\mathrm{fix}} = \frac{\mathrm{IEC}}{\mathrm{WU}}, \tag{3.29}$$

using a water density of approximately $1\ \mathrm{kg\,L^{-1}}$. Water uptake measured in pure water is used as a first-order estimate of membrane hydration in the operating electrolyte.

At each ODE evaluation, the total left-tank Fe concentration and SoC are used to recalculate the aqueous speciation, Donnan potential, and Fe^{2+}/Fe^{3+} partition coefficients. The membrane-side left boundary is therefore

$$c_2(0,t) = K_{2,L}(t)c_{2,L}(t), \qquad c_3(0,t) = K_{3,L}(t)c_{3,L}(t). \tag{3.30}$$

The opposite membrane face is adjacent to the hydrogen GDE rather than a bulk aqueous electrolyte. Fe ions do not possess a meaningful concentration or activity in the dry hydrogen phase, so a second Donnan equilibrium is not imposed. The right boundary is instead closed through an effective zero-dimensional hydrated boundary state:

$$c_i(\delta,t) = c_{i,R}^{\mathrm{eff}}(t) = \frac{n_{i,R}(t)}{V_{R,\mathrm{eff}}}, \qquad i \in \{2,3\}. \tag{3.31}$$

Equation (3.31) is a concentration-continuity closure, not partitioning into hydrogen gas. The state represents unresolved temporary storage of mobile iron in hydrated membrane-adjacent material, which may include ionomer or retained crossover liquid near the GDE. It allows a finite back-concentration to develop rather than imposing either a permanent perfect sink or an impermeable boundary.

The corresponding physical hydrated inventory was not measured independently. The numerical value of $V_{R,\mathrm{eff}}$ is therefore estimated from membrane water uptake and used as a characteristic hydrated-volume scale. It is not interpreted as a literal geometric identification of the complete membrane pore-water volume with a separate downstream compartment. Accordingly, $c_{i,R}^{\mathrm{eff}}$ is a model-effective boundary concentration, not a measured Fe concentration in the hydrogen gas or GDE.

3.9.4. Zero-Dimensional Inventory Evolution and OCV Assimilation

Let $n_{2,L}$ and $n_{3,L}$ denote the Fe^{2+} and Fe^{3+} inventories in the iron-electrolyte tank, and let $n_{2,R}$ and $n_{3,R}$ denote the corresponding mobile inventories in the effective hydrogen-side boundary state. The associated concentrations are

$$c_{i,L} = \frac{n_{i,L}}{V_L}, \qquad c_{i,R}^{\mathrm{eff}} = \frac{n_{i,R}}{V_{R,\mathrm{eff}}}, \qquad i \in \{2,3\}. \tag{3.32}$$

With $I > 0$ defined as charge, membrane transport and Faradaic conversion give

$$\frac{dn_{2,L}}{dt} = -AN_2 - \frac{I(t)}{F}, \tag{3.33}$$

$$\frac{dn_{3,L}}{dt} = -AN_3 + \frac{I(t)}{F}, \tag{3.34}$$

$$\frac{dn_{2,R}}{dt} = AN_2, \tag{3.35}$$

$$\frac{dn_{3,R}}{dt} = AN_3. \tag{3.36}$$

The measured stack current history is imposed directly as the electrical forcing. Duplicate or non-monotonic timestamps are removed, and downsampling is performed while retaining current and step-type transitions. Current reversal is therefore determined by the measured operating profile rather than by prescribed SoC thresholds.

Between OCV checkpoints, the left-tank state of charge is calculated as

$$\mathrm{SoC}(t) = \frac{n_{3,L}}{n_{2,L} + n_{3,L}}. \tag{3.37}$$

At each accepted rest-to-cycling transition, the measured OCV is converted to an SoC estimate using

$$\mathrm{SoC}_{\mathrm{OCV}} = \frac{1}{1 + \exp\left[-\left(V_{\mathrm{OC}} - E^{\circ\prime}\right)/b\right]}, \tag{3.38}$$

where $E^{\circ\prime}$ and b are obtained from the OCV–SoC calibration. The Fe^{2+}/Fe^{3+} split is then re-anchored to the OCV-derived SoC while preserving the total left-tank iron inventory,

$$n_{2,L} + n_{3,L}. \tag{3.39}$$

The effective hydrogen-side inventories and the resistance-growth state are not modified during this assimilation step. The calculation is therefore an OCV-assimilated, data-assisted simulation rather than an autonomous prediction of the complete electrochemical trajectory.

Between OCV corrections, the model satisfies the global iron-inventory balance

$$n_{2,L} + n_{3,L} + n_{2,R} + n_{3,R} = \mathrm{constant}. \tag{3.40}$$

The complete dynamic state vector is

$$\mathbf{y}(t) = \left[n_{2,L},\, n_{3,L},\, n_{2,R},\, n_{3,R},\, \theta\right]^{\mathsf{T}}. \tag{3.41}$$

3.9.5. Effective Resistance-Growth State

The measured resistance trajectories exhibit monotonic, progressively decelerating growth and can be represented using a saturating exponential. Such curvature is compatible with a finite-capacity membrane-associated process, including iron-related modification of ion-exchange environments, but it is not unique to one microscopic mechanism. Multivalent-cation exchange has been shown to alter proton mobility and reduce the conductivity of PFSA membranes [16], [21], [52].

The model therefore introduces a dimensionless effective resistance-growth state,

$$0 \le \theta \le 1, \tag{3.42}$$

which represents the normalised progression of the apparent resistance response. The state is not identified directly with a measured fraction of sulfonate sites occupied by iron or with a specific number of retained iron ions.

The nominal stack formulation uses the effective hydrogen-side total mobile-iron concentration as the exposure proxy:

$$C_{\mathrm{Fe},R}^{\mathrm{eff}} = c_{2,R}^{\mathrm{eff}} + c_{3,R}^{\mathrm{eff}} = \frac{n_{2,R} + n_{3,R}}{V_{R,\mathrm{eff}}}. \tag{3.43}$$

The variables $C_{\mathrm{Fe},R}^{\mathrm{eff}}$ and θ therefore have distinct roles. The former is a concentration-based exposure variable, whereas the latter is a dimensionless state defined by the normalised resistance response. No conversion of resistance into iron concentration is performed, and θ is not equated to molecular site coverage. The modelling hypothesis is instead that the local iron concentration controls the rate at which the effective resistance-growth state evolves. The resistance-growth state is represented by the finite-capacity relationship

$$\frac{d\theta}{dt} = k_{\mathrm{block}} C_{\mathrm{Fe},R}^{\mathrm{eff}} \left(1 - \theta\right). \tag{3.44}$$

The factor $1 - \theta$ represents the remaining capacity for additional resistance growth relative to the fitted asymptote. It should not necessarily be interpreted as the physical fraction of vacant sulfonate sites. Equation (3.44) is mathematically analogous to the adsorption-only limiting form of Langmuir-type accumulation models, which have been used to represent concentration-dependent, finite-capacity membrane-fouling behaviour [53]. This analogy motivates the saturating functional form but does not imply that θ is a molecular adsorption coverage or that Fe–sulfonate binding is the unique cause of the measured response.

Here k_{block} is an effective, concentration-normalised resistance-growth coefficient with units

$$[k_{\mathrm{block}}] = \mathrm{m}^3\,\mathrm{mol}^{-1}\,\mathrm{s}^{-1}. \tag{3.45}$$

It is obtained from the Membrane X H-cell resistance trajectory by normalising the fitted pseudo-first-order coefficient against the extended-ideal estimate of the membrane-phase iron concentration under the symmetric 50%-SoC H-cell condition. Applying the same coefficient to $C_{\mathrm{Fe},R}^{\mathrm{eff}}$ in the stack is therefore a conditional transfer between reduced concentration descriptions. It is not the use of a universal microscopic adsorption constant, equilibrium affinity, or Fe–sulfonate bond parameter.

The apparent cell resistance is mapped as

$$R(t) = R_0 + \Delta R_{\max}\theta(t), \tag{3.46}$$

where R_0 and $\Delta R_{\max}$ are obtained from the measured stack resistance trajectory. The model therefore does not independently predict the absolute resistance baseline or amplitude. The corresponding experimental resistance-growth state is

$$\theta_{\mathrm{exp}}(t) = \frac{R_{\mathrm{exp}}(t) - R_0}{\Delta R_{\max}}, \tag{3.47}$$

which is compared with

$$\theta_{\mathrm{model}}(t) = \theta(t). \tag{3.48}$$

The independent element of this comparison is the temporal evolution generated by the H-cell-derived effective coefficient and the calculated stack iron-exposure history.

No separate bound-iron inventory is resolved in the nominal model. This does not imply that iron association, retention, or ion exchange is absent physically. Instead, θ represents the cumulative net resistance response to the calculated iron-exposure history, while the available measurements do not establish a unique conversion between resistance growth, occupied charge-equivalent capacity, and moles of retained Fe^{2+} or Fe^{3+}.

The use of

$$C_{\mathrm{Fe},R}^{\mathrm{eff}} = c_{2,R}^{\mathrm{eff}} + c_{3,R}^{\mathrm{eff}} \tag{3.49}$$

also assigns equal effective molar weighting to Fe^{2+} and Fe^{3+}. Possible species-specific differences in affinity, persistence, charge stoichiometry, and resistance impact are therefore absorbed into the single effective coefficient obtained under the mixed H-cell condition.

3.9.6. Model Scope, Boundaries, and Assumptions

The model is developed as a reduced-order, data-assisted framework to test whether the calculated hydrogen-side mobile-iron exposure, together with the H-cell-derived resistance-growth parameter, can reproduce the normalised stack-resistance trajectory under the investigated operating conditions. It is not intended to represent the complete multiphase stack, to resolve the molecular mechanism of iron–membrane interactions, or to provide an independent prediction of absolute cell resistance.

The spatial model domain consists of zero-dimensional well-mixed bulk inventories, a one-dimensional membrane domain extending over $0 \leq x \leq \delta$, and a zero-dimensional effective hydrogen-side hydrated-capacitance state. The temporal focus is the long-duration evolution of iron transport and apparent resistance. Rapid membrane-storage, start-up, and switching transients lie outside the intended model scope.

The assumptions and closure relations that define this model domain are summarised below.

1. **Hybrid reduced-order architecture.** Bulk inventories, the effective hydrogen-side boundary state, and resistance growth are zero-dimensional; Fe^{2+}/Fe^{3+} membrane transport is solved quasi-steadily in one dimension.
2. **Quasi-steady non-equilibrium transport.** The membrane profile relaxes in approximately 2.35–$2.80\,\mathrm{s}$. Transient membrane storage is omitted, but nonuniform concentrations and nonzero fluxes are retained.
3. **Homogeneous effective membrane properties.** D_i, κ_{eff}, water content, and fixed-charge concentration are spatially uniform effective properties. Ionic concentrations may vary with x.
4. **Extended-ideal aqueous-side Donnan partitioning.** H^+, Fe^{2+}, Fe^{3+}, HSO_4^-, and SO_4^{2-} are included in the interfacial electroneutrality calculation. Activities are approximated by concentrations and iron–sulfate complexes are not resolved explicitly.
5. **Effective hydrogen-side boundary closure.** No gas-phase Donnan equilibrium is imposed. The right boundary is coupled to an effective hydrated-capacitance state. Its characteristic volume is estimated from water uptake.
6. **Effective Ohmic field closure.** The electric field is calculated from measured current density and a fixed effective membrane ionic conductivity. Supporting-ion profiles and a full multi-ion potential equation are not solved.
7. **Negligible membrane convection.** Pressure-driven and electro-osmotic convection are neglected relative to diffusion and electromigration as a first-order approximation.
8. **Langmuir-inspired net resistance growth.** The monotonic saturating state is treated as effectively irreversible over the measured interval. Desorption is not resolved, and the adopted form is not regarded as a unique microscopic mechanism.
9. **One-way transport–resistance coupling.** The resistance-growth state does not update D_i, κ_{eff}, water uptake, fixed charge, or the Donnan coefficients.
10. **Data-assisted operating trajectory.** The measured current history is imposed and the Fe^{2+}/Fe^{3+} split is periodically assimilated from OCV. R_0 and $\Delta R_{\max}$ are stack-derived, so the comparison concerns normalised trajectory shape rather than a blind prediction of absolute resistance.
11. **Omitted cell-level processes.** Detailed GDE hydration and purge dynamics, electrode degradation, contact-resistance evolution, side reactions, and spatial current nonuniformity are not resolved. Their possible contributions limit unique attribution of the apparent cell-resistance increase to membrane iron retention.

All numerical values used in the model are compiled in Appendix B.

4

Membrane Performance, Retained Iron, Resistance Evolution, and Model-Experiment Comparison

This chapter presents the experimental and computational results obtained across three interconnected lines of investigation. Section 4.1 reports the stack-cycling behaviour and apparent BOC resistance evolution for NR212, Membrane X, and CMVN, comparing their fitted resistance-growth trajectories. Section 4.2 presents post-cycling SEM–EDS elemental analysis of NR212 and Membrane X, examining where iron signals localise and the interpretive limits of the technique. Section 4.3 reports the ex-situ immersion results, comparing Fe^{2+}- and Fe^{3+}-rich retained-iron uptake across all three membranes on both molar and charge-equivalent bases. Section 4.4 presents the H-cell resistance-growth trajectory for Membrane X and derives the concentration-normalised coefficient k_{block}. Finally, Section 4.5 presents the data-assisted model results, comparing the simulated Membrane X resistance trajectory against the measured stack data and testing its sensitivity to the assumed membrane ionic conductivity. Together, these results form the experimental and theoretical basis for the discussion in Chapter 5.

4.1. Stack-Cycling Behaviour and Apparent Beginning-of-Charge Resistance

This section presents the stack-cycling behaviour of Nafion NR212, Selemion CMVN, and Membrane X. For NR212 and Membrane X, an apparent beginning-of-charge (BOC) cell-resistance indicator was calculated from the voltage response measured $10\,\mathrm{s}$ after the transition from rest to charge, as described in Section 3.2.6. Because this quantity is derived from the complete cell voltage response, it cannot be interpreted as a uniquely membrane-specific or purely ohmic resistance. CMVN did not produce a sufficiently stable cycling sequence for a reliable BOC resistance time series; its current–voltage behaviour is therefore reported separately.

4.1.1. Membrane X

Figure 4.1 shows the BOC resistance of Membrane X over 477 h of stack cycling, nominally at a constant power of 55 W. The first approximately $80\,\mathrm{h}$ of the Membrane X test were conducted under an unintended mix of $35\,\mathrm{W}$ and $55\,\mathrm{W}$ constant-power setpoint, rather than the $55\,\mathrm{W}$ setpoint specified for the principal company testing protocol. Once the protocol deviation was identified, the setpoint was corrected to $55\,\mathrm{W}$. Because the initial period with $35\,\mathrm{W}$ represents a different operating regime, relevant data from $t < 80\,\mathrm{h}$ are excluded from the resistance measurement. The complete measured operating history, including the initial $35\,\mathrm{W}$ period, is provided in Appendix H for transparency.

The resistance increased from 0.552 mΩ at $t = 80$ h to approximately 0.567 mΩ at $t \approx 150$ h, and

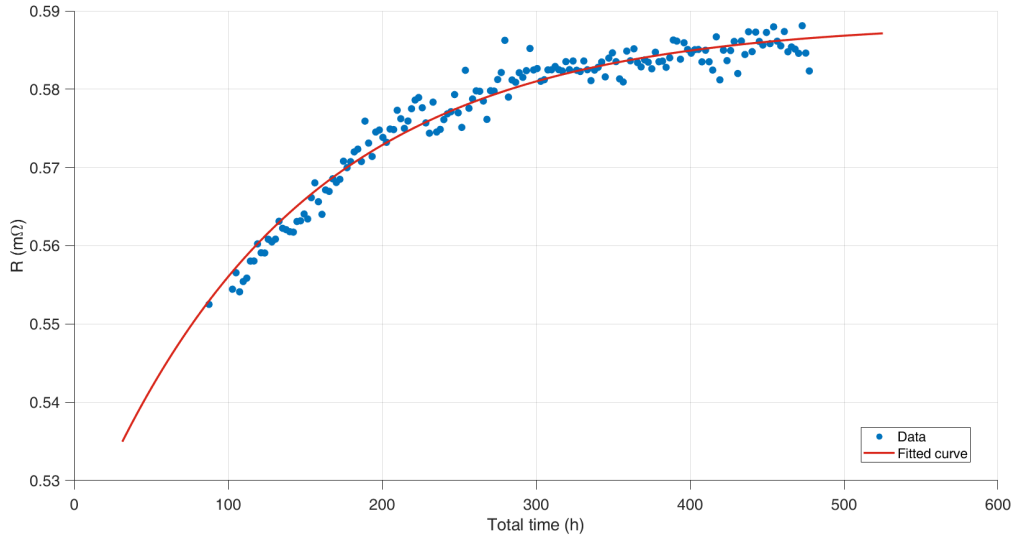


Figure 4.1: Beginning-of-charge (BOC) resistance of Membrane X during stack cycling as a function of total cycling time. The solid line shows the fitted saturating exponential (Equation 3.6).

continued to increase, at a progressively slower rate, up to approximately 0.582–0.583 mΩ by $t \approx 300$ h. Beyond $t \approx 300$ h, the resistance remained within a narrow band of approximately 0.582–0.588 mΩ for the remainder of the test, with no further systematic increase discernible up to the final measurement at $t = 477$ h. Overall, the BOC resistance increased by approximately 8% relative to its initial value over the full cycling window. To describe the observed curvature, the apparent BOC resistance data were fitted to the saturating exponential given in Equation 3.6. The fit yielded a $t = 0$ intercept of $R_0 = 0.524\,\mathrm{m\Omega}$, a fitted asymptotic resistance increment of $\Delta R_{\max} = 0.064\,\mathrm{m\Omega}$, and $k_{\mathrm{obs}} = 7.63 \times 10^{-3}\ \mathrm{h}^{-1}$. The corresponding fitted asymptote was $R_{\mathrm{sat}} = 0.588\,\mathrm{m\Omega}$ ($R^2 = 0.965$). Because the first reported measurement occurred at $t = 26$ h, R_0 represents the fitted intercept rather than a directly measured initial value. The fitted time to reach 99% of the asymptotic increment was $t_{99} = 603\,\mathrm{h}$. At $t = 477\,\mathrm{h}$, the final measured resistance corresponded to approximately 90.9% of the fitted increment. The value of t_{99} is therefore an extrapolated fit metric rather than a directly observed saturation time.

4.1.2. Nafion NR212

Figure 4.2 shows the BOC resistance of NR212 over approximately 965 h of stack cycling at a constant power of 45W, after a few initial cycles at 35 W which were excluded from the plot due to reasons similar to Membrane X. The resistance remained approximately constant at 1.048–1.050 mΩ between $t \approx 55$ h and $t \approx 95$ h, after which it began to increase steadily. By $t \approx 200$ h the resistance had reached approximately 1.11 mΩ, increasing further to approximately 1.20 mΩ at $t \approx 400$ h, 1.27 mΩ at $t \approx 600$ h, and 1.31 mΩ at $t \approx 800$ h. The resistance continued to increase up to the final measurement, reaching approximately 1.349 mΩ at $t \approx 965$ h. Overall, the BOC resistance increased by approximately 35% relative to its initial value over the full cycling window.

The same empirical fitting procedure was applied to the NR212 apparent BOC resistance data. The fit yielded a $t = 0$ intercept of $R_0 = 0.995\,\mathrm{m\Omega}$, a fitted asymptotic increment of $\Delta R_{\max} = 0.494\,\mathrm{m\Omega}$, and $k_{\mathrm{obs}} = 1.31 \times 10^{-3}\ \mathrm{h}^{-1}$, corresponding to a fitted asymptote of $R_{\mathrm{sat}} = 1.489\,\mathrm{m\Omega}$ ($R^2 = 0.997$). As the first reported resistance measurement was approximately $1.048\ \mathrm{m\Omega}$ at $t \approx 55\ \mathrm{h}$, the fitted R_0 is an extrapolated intercept rather than a directly measured initial value. The final measured resistance corresponded to approximately 71.7% of the fitted asymptotic increment. The resulting $t_{99} \approx 3.52 \times 10^3\ \mathrm{h}$ is therefore a substantial extrapolation beyond the $965\ \mathrm{h}$ observation window and should be interpreted as a descriptive fit parameter rather than an observed membrane lifetime or saturation time.

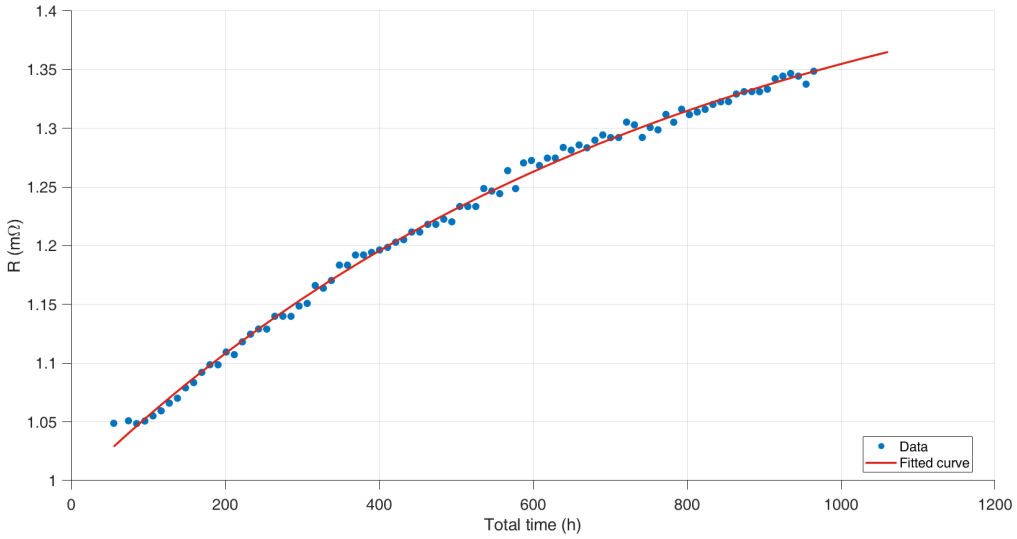


Figure 4.2: Beginning-of-charge (BOC) resistance of Nafion NR212 during stack cycling as a function of total cycling time. The solid line shows the fitted saturating exponential (Equation 3.6).

4.1.3. Selemion CMVN

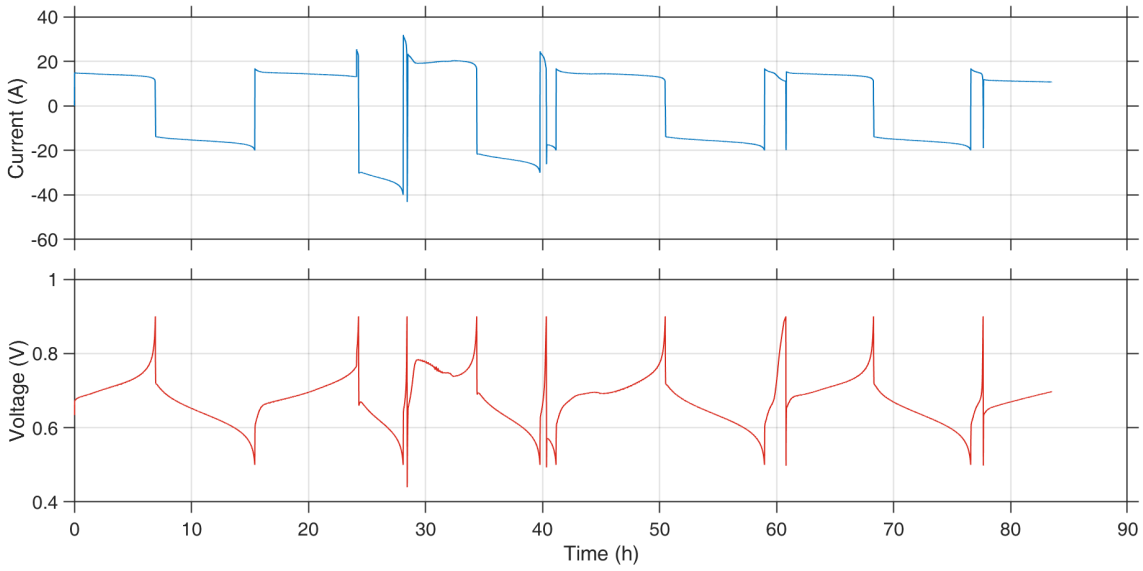


Figure 4.3: Current and voltage response of the CMVN stack during the stepped-power cycling protocol. The stack completed several full charge–discharge cycles, but repeated abrupt cutoff-limited transitions occurred between cycles, and stable uninterrupted multi-cycle operation was not maintained.

Figure 4.3 shows the current and voltage response of the stack assembled with CMVN over approximately $84\,\mathrm{h}$. Positive current corresponds to charge and negative current to discharge. The stack initially completed a full cycle at a constant power of $10\,\mathrm{W}$, with the voltage increasing from approximately 0.67 to the $0.90\,\mathrm{V}$ upper cutoff during charge and decreasing toward the lower cutoff during discharge.

At the same power, a second charge segment was completed between approximately 16 and $24\,\mathrm{h}$. During the subsequent higher-power discharge, the current magnitude increased from approximately 30 to $44\,\mathrm{A}$ as the voltage decreased from approximately 0.66 to $0.45\,\mathrm{V}$, consistent with constant-power control. At the following discharge transition near $28\,\mathrm{h}$, however, the voltage reached the upper cutoff

abruptly and the transition did not develop into a sustained discharge segment.

Following adjustment of the applied power to $20\,\mathrm{W}$, the stack completed another charge–discharge cycle between approximately 29 and $40\,\mathrm{h}$. Returning to $10\,\mathrm{W}$ subsequently enabled two further full cycles, approximately between 41–$59\,\mathrm{h}$ and 61–$77\,\mathrm{h}$. These cycles were separated or followed by short transitions in which the upper voltage cutoff was reached abruptly. A final partial charge segment was recorded after approximately $78\,\mathrm{h}$, but no further complete cycle was obtained before the end of the recorded test.

The tested CMVN stack configuration therefore demonstrated that individual charge–discharge cycles could be completed, including after power adjustments or system intervention, but continuous repeatable cycling was not maintained throughout the stepped-power protocol. The interrupted transitions prevented extraction of a consistent beginning-of-charge resistance time series and the testing had to be stopped due to poor performance, especially compared to Membrane X and NR212 which were able to cycle at much higher powers of $55\,\mathrm{W}$ and $45\,\mathrm{W}$ respectively.

The recovery of broadly similar cycling profiles following intervention means that the figure does not, by itself, establish a monotonic increase in resistance or irreversible degradation of the CMVN membrane. The observed instability could have originated from the membrane, membrane hydration, stack contacts, the electrode or gas-diffusion electrode, reactant management, or the test-control system. The available current–voltage data are therefore used to establish operational instability of the tested configuration, rather than to assign a unique component-level failure mechanism.

4.1.4. Discussion: Comparative Stack-Cycling Behaviour

Both Membrane X and NR212 exhibited increasing apparent BOC cell resistance over their respective stack tests. Membrane X showed an observed increase of approximately 8% over $477\ \mathrm{h}$, followed by a narrow late-time resistance range, whereas NR212 showed an observed increase of approximately 35% over $965\ \mathrm{h}$ and had not reached a clear plateau by the end of the test. Both trajectories were represented empirically by saturating exponentials, although the fitted asymptote and t_{99} for NR212 require substantial extrapolation beyond the measured window.

The saturating curvature is compatible with a finite-capacity degradation or occupation process, including iron-related membrane changes, but does not uniquely identify the responsible mechanism. The apparent BOC resistance is obtained from the complete cell response and may include contributions from the membrane, electrolyte, contacts, electrodes, GDE, and other interfaces.

Under the respective configurations tested, Membrane X exhibited both the lower absolute apparent cell resistance and the smaller relative resistance increase. This is a favourable candidate-level result. However, the NR212 and Membrane X tests differed in electrolyte volume, power setpoint, stack configuration, and cycling duration. Their absolute fitted resistances and rate constants should therefore not be interpreted as intrinsic like-for-like membrane properties. Comparison using normalised resistance, completed equivalent cycles, cumulative charge throughput, and matched stack hardware would provide a stronger material-level ranking.

CMVN did not sustain a stable sequence of charge–discharge cycles under the applied stepped-power protocol, and no reliable BOC resistance trajectory was obtained. The result demonstrates instability of the tested CMVN stack configuration, but the available current–voltage data do not isolate the cause or establish that a monotonic resistance increase was responsible.

4.2. Post-Cycling SEM-EDS Analysis of Membranes

Scanning electron microscopy with energy-dispersive X-ray spectroscopy (SEM–EDS) was used to examine the surface morphology of pristine and cycled membrane samples and to determine the elemental composition at selected surface locations. The method provides local elemental information within the electron-beam interaction volume but does not determine iron oxidation state, chemical coordination, or through-thickness distribution. Both membranes proved difficult to image reliably owing to their thin, non-conductive, beam-sensitive nature; the resulting limitations are addressed in detail.

4.2.1. Nafion NR212

To distinguish iron accumulation from intrinsic membrane features, a pristine NR212 sample was imaged as a reference alongside the cycled sample. The pristine surface (Figure 4.4) exhibits the characteristic anisotropic “tiger-stripe” ridge texture arising from manufacturing, with occasional isolated surface particulates.

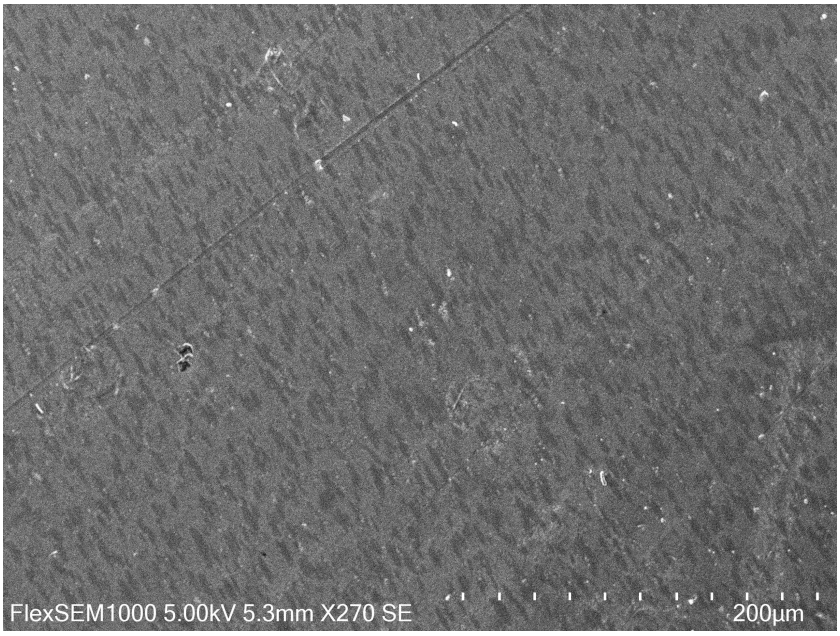
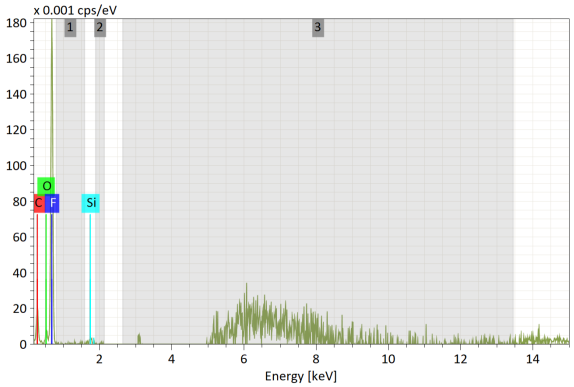


Figure 4.4: Secondary-electron image of pristine (uncycled) NR212, showing the characteristic anisotropic ridge (“tiger-stripe”) surface texture used as the morphological reference

EDS of the pristine surface (Figure 4.5) was acquired at two points: Spectrum 1, on an isolated bright particulate, and Spectrum 2, on the nominally featureless off-particle surface location. Spectrum 2 returned only the expected PFSA backbone constituents (C, O, F) with a trace Si signal, and no detectable iron (Table 4.1). Spectrum 1 identified the particulate as an Al/S/Cl-bearing contaminant, unrelated to iron fouling (Figure H.3).



(a) SEM context

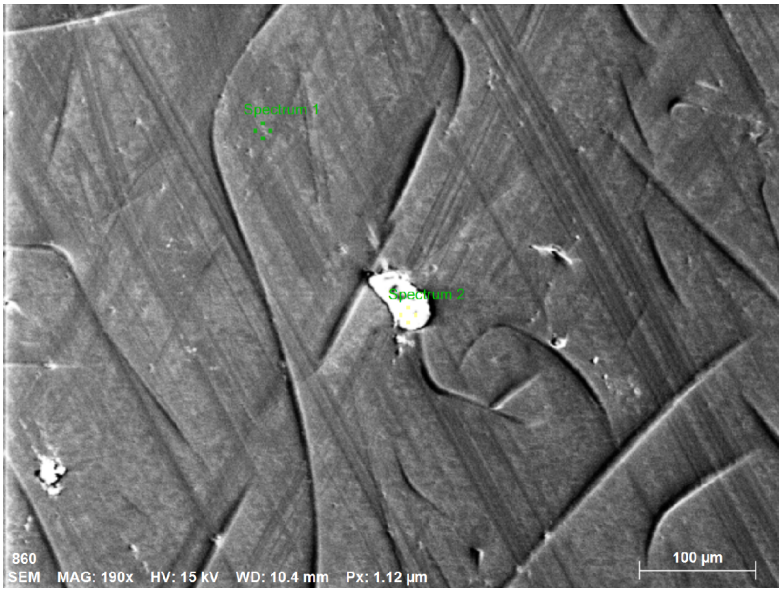


(b) Spectrum 2 (matrix)

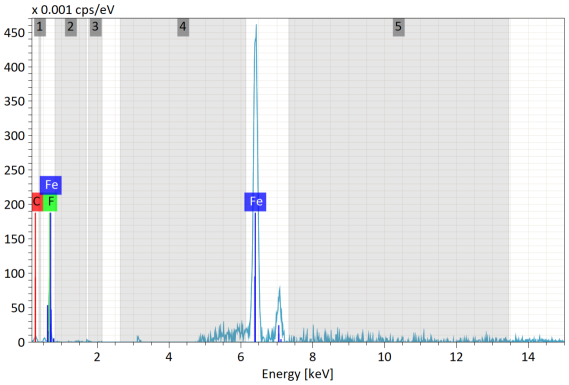
Figure 4.5: EDS analysis of pristine NR212 (15 kV, 600×). Spectrum 2, acquired on the plain membrane matrix, shows only C, O, F, and trace Si; no iron is detected. The Spectrum 1 particulate is reported in Figure H.3.

The cycled NR212 surface retained the underlying ridge texture but additionally exhibited discrete surface particulates. EDS was acquired across two independent fields of view (Figures 4.6 and 4.7). In both fields, matrix points acquired at nominally featureless locations consistently returned a very high

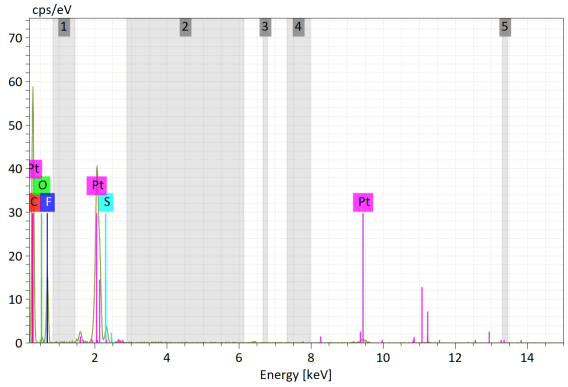
iron signal, with Fe constituting 49–86 at% of the detected elements (Table 4.1), while the visible bright particulates were instead identified as platinum, most likely transferred from the catalyst layer during cell disassembly.



(a) SEM context



(b) Spectrum 1 (matrix)



(c) Spectrum 2 (particle)

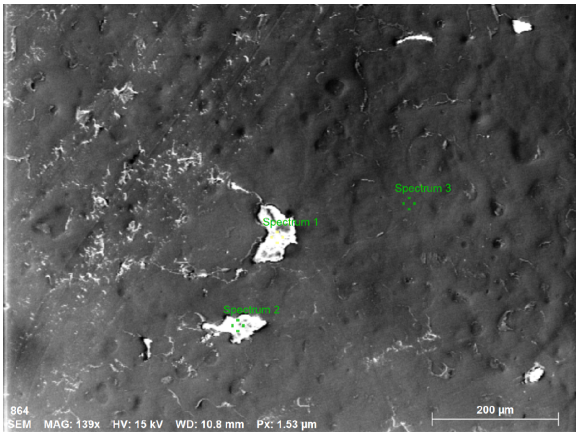
Figure 4.6: EDS analysis of cycled NR212, Field 1 (15 kV, 190×). Spectrum 1, acquired on the plain matrix, is iron-dominated (86.09 at%, 95.53 mass norm.%). Spectrum 2, acquired on the bright particulate visible in the SEM context image, having substantial Pt contribution (2.24 at%, 25.66 mass norm.%), identifying this feature as catalyst-derived contamination rather than an iron deposit.

The contrast between the pristine and cycled matrix compositions is summarised in Table 4.1.

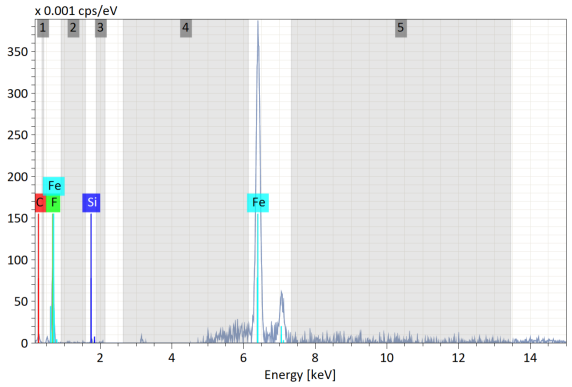
Table 4.1: Comparison of representative EDS matrix (off-particle) point spectra for pristine and cycled NR212. Values are atomic percent (at.%), normalized basis. Dashes indicate elements not detected.

Sample / location	C	O	F	Si	Fe
Pristine, matrix (Spectrum 2)	30.92	4.20	64.36	0.52	—
Cycled, Field 1, matrix (Spectrum 1)	5.66	—	8.25	—	86.09
Cycled, Field 2, matrix (Spectrum 2)	6.36	7.79	—	36.01	49.85

At one nominally featureless off-particle surface location in each of two spatially separated fields, software-normalised EDS analysis returned strong Fe signals of 86.09 and 49.85 at.%. No Fe was detected at the analysed pristine NR212 off-particle location. The visible particulates sampled on the



(a) SEM context



(b) Spectrum 3 (matrix)

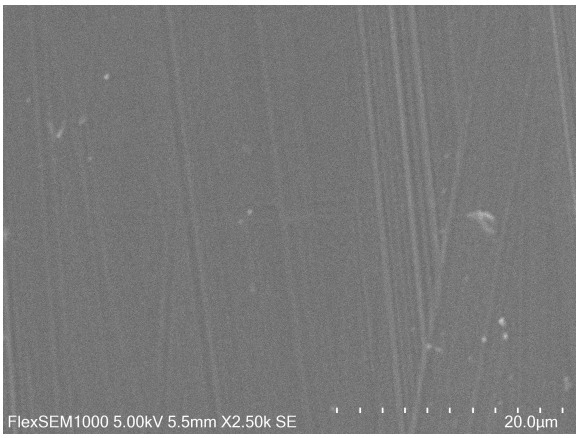
Figure 4.7: EDS analysis of cycled NR212, Field 2 (15 kV, 139×). Spectrum 3, acquired on the plain matrix, is again iron-dominated (49.85 at%, 69.26 mass norm.%), reproducing a strong Fe signal at a second spatially separated off-particle location. (Figure 4.6). Spectra 1 and 2, acquired on the bright particulates visible in the SEM context image, identified further Pt/S-bearing contamination and are reported in Figure H.4 and Figure H.5 .

cycled membrane were Pt- or Pt/S-bearing rather than clearly Fe-rich, showing that image brightness alone did not identify the locations of the strongest Fe signal.

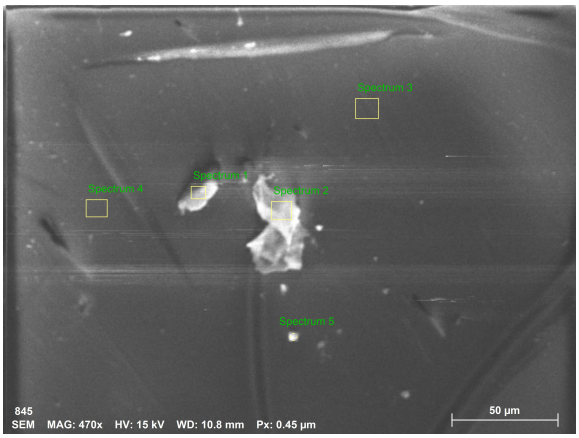
4.2.2. Membrane X

Acquiring stable images proved more difficult throughout compared to NR212, so incident electrons accumulated on the surface, producing lateral image drift and scan-line streaking at higher accelerating voltage. Re-imaging the same region after a short interval sometimes showed a visibly altered surface: particulate features changed apparent size and in some cases disappeared entirely between successive acquisitions. Reducing the accelerating voltage improved stability but did not fully eliminate the effect.

A pristine (uncycled) reference sample was imaged: the non-conductive surface with parallel ridges, possibly from the manufacturing process are visible as shown in Figure 4.8.



(a) Pristine (uncycled)

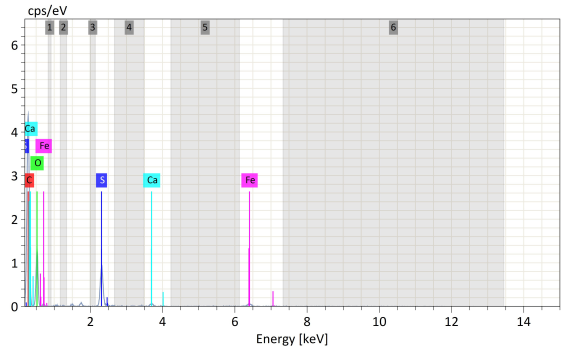


(b) Cycled (fouled); Spectra 2 and 3 in Figure 4.9 were acquired within this field of view

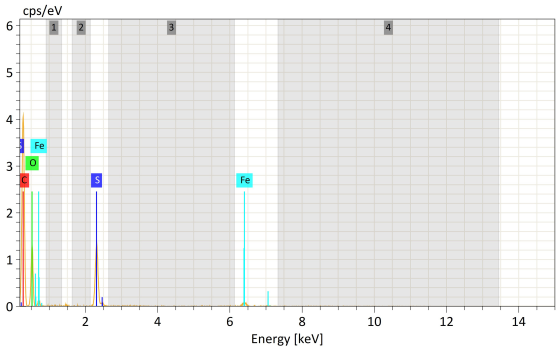
Figure 4.8: Comparison of pristine and cycled Membrane X surfaces (5 kV). The pristine surface (a) shows ridges with no resolvable morphological feature, precluding a pristine SEM-EDS baseline for this membrane. The cycled surface (b) is comparatively stable and resolves discrete surface features.

Figures 4.9 and 4.10 show representative off-particle matrix spectra from two independent fields of view, and Figure 4.11 shows the highest-iron on-particle spectrum obtained in this dataset; Table H.2 summarises the corresponding iron readings across all seventeen points acquired over three independent

fields of view.

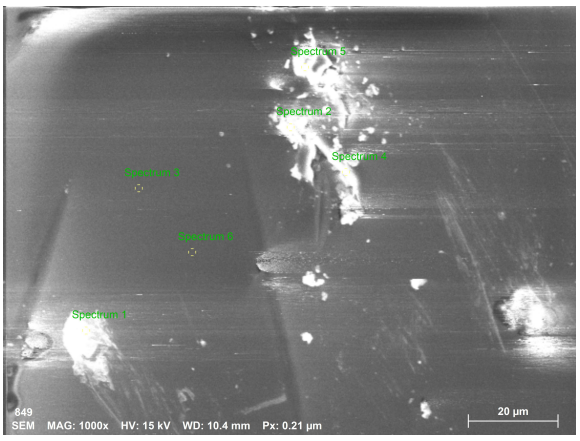


(a) Spectrum 2 (matrix)

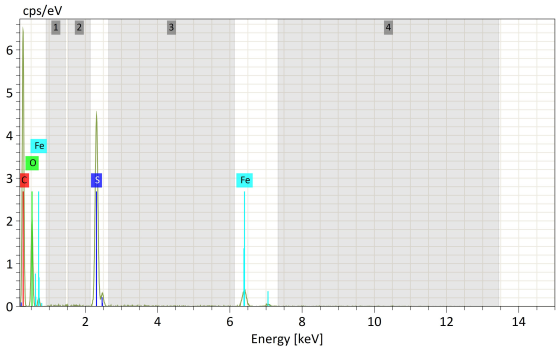


(b) Spectrum 3 (matrix)

Figure 4.9: Representative off-particle (matrix) EDS point spectra for Membrane X, Field 1 (15 kV, 470×); SEM context for both points is shown in Figure 4.8b. Spectrum 2 (Fe 0.52 at.%, Fe 2.12 mass norm.%) additionally shows a minor Ca signal; Spectrum 3 (Fe 0.68 at.%, 2.77 mass norm.%) is dominated by C, O, and S. The remaining EDS Spectra 1, 4 and 5 are reported in Figure H.7



(a) SEM context (Spectrum 2: matrix)



(b) Corresponding EDS spectrum

Figure 4.10: Representative off-particle (matrix) EDS point spectrum for Membrane X, Field 2, Spectrum 2 (15 kV). This independent field of view again shows a C/O/S-dominated matrix with a modest Fe signal (1.98 at.%, 7.59 mass norm.%), the highest matrix reading recorded across all three fields. The remaining spectra 1,4, 5 and 6 are presented in Figure H.8 and H.9 .

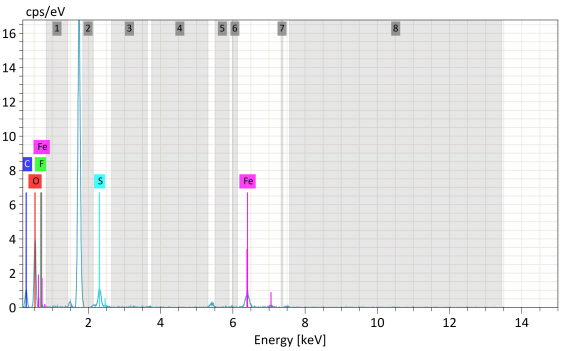
Even with the beam centred on a visibly bright particle, iron reached only 6.37 at% (19.4 mass% normalized), roughly an order of magnitude above the typical matrix reading (0.68 at%). However, the raw analytical total for this spectrum was only 45.95%, so its normalised value of $6.37\ \mathrm{at.\%}$ is reported for qualitative comparison only and should not be interpreted as a quantitative particle composition. Across all matrix (off-particle) points, iron consistently fell within a narrow low range of 0.24–1.98 at%, with no obvious field-to-field pattern was observed within the sampled locations. A consistent low-level iron signal was therefore detected across matrix regions containing no visible particulate, in every field examined. A separate, more strongly Si-contaminated point (Field 2, Spectrum 5; Si 18.81 at%, Fe 0.95 at%) was also identified and is attributed to an unrelated surface contaminant rather than an iron-bearing deposit (Figure 4.10 b). The remaining EDS point spectra acquired across all three fields, not shown individually above, are reported in full in Appendix H.

4.2.3. Discussion: Iron Occurrence and Interpretive Limits of SEM-EDS

A stoichiometric consistency check was used to evaluate whether the large software-normalised Fe fractions obtained for cycled NR212 could represent homogeneous ion-exchange loading. For Nafion with a nominal equivalent weight of approximately $1100\ \mathrm{g\,mol^{-1}}$, complete exchange with Fe^{2+} would correspond to approximately $0.8\ \mathrm{at.\%}$ Fe on a non-hydrogen atomic basis, while complete exchange



(a) SEM context (Spectrum 1: particle)



(b) Corresponding EDS spectrum

Figure 4.11: Highest-iron on-particle EDS point spectrum for Membrane X, Field 3, Spectrum 1 (15 kV, 650×). Despite the on-particle placement, the Fe signal (6.37 at.%, 19.40 mass norm.%) remains modest, and the raw measured mass fractions sum to only 45.95% of the expected total, indicative of degraded X-ray collection from a small, charging-affected feature.

Table 4.2: Comparison of a representative off-particle EDS spectrum and the highest software-reported on-particle Fe spectrum for Membrane X. The raw analytical total of the on-particle spectrum was 45.95%; software-normalised values are included for qualitative reference only.

Spectrum	Fe (mass%, raw)	Fe (mass%, normalized)	Fe (at%)
Matrix (off-particle)	2.77	2.77	0.68
On-particle (highest Fe)	8.92	19.40	6.37

with Fe^{3+} would correspond to approximately $0.5\ \mathrm{at.\%}$. The reported values of 49–$86\ \mathrm{at.\%}$ therefore cannot be interpreted as the homogeneous composition of ion-exchanged NR212. Locally Fe-rich or otherwise more conductive regions may also charge less than the surrounding polymer and can therefore be preferentially resolved under the electron beam. Apparent image stability or brightness is not, however, treated as a quantitative indicator of Fe abundance.

The measurements demonstrate that strong Fe-related signals were present within the EDS interaction volume at selected cycled NR212 locations. However, they do not distinguish among an adherent Fe-rich surface phase, a locally concentrated subsurface region, and quantitative artefacts associated with charging, specimen geometry, contamination, or standardless normalisation. In particular, the second high-Fe spectrum also contained $36.01\ \mathrm{at.\%}$ Si and was therefore compositionally anomalous. The washing and sonication procedure reduces the likelihood that the signals originated solely from loosely retained electrolyte, but does not exclude a strongly adherent film or precipitated phase. Cross-sectional elemental mapping and bulk digestion would be required to establish the through-thickness distribution and total iron loading.

For Membrane X, software-reported Fe values of 0.24–$1.98\ \mathrm{at.\%}$ were obtained at sampled off-particle locations, while one visible feature produced a higher reported value of $6.37\ \mathrm{at.\%}$. A reliable pristine EDS baseline and sample-specific detection limit were not obtained, and the spectra with the highest reported Fe values had poor raw analytical totals. These values are therefore interpreted descriptively rather than as quantitative membrane or particle compositions.

Although the software-reported Fe fractions differed substantially between NR212 and Membrane X, the absolute values should not be used to rank total iron loading or fouling severity. The membranes differed in composition, charging behaviour, surface condition, and spectral quality, and their electron interaction volumes were not independently determined. The SEM–EDS results therefore provide qualitative evidence of Fe occurrence at selected cycled-sample locations but do not determine oxidation state, binding mechanism, through-thickness distribution, or comparative bulk iron loading.

4.3. Ex-Situ Iron Uptake in Membranes

The immersion experiments were used to compare the amount of iron retained by the three membranes following exposure to nominally Fe^{2+}-rich and Fe^{3+}-rich electrolytes. The samples were first subjected to the sequential water-washing procedure described in Section 3.4, after which the retained iron was released by NaCl exchange and quantified by UV–Vis spectrophotometry. The measured quantity is therefore the total water-wash-resistant, NaCl-exchangeable iron recovered from each membrane, normalised by the dry membrane mass. Throughout this section, the terms Fe^{2+}-rich and Fe^{3+}-rich refer to the nominal oxidation state of the corresponding exposure electrolyte. Because all dissolved Fe^{3+} was reduced before the UV–Vis measurement, the analytical method reports total extracted iron and does not independently determine the oxidation state of iron in the final extract. A separately immersed membrane sample was used at each time point. Consequently, the late-time trends are interpreted as apparent plateaus within the measured interval rather than as independently replicated thermodynamic equilibrium values. The results for NR212 are presented in Section 4.3.1, followed by those for CMVN in Section 4.3.2 and Membrane X in Section 4.3.3.

4.3.1. Iron Uptake in Nafion NR212

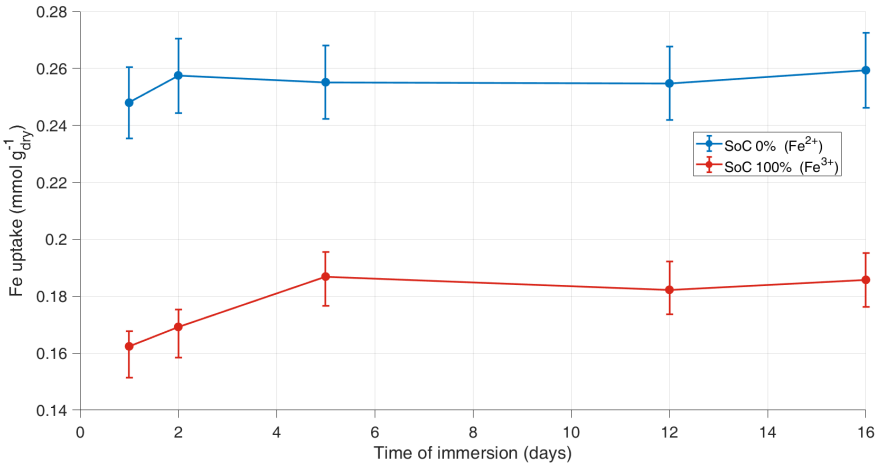


Figure 4.12: Iron uptake in Nafion NR212 as a function of immersion time under SoC $= 0$ (Fe^{2+}, blue) and SoC $= 100$ (Fe^{3+}, red) conditions. Each data point corresponds to an independently immersed membrane sample.

Figure 4.12 shows the retained-iron uptake in NR212 as a function of immersion time. Following exposure to the Fe^{2+}-rich electrolyte, the recovered iron increased from approximately $0.249\ \mathrm{mmol\,g^{-1}}$ at day 1 to $0.258\ \mathrm{mmol\,g^{-1}}$ at day 2. The subsequent values were 0.258, 0.255, and $0.259\ \mathrm{mmol\,g^{-1}}$ at days 5, 12, and 16, respectively. The small variation after day 2 is consistent with an apparent late-time plateau within the experimental resolution.

Following exposure to the Fe^{3+}-rich electrolyte, the retained iron increased more gradually, from $0.162\ \mathrm{mmol\,g^{-1}}$ at day 1 to $0.169\ \mathrm{mmol\,g^{-1}}$ at day 2 and $0.187\ \mathrm{mmol\,g^{-1}}$ at day 5. The values at days 12 and 16 were 0.182 and $0.186\ \mathrm{mmol\,g^{-1}}$, respectively. The Fe^{3+}-rich condition therefore approached its apparent plateau later than the Fe^{2+}-rich condition.

Using the day-16 values, the molar retained-iron ratio is

$$\mathcal{R}_{\mathrm{mol}}^{\mathrm{NR212}} = \frac{q_{\mathrm{Fe^{2+}\text{-rich}}}}{q_{\mathrm{Fe^{3+}\text{-rich}}}} = \frac{0.259}{0.186} = 1.39, \tag{4.1}$$

where q denotes the total extracted iron per gram of dry membrane. Although more moles of iron were recovered after Fe^{2+}-rich exposure, this comparison does not by itself demonstrate preferential occupation by Fe^{2+}, because Fe^{2+} and Fe^{3+} compensate different numbers of fixed-charge equivalents. This distinction is examined in Section 4.3.4.

4.3.2. Iron Uptake in Selemion CMVN

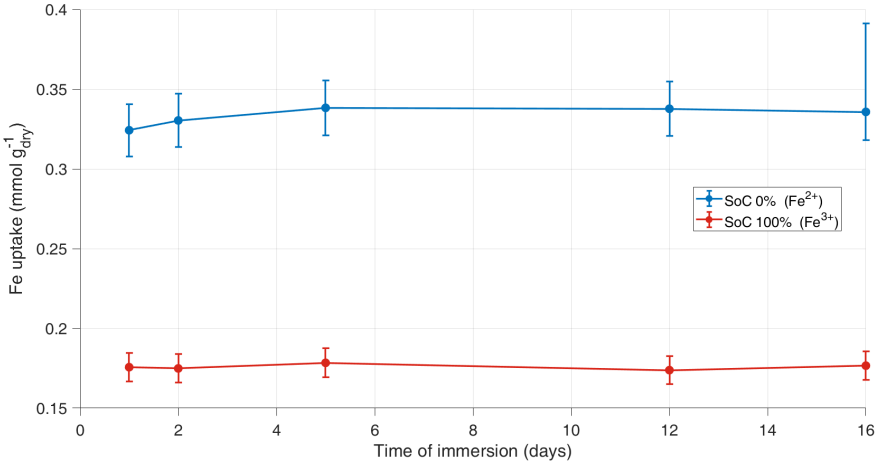


Figure 4.13: Iron uptake in Selemion CMVN as a function of immersion time under SoC $= 0$ (Fe^{2+}, blue) and SoC $= 100$ (Fe^{3+}, red) conditions. Each data point corresponds to an independently immersed membrane sample.

Figure 4.13 shows the corresponding retained-iron results for CMVN. Under Fe^{2+}-rich exposure, the recovered iron increased from approximately $0.324\ \mathrm{mmol\,g^{-1}}$ at day 1 to approximately $0.339\ \mathrm{mmol\,g^{-1}}$ by day 5, after which the values remained close to this level through day 16. The Fe^{2+}-rich condition therefore showed a modest increase over the first several days before reaching an apparent plateau.

Under Fe^{3+}-rich exposure, the retained iron was already approximately $0.178\ \mathrm{mmol\,g^{-1}}$ at day 1 and remained close to this value over the remainder of the test. Within the temporal resolution of the measurements, the Fe^{3+}-rich condition therefore reached its apparent plateau earlier than the Fe^{2+}-rich condition.

The corresponding late-time molar ratio is

$$\mathcal{R}_{\mathrm{mol}}^{\mathrm{CMVN}} = \frac{0.339}{0.178} = 1.90. \tag{4.2}$$

This is the largest molar ratio observed among the three membranes. However, as for NR212, the difference must be interpreted together with the charge stoichiometry of the two iron ions. On a charge-equivalent basis, CMVN retains more iron-associated charge following the Fe^{2+}-rich exposure, as discussed in Section 4.3.4.

4.3.3. Iron Uptake in Membrane X

Figure 4.14 shows the retained-iron uptake in Membrane X. Following Fe^{2+}-rich exposure, the recovered iron increased from $0.324\ \mathrm{mmol\,g^{-1}}$ at day 1 to $0.382\ \mathrm{mmol\,g^{-1}}$ at day 2. The subsequent values were 0.376, 0.374, and $0.372\ \mathrm{mmol\,g^{-1}}$ at days 5, 12, and 16, respectively.

Following Fe^{3+}-rich exposure, the retained iron increased from $0.268\ \mathrm{mmol\,g^{-1}}$ at day 1 to $0.307\ \mathrm{mmol\,g^{-1}}$ at day 2. The values at days 5, 12, and 16 were 0.314, 0.307, and $0.304\ \mathrm{mmol\,g^{-1}}$, respectively. For both exposure conditions, the change after day 2 was small compared with the initial increase, indicating that Membrane X had approached an apparent plateau within approximately two days.

The day-16 molar retained-iron ratio is

$$\mathcal{R}_{\mathrm{mol}}^{\mathrm{X}} = \frac{0.372}{0.304} = 1.22. \tag{4.3}$$

Membrane X exhibited the highest absolute late-time retained-iron uptake among the three membranes under both exposure conditions. Its molar ratio was nevertheless the closest to unity. When charge stoichiometry is taken into account, the Fe^{3+}-rich condition represents the larger retained fixed-charge-equivalent inventory.

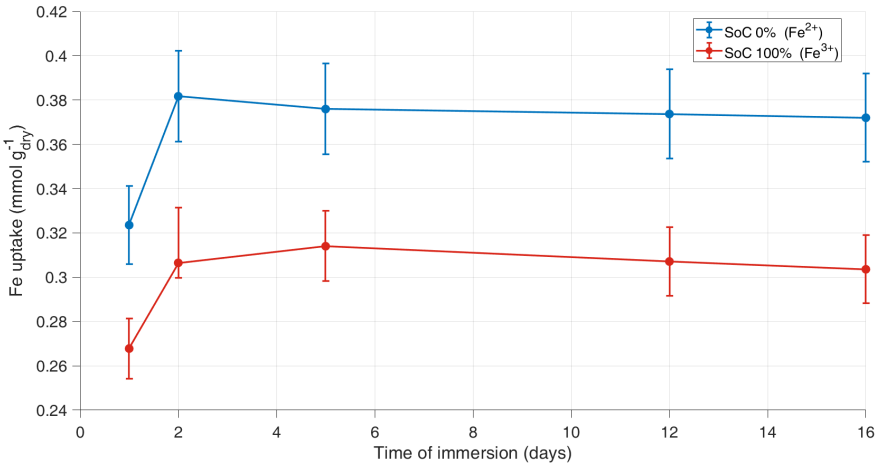


Figure 4.14: Iron uptake in Membrane X as a function of immersion time under SoC $= 0$ (Fe^{2+}, blue) and SoC $= 100$ (Fe^{3+}, red) conditions. Each data point corresponds to an independently immersed membrane sample.

4.3.4. Cross-Membrane Comparison of Retained-Iron Ratios

The late-time molar uptake following Fe^{2+}-rich exposure exceeded that following Fe^{3+}-rich exposure for all three membranes. However, a direct molar comparison does not account for charge stoichiometry: one Fe^{2+} ion compensates two fixed negative charges, whereas one Fe^{3+} ion compensates three. Equal occupation of membrane fixed-charge equivalents would therefore correspond to a molar ratio of $n_{Fe^{2+}}/n_{Fe^{3+}} = 1.5$. The measured results are compared on a charge-equivalent basis using

$$\mathcal{R}_{\mathrm{eq}} = \frac{2q_{Fe^{2+}\text{-rich}}}{3q_{Fe^{3+}\text{-rich}}} = \frac{\mathcal{R}_{\mathrm{mol}}}{1.5}. \tag{4.4}$$

Table 4.3: Measured mole and charge-equivalent uptake ratios (Fe^{2+}-rich vs.Fe^{3+}-rich) at day 16, compared with the ideal-Donnan-theory prediction

Membrane	$\mathcal{R}_{\mathrm{mol}}$	$\mathcal{R}_{\mathrm{eq}}$	$\mathcal{R}_D$
NR212	1.39	0.93	1.007
CMVN	1.90	1.27	1.057
Membrane X	1.22	0.82	1.012

NR212 was close to the equal-charge benchmark, while CMVN retained more iron-associated charge following Fe^{2+}-rich exposure and Membrane X retained more following Fe^{3+}-rich exposure. The direction of the difference was therefore membrane-specific, and the results do not indicate a universal preference for either exposure condition.

The ideal Donnan calculation predicted cross-endpoint partition ratios close to unity for all three membranes, indicating only weak electrostatic discrimination between the endpoint electrolyte conditions. These coefficients describe ideal mobile-ion partitioning into membrane water, whereas the experiment measures water-wash-resistant, NaCl-exchangeable total iron. The two ratios are therefore related but are not identical physical quantities.

The observed membrane-specific differences indicate that ideal electrostatic partitioning and charge stoichiometry alone do not fully describe the retained-iron results. Additional influences may include membrane-specific ion interactions, concentrated sulfate-electrolyte speciation, and experimental factors affecting iron oxidation state or extraction recovery.

4.4. Resistance Evolution in the H-Cell

Figure 4.15 shows the apparent high-frequency resistance of the Membrane X H-cell over approximately $264\ \mathrm{h}$. The resistance increased from $5.915\ \Omega$ at the first measurement to $6.086\ \Omega$ at $t = 263.4\ \mathrm{h}$, corresponding to an observed increase of approximately 2.9%.

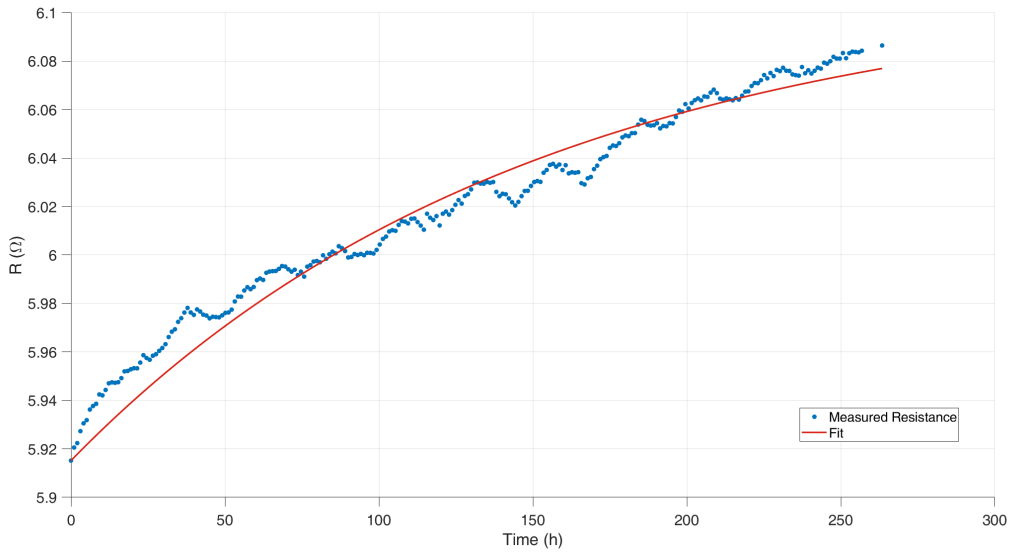


Figure 4.15: Evolution of the apparent high-frequency H-cell resistance during symmetric exposure of Membrane X to the 50% SoC iron electrolyte. Blue points denote the measured resistance and the red line denotes the nonlinear least-squares fit of Equation (4.5).

The measurement was performed in a two-electrode configuration and the time-dependent high-frequency resistance is treated as an apparent membrane-associated resistance-growth indicator. The symmetric geometry suppresses a sustained concentration gradient and stack-specific components, but the membrane contribution was not independently isolated through a blank subtraction. The reported resistance increase is probably driven by membrane fouling, although it can include contributions from the electrolyte, electrodes, and electrical contacts. However, the cell geometry, electrolyte composition, temperature, and electrode configuration were maintained throughout the experiment. The systematic time-dependent change is therefore used as an apparent membrane-associated resistance-growth indicator rather than as an independently isolated membrane resistance.

The measured trajectory was fitted using the saturating exponential

$$R(t) = R_0 + \Delta R_{\max}\left[1 - \exp(-k_{\mathrm{obs}} t)\right], \tag{4.5}$$

which has the same mathematical form as the finite-capacity blocking relationship used in the reduced-order model. The initial resistance was fixed at the first measured value, while R_{sat} and k_{obs} were obtained by nonlinear least-squares fitting. The fit yielded

$$R_{\mathrm{sat}} = 6.111\ \Omega, \qquad \Delta R_{\max} = 0.196\ \Omega,$$

and

$$k_{\mathrm{obs}} = 1.855 \times 10^{-6}\ \mathrm{s}^{-1} \quad \left(95\%\ \mathrm{CI} : [1.717,\ 1.992] \times 10^{-6}\ \mathrm{s}^{-1}\right).$$

The corresponding fitted times to reach 90%, 95%, and 99% of the asymptotic resistance increment were 344.9, 448.7, and $689.8\ \mathrm{h}$, respectively. These values extend beyond the experimental window and are therefore fit-based extrapolations rather than directly observed saturation times. At the end of the experiment, the fitted curve corresponded to approximately 82.8% of the asymptotic increment.

The effective concentration-normalised resistance-growth coefficient was calculated using the ideal Donnan estimate of the total mobile iron concentration in the membrane-water phase at 50% SoC, $C_{\mathrm{Fe,mem}}^{\mathrm{H-cell}} = 1595.79\ \mathrm{mol\,m^{-3}}$:

$$k_{\mathrm{block}} = \frac{k_{\mathrm{obs}}}{C_{\mathrm{Fe,mem}}^{\mathrm{H-cell}}} = \frac{1.8546 \times 10^{-6}}{1595.79} = 1.162 \times 10^{-9}\ \mathrm{m^3\,mol^{-1}\,s^{-1}}. \tag{4.6}$$

The corresponding fit-based 95% confidence interval was

$$[1.076,\ 1.248] \times 10^{-9}\ \mathrm{m^3\,mol^{-1}\,s^{-1}}.$$

This interval reflects uncertainty in the fitted k_{obs} only and is conditional on the adopted Donnan concentration. It does not include uncertainty in IEC, water uptake, activity effects, or iron–sulfate speciation.

The external iron concentration was treated as effectively constant during the experiment. Each $50\ \mathrm{mL}$ half-cell contained approximately $50\ \mathrm{mmol}$ total iron, whereas the iron capacity of the exposed membrane coupon was only of micromole order. Uptake by the membrane therefore represented a negligible fraction of the external iron inventory. The membrane-phase concentration was also treated as constant, which is a reduced-order approximation because any change in partitioning during resistance growth was not resolved explicitly.

Small structured deviations from the fitted curve are visible in Figure 4.15. Their origin was not independently determined and is theorised to involve temperature-control fluctuations, although instrumental drift, or changes in the electrode and contact response could play a role as well. No mechanistic significance is therefore assigned to these deviations.

4.5. Data-Assisted Model Results and Comparison with Experiment

This section evaluates whether the effective resistance-growth timescale derived from the Membrane X H-cell experiment remains consistent with the normalised resistance trajectory measured during stack cycling. The calculation is data-assisted rather than fully predictive: the measured current history is imposed as the electrical forcing, the left-tank Fe^{2+}/Fe^{3+} split is periodically re-anchored using OCV-derived SoC checkpoints, and the measured values of R_0 and $\Delta R_{\max}$ define the resistance scale. The H-cell-derived coefficient k_{block} is transferred to the stack model, while the principal calculated output is the temporal evolution of the resistance-growth.

The results are presented in two parts. First, the measured operating history, the transferred k_{block} value and its fit-derived confidence interval, and the nominal model–experiment comparison are presented together. Second, the robustness of the predicted trajectory to the adopted effective membrane ionic conductivity is evaluated using a set of plausible conductivity values. Supplementary model outputs are presented in Figure H.10 and Figure H.11.

4.5.1. Nominal Model-Experiment Comparison

The nominal model–experiment comparison was evaluated over the principal Membrane X operating interval defined in Section 4.1.1, corresponding to $t \geq 80\ \mathrm{h}$. The model was propagated from the beginning of the recorded test so that the calculated state at the start of the comparison interval retained the effect of the preceding current and SoC history. Only resistance measurements within the defined comparison window were used to calculate the reported goodness-of-fit metrics.

Figure 4.16 summarises the measured current history and the OCV-assimilated SoC trajectory over the comparison interval. The current trajectory is a prescribed model input rather than a calculated output. The model's calculated state of charge is periodically reset to the OCV-derived value at fixed checkpoints. Agreement between the model and the data at these checkpoints is therefore enforced by construction and does not constitute independent validation of the model. Between successive checkpoints, the continuous SoC trajectory is calculated from the Fe^{2+}/Fe^{3+} inventory balances and determines the time-dependent electrolyte composition supplied to the membrane-transport subproblem.

The effective concentration-normalised resistance-growth coefficient transferred from the H-cell experiment was

$$k_{\mathrm{block}} = 1.162 \times 10^{-9}\ \mathrm{m^3\,mol^{-1}\,s^{-1}}, \tag{4.7}$$

with a fit-derived 95% confidence interval of

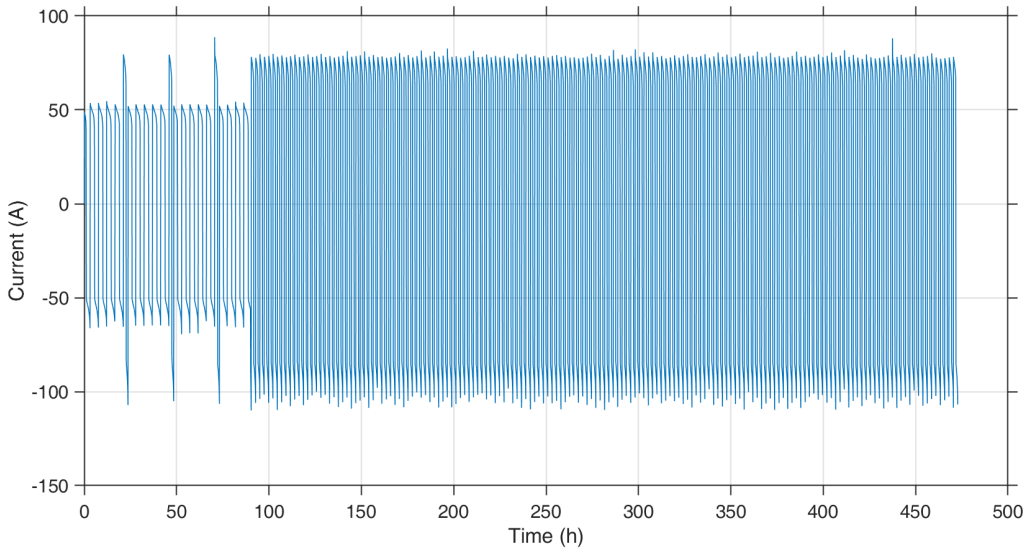
$$k_{\mathrm{block}} = [1.076,\ 1.248] \times 10^{-9}\ \mathrm{m^3\,mol^{-1}\,s^{-1}}. \tag{4.8}$$

The nominal simulation used the central value in Equation (4.7), together with $\kappa_{\mathrm{eff}} = 7.78\ \mathrm{S\,m^{-1}}$. The lower and upper bounds in Equation (4.8) were propagated through the same stack model while all other parameters and the measured operating history were held constant. The nominal model captured the

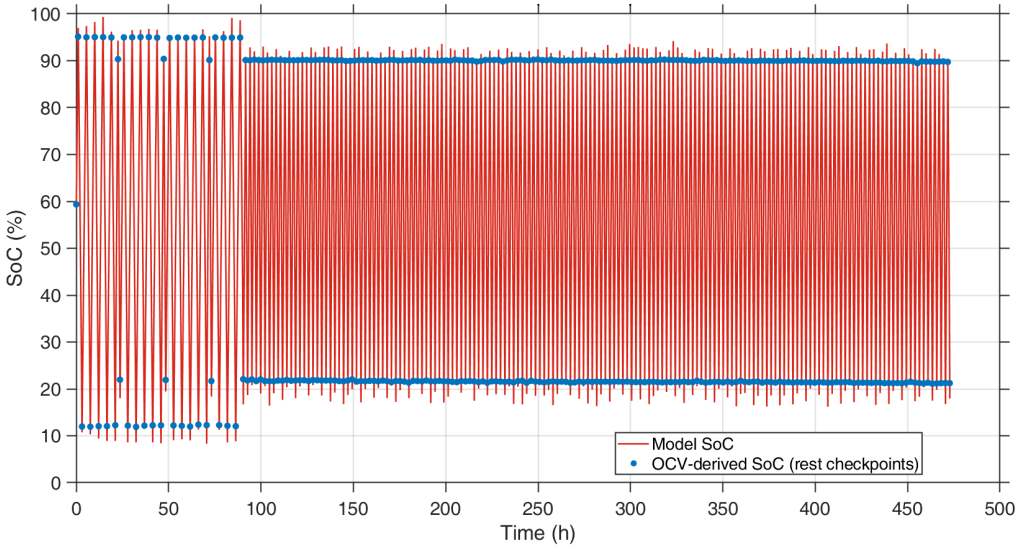
Case	k_{block} ($\mathrm{m^3\,mol^{-1}\,s^{-1}}$)	R^2	NRMSE (%)
Lower fit bound	1.076e-9	0.842	10.51
Nominal	1.162e-9	0.934	6.78
Upper fit bound	1.248e-9	0.962	5.16

Table 4.4: Effect of the H-cell fit-derived k_{block} interval on model agreement over the Membrane X comparison interval, 80-400 h.

monotonic resistance increase and its progressive deceleration, giving $R^2 = 0.934$ and an NRMSE of 7.13% over the corrected comparison interval. Propagating the H-cell fit-derived k_{block} interval produced R^2 values between 0.842 and 0.962, with NRMSE values between 10.51% and 5.16%. To confirm that this result does not depend on the choice of comparison window, the same three cases were additionally evaluated over the entire recorded test duration. This gave $R^2 = 0.942$ and an NRMSE of 4.92% for the nominal case, with the lower- and upper-bound cases spanning $R^2 = 0.873$–0.963 and NRMSE $= 7.29$–3.93%. The consistent level of agreement across both windows indicates that the reported fit quality is not an artefact of the chosen comparison interval.



(a) Measured current profile supplied to the model as input



(b) Model-calculated SoC trajectory, with periodic resets to the OCV-derived measured values

Figure 4.16: Measured operating history used in the data-assisted Membrane X simulation. The current history is imposed directly. The Fe^{2+}/Fe^{3+} inventory evolves continuously between OCV checkpoints and is re-anchored at the indicated rest-to-cycling transitions.

The upper-bound coefficient gave the closest agreement with the measured trajectory, indicating that the stack response was most consistent with the faster end of the independently derived H-cell range. Nevertheless, all three cases reproduced the same overall saturating resistance-growth behaviour. The comparison therefore supports the conditional transferability of the H-cell-derived coefficient while showing that its fit uncertainty has a measurable, but not qualitative, influence on the predicted trajectory.

4.5.2. Robustness to the Adopted Effective Membrane Ionic Conductivity

The effective membrane ionic conductivity was not estimated statistically from the stack data. Instead, the model was rerun using three plausible values spanning the adopted literature range [54]:

$$\kappa_{\mathrm{eff}} = 5.07,\ 7.78,\ \text{and}\ 10.49\ \mathrm{S\,m^{-1}}, \tag{4.9}$$

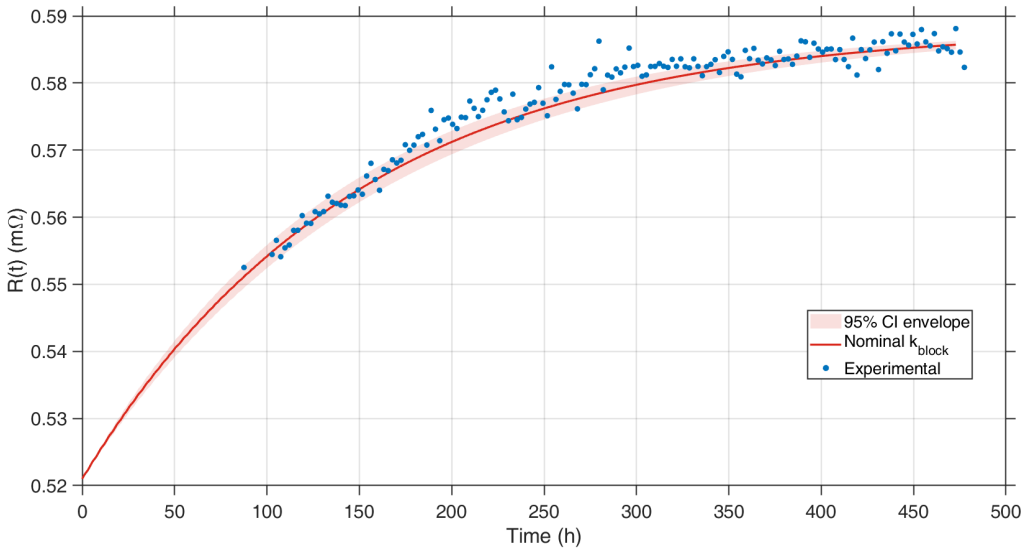


Figure 4.17: Measured apparent BOC cell resistance and calculated resistance-growth trajectories obtained using the nominal k_{block} and the lower and upper bounds of its H-cell fit-derived 95% confidence interval. The shaded region represents propagation of the H-cell fit uncertainty in k_{block} only. Because R_0 and $\Delta R_{\max}$ are stack-derived, the comparison evaluates the temporal resistance-growth trajectory rather than an independent prediction of the absolute resistance scale.

where $7.78\ \mathrm{S\,m^{-1}}$ is the nominal value. All other model parameters and the measured operating history were held constant. This one-at-a-time parameter variation is interpreted as a robustness check against the adopted conductivity assumption, rather than as a probabilistic uncertainty analysis or confidence interval.

The conductivity enters the transport model through the effective Ohmic field closure

$$E = \frac{j}{\kappa_{\mathrm{eff}}}. \tag{4.10}$$

A lower conductivity therefore produces a larger electric field at the same imposed current density and changes the electromigration contribution to Fe^{2+} and Fe^{3+} transport. Conductivity affects the calculated resistance trajectory only indirectly through the resulting iron-exposure history and resistance-growth state; R_0 and $\Delta R_{\max}$ remain fixed in all three cases.

Case	κ_{eff} ($\mathrm{S\,m^{-1}}$)	R^2	NRMSE (%)
Lower conductivity	5.07	0.956	5.56
Nominal conductivity	7.78	0.934	6.78
Higher conductivity	10.49	0.924	7.29

Table 4.5: Model agreement for the three adopted conductivity scenarios over the Membrane X comparison interval, 80-$400\ \mathrm{h}$.

All three conductivity scenarios reproduced the monotonic increase and progressive deceleration of the measured resistance trajectory. Across the tested range, R^2 remained between 0.924 and 0.956, while the NRMSE remained between 5.56% and 7.29%. The lower-conductivity case gave the closest agreement with the measured trajectory, whereas the higher-conductivity case predicted slightly slower resistance growth. The same three conductivity scenarios were also evaluated over the entire recorded test duration, giving R^2 values between 0.924 and 0.956 and NRMSE values between 4.20% and 5.24%. The comparable fit quality across both windows indicates that the robustness conclusions are not sensitive to the choice of comparison interval.

This ordering is consistent with the adopted field closure: for the measured current history, a lower κ_{eff} produces a stronger migration field and slightly greater cumulative iron exposure at the resistance-growth driver. The limited separation between the three trajectories indicates that the principal model

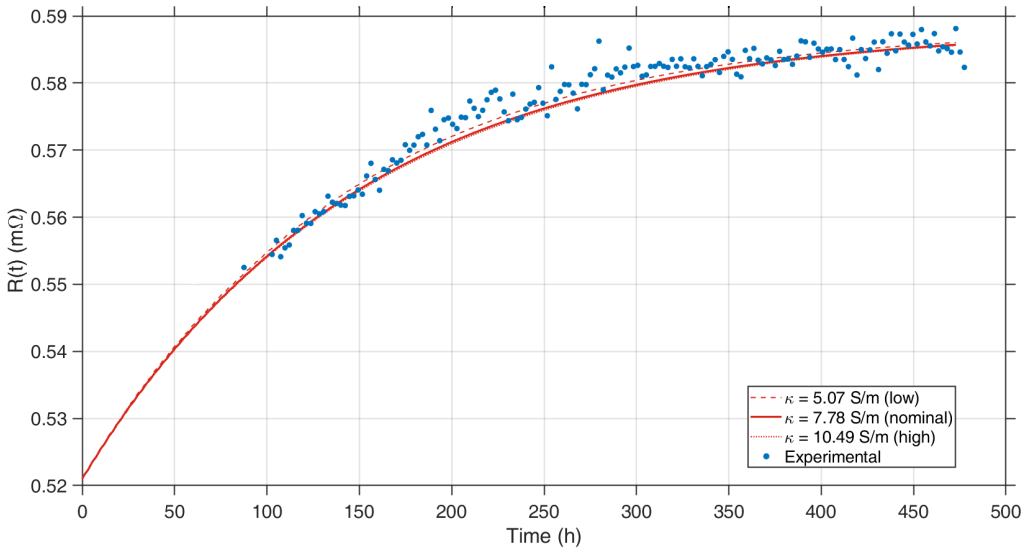


Figure 4.18: Effect of the adopted effective membrane ionic conductivity on the calculated Membrane X resistance-growth trajectory. The three curves represent discrete conductivity scenarios and are not a confidence interval. The goodness-of-fit metrics were evaluated over the comparison interval, 80-400 h.

result is relatively robust to the conductivity assumption over the tested literature range. Because the conductivity values were not fitted to the stack data, the closer agreement of the lower-conductivity case should not be interpreted as an independent measurement of the true Membrane X conductivity.

4.5.3. Model Limitations and Domain of Applicability

The present model is a reduced-order, data-assisted framework developed to test whether the resistance-growth coefficient obtained from the Membrane X H-cell experiment, when combined with a calculated stack iron-exposure history, is consistent with the normalised resistance trajectory of the tested stack. It is not intended as a complete multiphase stack model or as an independent predictor of absolute cell resistance.

The spatial representation consists of well-mixed zero-dimensional compartments coupled to a quasi-steady one-dimensional membrane-transport model. This enables simulations over several hundred hours, but excludes in-plane concentration gradients, local current-density nonuniformity, flow-distribution effects, detailed GDE hydration and purge dynamics, and short-time membrane storage. The model is therefore most applicable to long-timescale resistance trends rather than start-up or rapid switching transients.

Several physicochemical processes are represented through effective closures. Membrane diffusivities, ionic conductivity, water content, and fixed-charge concentration remain constant. Activities are approximated by concentrations, iron–sulfate complexes are not explicitly resolved, and the hydrogen-side boundary is represented by an effective hydrated volume estimated from water uptake. These assumptions may affect the calculated partitioning and fluxes when the electrolyte composition, hydration, temperature, or current density differs substantially from the tested conditions.

The resistance-growth state, θ, is phenomenological and represents the normalised progression of the apparent resistance response rather than a directly measured fraction of iron-occupied sulfonate sites. Fe^{2+} and Fe^{3+} are assigned equal molar weighting in the effective exposure variable, while desorption, recovery, and species-specific resistance effects are omitted. Furthermore, the coupling is one-way: resistance growth does not update membrane diffusivity, conductivity, water uptake, fixed charge, or Donnan partitioning.

For $\theta(0) = 0$, the adopted formulation gives

$$\theta(t) = 1 - \exp\left[-k_{\mathrm{block}} \int_0^t C^{\mathrm{eff}}_{\mathrm{Fe},R}(\tau)\, \mathrm{d}\tau\right]. \tag{4.11}$$

Consequently, operating histories with the same cumulative effective iron exposure produce the same value of θ, even if their Fe^{2+}/Fe^{3+} sequence, rest periods, or current-direction history differ. History-dependent recovery and species-specific effects therefore lie outside the present formulation.

The measured current history is imposed, the Fe^{2+}/Fe^{3+} split is periodically re-anchored using OCV-derived SoC checkpoints, and R_0 and $\Delta R_{\max}$ are obtained from the measured stack trajectory. The comparison therefore primarily evaluates the predicted temporal shape of the resistance response, rather than providing a blind prediction of its operating trajectory, baseline, or amplitude. Additionally, the apparent cell resistance may include contributions from the membrane, electrodes, GDE hydration, interfaces, and contact resistances. Agreement with the experiment therefore supports the conditional consistency of the iron-exposure-based formulation, but does not uniquely attribute the complete resistance increase to membrane iron retention or establish a specific microscopic mechanism.

Validation is currently limited to one Membrane X stack configuration and uncertainty analysis of selected parameters. Application to other membrane chemistries, electrolyte conditions, temperatures, current profiles, or stack designs requires independent validation.

5

Conclusions and Recommendations

5.1. Conclusions

RQ1: Candidate stack performance.

The screening framework reduced the initial candidate pool to three cation-exchange membranes: Nafion NR212 as the PFSA benchmark, Selemion CMVN as a crosslinked hydrocarbon membrane, and Membrane X as an alternative commercial hydrocarbon membrane.

In their respective tested stack configurations, NR212 and Membrane X sustained cycling for approximately 965 and $477\ \mathrm{h}$, respectively. Their apparent beginning-of-charge cell resistances increased at progressively decreasing rates and could be represented by saturating exponentials. This curvature is compatible with a finite-capacity resistance-growth process but does not uniquely establish iron site blocking as the underlying mechanism.

Membrane X showed an approximately 8% first-to-final resistance increase and an apparent approach to a plateau, whereas NR212 increased by approximately 35% and was still rising at the end of the longer test. The two tests differed in stack configuration, electrolyte volume, operating history, duration, and power setpoint; the results are therefore interpreted as candidate-level evidence rather than controlled intrinsic membrane properties. Within this scope, Membrane X showed the more favourable apparent resistance response and is the preferred candidate for further HyFe evaluation, while NR212 remains a viable PFSA benchmark.

The tested CMVN configuration did not sustain repeatable multi-cycle operation and did not provide a reliable resistance trajectory. Its visibly dry appearance suggests that membrane hydration warrants further investigation, but the electrochemical results do not identify a unique failure mechanism. CMVN should therefore not be advanced without independent replicate testing and targeted failure analysis.

RQ2: Post-cycling elemental evidence.

Post-cycling SEM–EDS produced Fe-related signals at selected locations on both analysed membrane samples. For NR212, software-reported Fe signals of 49–$86\ \mathrm{at.\%}$ were obtained at nominally featureless off-particle locations, while the sampled visible particulates were mainly Pt- or Pt/S-bearing. The magnitude of the Fe values is incompatible with homogeneous stoichiometric ion-exchange loading in intact Nafion and is therefore interpreted as qualitative evidence of a strong local Fe signal, not as a bulk membrane composition.

For Membrane X, low Fe-related signals were observed at several off-particle locations and one visible feature produced a locally higher signal. Charging, beam-induced instability, the absence of a reliable pristine EDS baseline, and poor analytical totals prevented quantitative interpretation.

The SEM–EDS results therefore demonstrate local Fe occurrence within the interaction volume at selected cycled-sample locations. They do not determine oxidation state, chemical coordination, binding

mechanism, through-thickness distribution, or comparative bulk Fe loading, and are not treated as independent validation of the resistance-growth model.

RQ3: Retained-iron behaviour.

For all three membranes, the amount of retained iron, the water-wash-resistant, NaCl-exchangeable fraction, was higher at the last time point (day 16) following exposure to the nominally Fe^{2+}-rich electrolyte than following exposure to the nominally Fe^{3+}-rich electrolyte. Accounting for the different charge stoichiometries of the two ions, however, revealed membrane-specific behaviour: NR212 showed approximately balanced charge-equivalent retention, CMVN showed greater retention following Fe^{2+}-rich exposure, and Membrane X showed greater retention following Fe^{3+}-rich exposure. The results therefore do not support a universal preference for either exposure condition across the three membrane chemistries.

The time dependence was also membrane- and exposure-specific. Membrane X approached an apparent plateau under both conditions by approximately day 2. For NR212, the Fe^{2+}-rich condition was approximately stable by day 2, while the Fe^{3+}-rich condition continued increasing until approximately day 5. CMVN showed the opposite timing pattern, with the Fe^{3+}-rich condition near its late-time value by day 1 and the Fe^{2+}-rich condition continuing to increase until approximately day 5. Both the retained inventory and its timescale were therefore apparently dependent on membrane chemistry and exposure condition.

RQ4: Conditional transfer of k_{block}.

The results support the conditional applicability of the H-cell-derived effective resistance-growth coefficient to the tested Membrane X stack configuration. When combined with the calculated time-dependent iron exposure, the nominal coefficient captured the monotonic increase and progressive deceleration of the normalised stack-resistance trajectory, giving $R^2 = 0.934$ and an NRMSE of 6.78% over the corrected 80-$477\ \mathrm{h}$ comparison interval.

The same qualitative behaviour was retained across the fit-derived k_{block} interval, and the result remained comparatively robust to the adopted effective ionic conductivity over the tested literature range. The H-cell-derived coefficient, therefore seems to be useful as an effective reduced-order parameter for interpreting the temporal resistance-growth behaviour of this Membrane X stack.

This conclusion depends on several modelling choices made in this work: the adopted concentration driver, the hydrogen-side boundary closure, the use of the measured current as a fixed model input, the periodic resetting of SoC to OCV-derived values, and the fact that the resistance scale is derived from the stack rather than from the membrane alone. It therefore does not establish k_{block} as a universal microscopic binding constant; it does not constitute an independent prediction of the absolute resistance increase; and it does not uniquely identify iron–sulfonate occupation as the sole cause of the observed resistance evolution.

5.2. Recommendations

1. Conduct matched replicate stack tests.

The candidate comparison should be repeated using independent membrane specimens and stack assemblies. At minimum, CMVN and Membrane X should be retested; ideally, NR212 should also be included in a fully replicated three-membrane study. Future tests should use matched stack hardware, membrane conditioning, electrolyte composition and volume, flow conditions, SoC window, and current density.

2. Resolve the CMVN failure mechanism and quantify membrane iron.

If CMVN instability is reproduced, pristine, electrolyte-soaked, and stack-cycled samples should be compared using XPS together with post-test IEC, water uptake, and ionic conductivity. Changes in the S 2p region may provide evidence of alteration of the sulfonate environment, but XPS alone should not be treated as proof of irreversible desulfonation [55].

For the cycled membranes more generally, complete digestion followed by ICP–OES or ICP–MS should first establish the total bulk Fe inventory. Cross-sectional SEM–EDS mapping could then determine whether Fe-related signals are surface-localised or distributed through the thickness [56]. Where sufficient Fe loading is available, Fe K-edge XAS could provide complementary information on average oxidation state and local coordination [57].

3. Test the origin of membrane-specific retained-iron behaviour.

The immersion experiments should be repeated using independent samples, oxygen-controlled handling, and verification of the Fe^{2+}/Fe^{3+} composition before and after exposure. Comparative isothermal titration calorimetry, or an equivalent microcalorimetric method, could then test whether the apparent Fe^{2+} and Fe^{3+} ion-exchange affinities of NR212, CMVN, and Membrane X follow the measured charge-equivalent retention order. Agreement would support a membrane-specific affinity mechanism, while a different ordering would indicate a stronger influence of electrolyte speciation, hydration, kinetics, or extraction recovery.

4. Validate the concentration scaling, parameter transferability, and hydrogen-side exposure closure.

The concentration normalisation used to define k_{block} should be evaluated by repeating the H-cell experiment at several controlled total-iron concentrations and Fe^{2+}/Fe^{3+} compositions. An approximately linear relationship between k_{obs} and the estimated membrane-phase mobile-iron concentration over the investigated range would support treating k_{block} as a concentration-independent coefficient under those conditions.

The resulting value of k_{block} should then be determined before analysing an independently assembled Membrane X stack and retained without refitting. The model should be applied to a second operating history to assess whether it reproduces the normalised resistance trajectory under independent conditions. Where feasible, measurements of iron in the hydrogen-side purge or collected crossover liquid, together with an estimate of the associated liquid inventory, should be used to constrain the effective hydrogen-side exposure term.

Successful reproduction of the independent stack trajectory would provide stronger evidence for both the transferability of k_{block} and the suitability of the hydrogen-side boundary closure. These validation steps should precede further increases in model complexity, so that any subsequent extensions are motivated by reproducible out-of-sample deviations rather than by improved fitting of the original dataset.

5. Introduce data-supported extensions to the model.

If independent validation reveals systematic deviations from the present formulation, individual assumptions should be relaxed in a stepwise and experimentally supported manner. For example, Fe^{2+} and Fe^{3+} could be assigned different effective contributions to resistance growth if controlled species-composition experiments demonstrate distinguishable effects. A recovery term should similarly be introduced only if reproducible resistance decreases are observed during rest, flushing, electrolyte replacement, or regeneration experiments.

Time-resolved quartz crystal microbalance measurements with dissipation monitoring (QCM-D) could support these extensions by measuring apparent iron-uptake and release transients in thin, compositionally representative ionomer films. The films could be exposed sequentially to Fe^{2+}-rich or Fe^{3+}-rich electrolyte and then to Fe-free acid or a controlled exchange solution. Repeating these concentration-step experiments at several iron concentrations could provide apparent species-specific association and recovery coefficients and help determine whether the net-growth relationship adopted in the present model is sufficient or whether a reversible form such as

$$\frac{d\theta}{dt} = \left(k_2 c_{2,R}^{\mathrm{eff}} + k_3 c_{3,R}^{\mathrm{eff}}\right)(1-\theta) - k_{\mathrm{rec}}\theta \tag{5.1}$$

is supported experimentally.

The present one-way coupling could also be extended if independent measurements show that iron exposure changes membrane properties. In that case, the resistance-growth state could be allowed to influence ionic conductivity, diffusivity, water uptake, or effective fixed-charge concentration, thereby affecting subsequent partitioning and transport. Further refinements, such as activity corrections, explicit iron–sulfate speciation, concentration-dependent transport properties, etc. should be prioritised according to the results of independent validation and sensitivity analysis.

References

[1] International Energy Agency, “Renewables 2025: Analysis and forecast to 2030,” IEA, Tech. Rep., 2025, Accessed June 2026. [Online]. Available: https://www.iea.org/reports/renewables-2025.

[2] B. Dunn, H. Kamath, and J.-M. Tarascon, “Electrical energy storage for the grid: A battery of choices,” *Science*, vol. 334, no. 6058, pp. 928–935, 2011. DOI: 10.1126/science.1212741.

[3] P. Albertus, J. S. Manser, and S. Litzelman, “Long-duration stationary energy storage: Ubiquitous, safe, and affordable,” *Joule*, vol. 4, no. 1, pp. 21–32, 2020. DOI: 10.1016/j.joule.2019.11.009.

[4] J. Deng, D. Pang, X. Yu, Y. Bai, and J. Mo, “Innovations and prospects on functional membrane design for advanced redox flow batteries,” *Applied Energy*, vol. 406, p. 127 316, 2026. DOI: 10.1016/j.apenergy.2025.127316.

[5] C. A. Machado, G. O. Brown, R. Yang, T. E. Hopkins, J. G. Pribyl, and T. H. E. III, “Redox flow battery membranes: Improving battery performance by leveraging structure–property relationships,” *ACS Energy Letters*, vol. 6, no. 2, pp. 648–660, 2021. DOI: 10.1021/acsenergylett.0c02205.

[6] J. R. Varcoe, P. Atanassov, D. R. Dekel, A. M. Herring, M. A. Hickner, P. A. Kohl, A. R. Kucernak, W. E. Mustain, K. Nijmeijer, K. Scott, T. Xu, and L. Zhuang, “Anion-exchange membranes in electrochemical energy systems,” *Energy & Environmental Science*, vol. 7, pp. 3135–3191, 2014. DOI: 10.1039/C4EE01303D.

[7] S. N. Oreiro, A. Bentien, J. Sloth, M. Rahimi, M. B. Madsen, and T. Drechsler, “Crossover analysis in a commercial 6 kw/43 kah vanadium redox flow battery utilizing anion exchange membrane,” *Chemical Engineering Journal*, p. 151 947, 2024. DOI: 10.1016/j.cej.2024.151947.

[8] T. T. K. Huynh, T. Yang, P. S. Nayanthara, Y. Yang, J. Ye, and H. Wang, “Construction of high-performance membranes for vanadium redox flow batteries: Challenges, development, and perspectives,” *Nano-Micro Letters*, vol. 17, p. 260, 2025. DOI: 10.1007/s40820-025-01736-x.

[9] T. Wong, Y. Yang, R. Tan, A. Wang, Z. Zhou, Z. Yuan, J. Li, D. Liu, A. Alvarez-Fernandez, C. Ye, M. Sankey, D. Ainsworth, S. Guldin, F. Foglia, N. B. McKeown, K. E. Jelfs, X. Li, and Q. Song, “Sulfonated poly(ether-ether-ketone) membranes with intrinsic microporosity enable efficient redox flow batteries for energy storage,” *Joule*, 2024. DOI: 10.1016/j.joule.2024.11.012.

[10] European Chemicals Agency. “ECHA supports PFAS restriction with targeted derogations.” Accessed: 2026-07-28, Accessed: Jul. 28, 2026. [Online]. Available: https://echa.europa.eu/-/echa-supports-pfas-restriction-with-targeted-derogations.

[11] C. Yang, L. Pan, and Q. Jian, “Recent advances in sulfonated poly(ether ether ketone) membrane for vanadium redox flow batteries,” *Future Batteries*, vol. 5, p. 100 026, 2025. DOI: 10.1016/j.fub.2025.100026.

[12] L. J. Small, H. D. Pratt III, and T. M. Anderson, “Crossover in membranes for aqueous soluble organic redox flow batteries,” *Journal of The Electrochemical Society*, vol. 166, no. 12, A2536–A2542, 2019. DOI: 10.1149/2.0681912jes.

[13] Y. Yang, Q. Wang, S. Xiong, and Z. Song, “Research progress on optimized membranes for vanadium redox flow batteries,” *Inorganic Chemistry Frontiers*, 2024. DOI: 10.1039/d4qi00520a.

[14] A. Kusoglu and A. Z. Weber, “New insights into perfluorinated sulfonic-acid ionomers,” *Chemical Reviews*, vol. 117, no. 3, pp. 987–1104, 2017. DOI: 10.1021/acs.chemrev.6b00159.

[15] S. He, S. Chai, and H. Li, “Nafion-based proton exchange membranes for vanadium redox flow batteries,” *ChemSusChem*, 2025. DOI: 10.1002/cssc.202402506.

[16] V. Pupkevich, V. Glibin, and D. Karamanev, “The effect of ferric ions on the conductivity of various types of polymer cation exchange membranes,” *Journal of Applied Electrochemistry*, vol. 37, no. 9, pp. 1031–1036, 2007. DOI: 10.1007/s10008-007-0306-4.

[17] Q. Wang, Z. Zhang, P. Lv, Z. Peng, and J. Yang, “Poly(terphenyl pyridine) based amphoteric and anion exchange membranes with high ionic selectivity for vanadium redox flow batteries,” *Chemical Engineering Journal*, p. 158 922, 2024. DOI: 10.1016/j.cej.2024.158922.

[18] S. Sreenath, C. M. Pawar, P. Bavdane, D. Y. Nikumbe, and R. K. Nagarale, “A sulfonated polyethylene–styrene cation exchange membrane: A potential separator material in vanadium redox flow battery applications,” *Sustainable Energy & Fuels*, 2021. DOI: 10.1039/d1ya00059d.

[19] M. C. Tucker, V. Srinivasan, P. N. Ross, and A. Z. Weber, “Performance and cycling of the iron-ion/hydrogen redox flow cell with various catholyte salts,” *Journal of Applied Electrochemistry*, vol. 43, no. 6, pp. 637–644, 2013. DOI: 10.1007/s10800-013-0553-2.

[20] C. He, Y. Zhang, S. Zhang, X. Peng, J. Noack, M. Skyllas-Kazacos, L. Wang, and B. Luo, “Aqueous iron-based redox flow batteries for large-scale energy storage,” *National Science Review*, vol. 12, no. 7, nwaf218, 2025. DOI: 10.1093/nsr/nwaf218.

[21] T. Okada, Y. Ayato, M. Yuasa, and I. Sekine, “The effect of impurity cations on the transport characteristics of perfluorosulfonated ionomer membranes,” *Journal of Physical Chemistry B*, vol. 103, no. 16, pp. 3315–3322, 1999. DOI: 10.1021/jp983762d.

[22] K. Kawai, T. Mabuchi, and T. Tokumasu, “Molecular dynamics analysis of proton diffusivity in hydrated Nafion membranes contaminated with ferrous ions,” *Macromolecular Theory and Simulations*, vol. 29, no. 1, p. 1 900 047, 2020. DOI: 10.1002/mats.201900047.

[23] M. Mukaddam, Y. Wang, and I. Pinnau, “Structural, thermal, and gas-transport properties of Fe^{3+} ion-exchanged Nafion membranes,” *ACS Omega*, vol. 3, no. 7, pp. 7474–7482, 2018. DOI: 10.1021/acsomega.8b00914.

[24] X. Wang, L. Zhang, G. Li, G. Zhang, Z.-G. Shao, and B. Yi, “The influence of ferric ion contamination on the solid polymer electrolyte water electrolysis performance,” *Electrochimica Acta*, vol. 158, pp. 253–257, 2015. DOI: 10.1016/j.electacta.2015.01.140.

[25] N. Li, S. S. Araya, X. Cui, and S. K. Kær, “The effects of cationic impurities on the performance of proton exchange membrane water electrolyzer,” *Journal of Power Sources*, vol. 473, p. 228 617, 2020. DOI: 10.1016/j.jpowsour.2020.228617.

[26] N. Remmler and M. Bron, “Recent progress in our understanding of the degradation of carbon-based electrodes in vanadium redox flow batteries — current status and next steps,” *ChemElectroChem*, vol. 11, e202400127, 2024. DOI: 10.1002/celc.202400127.

[27] W. Sun, N. Kim, A. M. Ebrahim, S. Sharma, A. Hollas, Q. Huang, D. M. Reed, E. C. Thomsen, V. Murugesan, A. van Buuren, L. F. Wan, and J. R. I. Lee, “Coupled experimental–theoretical characterization of a carbon electrode in vanadium redox flow batteries using X-ray absorption spectroscopy,” *ACS Applied Materials & Interfaces*, vol. 16, no. 7, pp. 8791–8801, 2024. DOI: 10.1021/acsami.3c17049.

[28] P. Loktionov, A. Pustovalova, R. Pichugov, D. Konev, and A. Antipov, “Quantifying effect of faradaic imbalance and crossover on capacity fade of vanadium redox flow battery,” *Electrochimica Acta*, vol. 485, p. 144 047, 2024. DOI: 10.1016/j.electacta.2024.144047.

[29] M. Vijayakumar, M. S. Bhuvaneswari, P. Nachimuthu, B. Schwenzer, S. Kim, Z. Yang, J. Liu, G. L. Graff, S. Thevuthasan, and J. Hu, “Spectroscopic investigations of the fouling process on Nafion membranes in vanadium redox flow batteries,” *Journal of Membrane Science*, vol. 366, no. 1–2, pp. 325–334, 2011. DOI: 10.1016/j.memsci.2010.10.018.

[30] J. Zhu, X. Yang, F. Fan, and Y. Li, “Factors affecting the determination of iron species in the presence of ferric iron,” *Applied Water Science*, vol. 8, p. 228, 2018. DOI: 10.1007/s13201-018-0876-6.

[31] H. Prifti, A. Parasuraman, S. Winardi, T. M. Lim, and M. Skyllas-Kazacos, “Membranes for redox flow battery applications,” *Membranes*, vol. 2, no. 2, pp. 275–306, 2012. DOI: 10.3390/membranes2020275.

[32] N. Hallemans, D. Howey, A. Battistel, N. F. Saniee, F. Scarpioni, B. Wouters, F. L. Mantia, A. Hubin, W. D. Widanage, and J. Lataire, “Electrochemical impedance spectroscopy beyond linearity and stationarity—a critical review,” *Electrochimica Acta*, vol. 466, p. 142 939, 2023. DOI: 10.1016/j.electacta.2023.142939.

[33] A. Trovo, G. Zamboni, and M. Guarnieri, “Multichannel electrochemical impedance spectroscopy and equivalent circuit synthesis of a large-scale vanadium redox flow battery,” *Journal of Power Sources*, vol. 229, pp. 273–283, 2021. DOI: 10.1016/j.jpowsour.2021.229703.

[34] M. Becker and T. Turek, “Combination of impedance spectroscopy and potential probe sensing to characterize vanadium redox-flow batteries,” *Journal of Power Sources*, vol. 446, p. 227 349, 2020. DOI: 10.1016/j.jpowsour.2019.227349.

[35] A. M. Pezeshki, R. L. Sacci, F. M. Delnick, D. S. Aaron, and M. M. Mench, “Elucidating effects of cell architecture, electrode material, and solution composition on overpotentials in redox flow batteries,” *Electrochimica Acta*, vol. 229, pp. 261–270, 2017. DOI: 10.1016/j.electacta.2017.01.056.

[36] J. Newman and K. E. Thomas-Alyea, *Electrochemical Systems*, 3rd ed. Hoboken, NJ, USA: Wiley, 2004.

[37] A. A. Shah, M. J. Watt-Smith, and F. C. Walsh, “A dynamic performance model for redox-flow batteries involving soluble species,” *Electrochimica Acta*, vol. 53, no. 27, pp. 8087–8100, 2008. DOI: 10.1016/j.electacta.2008.05.067.

[38] M. Pugach, M. Kondratenko, S. Briola, and A. Bischi, “Zero dimensional dynamic model of vanadium redox flow battery cell incorporating all modes of vanadium ions crossover,” *Applied Energy*, vol. 226, pp. 560–569, 2018. DOI: 10.1016/j.apenergy.2018.05.124.

[39] S. Mareev, A. Gorobchenko, D. Ivanov, D. Anokhin, and V. Nikonenko, “Ion and water transport in ion-exchange membranes for power generation systems: Guidelines for modeling,” *International Journal of Molecular Sciences*, vol. 24, no. 1, p. 34, 2023. DOI: 10.3390/ijms24010034.

[40] T. A. Zawodzinski, C. Derouin, S. Radzinski, R. J. Sherman, V. T. Smith, T. E. Springer, and S. Gottesfeld, “Water uptake by and transport through Nafion 117 membranes,” *Journal of The Electrochemical Society*, vol. 140, no. 4, pp. 1041–1047, 1993. DOI: 10.1149/1.2056194.

[41] D. You, H. Zhang, and J. Chen, “A simple model for the vanadium redox battery,” *Electrochimica Acta*, vol. 54, no. 27, pp. 6827–6836, 2009. DOI: 10.1016/j.electacta.2009.06.086.

[42] K. W. Knehr, E. Agar, C. R. Dennison, A. R. Kalidindi, and E. C. Kumbur, “A transient vanadium flow battery model incorporating vanadium crossover and water transport through the membrane,” *Journal of The Electrochemical Society*, vol. 159, no. 9, A1446–A1459, 2012. DOI: 10.1149/2.017209jes.

[43] F. T. Wandschneider, D. Finke, S. Grosjean, P. Fischer, K. Pinkwart, J. Tübke, and H. Nirschl, “Model of a vanadium redox flow battery with an anion exchange membrane and a Larminie-correction,” *Journal of Power Sources*, vol. 272, pp. 436–447, 2014. DOI: 10.1016/j.jpowsour.2014.08.082.

[44] Q. Dai, T. Liu, X. Li, and Y. Wang, “Overcoming the trade-off between ionic conductivity and selectivity in redox flow battery membranes,” *Nature Communications*, vol. 11, no. 1, p. 13, 2020. DOI: 10.1038/s41467-019-13704-2.

[45] X. Wang, H. Li, and Y. Zhang, “Ion-selective membranes for redox flow batteries: Challenges and future directions,” *Membranes*, vol. 13, no. 9, p. 777, 2023. DOI: 10.3390/membranes13090777.

[46] C. E. Evans, R. D. Noble, S. Nazeri-Thompson, B. Nazeri, and C. A. Koval, “Role of conditioning on water uptake and hydraulic permeability of Nafion® membranes,” *Journal of Membrane Science*, vol. 279, no. 1–2, pp. 521–528, 2006. DOI: 10.1016/j.memsci.2005.12.046.

[47] E. J. F. Dickinson, J. G. Limon-Petersen, and R. G. Compton, “The electroneutrality approximation in electrochemistry,” *Journal of Solid State Electrochemistry*, vol. 15, no. 7-8, pp. 1335–1345, 2011. DOI: 10.1007/s10008-011-1323-x.

[48] A. Münchinger and K.-D. Kreuer, “Selective ion transport through hydrated cation and anion exchange membranes I. The effect of specific interactions,” *Journal of Membrane Science*, vol. 592, p. 117 372, 2019. DOI: 10.1016/j.memsci.2019.117372.

[49] F. D. Coms and A. B. LaLonde, “Determination of Ce^{3+}, Co^{2+}, Mn^{2+} and Fe^{2+} diffusion coefficients in nafion® membrane,” *Journal of Power Sources*, vol. 572, p. 233 359, 2023. DOI: 10.1016/j.jpowsour.2023.233359.

[50] K. L. Hawthorne, J. S. Wainright, and R. F. Savinell, "Studies of iron-ligand complexes for an all-iron flow battery application," *Journal of The Electrochemical Society*, vol. 161, no. 10, A1662–A1671, 2014. DOI: 10.1149/2.0761410jes.

[51] A. Á. Moya, "Simple analytical approximations for Donnan ion partitioning in permeable ion-exchange membranes under reverse electrodialysis conditions," *Membranes*, vol. 15, no. 12, p. 365, 2025. DOI: 10.3390/membranes15120365.

[52] K. Hongsirikarn, J. G. J. Goodwin, S. Greenway, and S. Creager, "Effect of cations (Na^{+}, Ca^{2+}, Fe^{3+}) on the conductivity of a nafion membrane," *Journal of Power Sources*, vol. 195, no. 21, pp. 7213–7220, 2010. DOI: 10.1016/j.jpowsour.2010.05.005.

[53] B. Ling, P. Xie, D. Ladner, and I. Battiato, "Dynamic modeling of fouling in reverse osmosis membranes," *Membranes*, vol. 11, no. 5, p. 349, 2021. DOI: 10.3390/membranes11050349.

[54] F. Wang, D. Mu, and Y.-C. Lu, "Ion-conducting membranes for long-duration energy storage," *ACS Energy Letters*, vol. 10, no. 7, pp. 3096–3111, Jul. 2025. DOI: 10.1021/acsenergylett.5c00934. [Online]. Available: https://doi.org/10.1021/acsenergylett.5c00934.

[55] K. S. Siow, L. Britcher, S. Kumar, and H. J. Griesser, "XPS study of sulfur and phosphorus compounds with different oxidation states," *Sains Malaysiana*, vol. 47, no. 8, pp. 1913–1922, 2018. DOI: 10.17576/jsm-2018-4708-33.

[56] R. R. Ferlita, D. Phipps, J. Safarik, and D. H. Yeh, "Cryo-snap: A simple modified freeze-fracture method for SEM imaging of membrane cross-sections," *Environmental Progress*, vol. 27, no. 2, pp. 204–209, 2008. DOI: 10.1002/ep.10270.

[57] H. Wu, A. Ikeda-Ohno, Y. Wang, and T. D. Waite, "Iron and phosphorus speciation in Fe-conditioned membrane bioreactor activated sludge," *Water Research*, vol. 76, pp. 213–226, 2015. DOI: 10.1016/j.watres.2015.02.020.

[58] S. S. Sha'rani, N. W. C. Jusoh, E. Abouzari-Lotf, A. Ahmad, and R. R. Ali, "Evaluation of perfluorinated sulfonic acid membranes for vanadium redox," *IOP Conference Series: Materials Science and Engineering*, vol. 808, no. 1, p. 012 026, 2020. DOI: 10.1088/1757-899X/808/1/012026.

[59] E. Bai, H. Zhu, C. Sun, G. Liu, X. Xie, C. Xu, and S. Wu, "A comparative study of nafion 212 and sulfonated poly(ether ether ketone) membranes with different degrees of sulfonation on the performance of iron-chromium redox flow battery," *Membranes*, vol. 13, no. 10, p. 820, 2023. DOI: 10.3390/membranes13100820.

[60] H. Hou, S. Wang, W. Jin, Q. Jiang, L. Sun, L. Jiang, and G. Sun, "KOH modified nafion112 membrane for high performance alkaline direct ethanol fuel cell," *International Journal of Hydrogen Energy*, vol. 36, no. 11, pp. 6876–6881, 2011. DOI: 10.1016/j.ijhydene.2010.12.093.

[61] Z. Li and Y.-C. Lu, "Polysulfide-based redox flow batteries with long life and low levelized cost enabled by charge-reinforced ion-selective membranes," *Nature Energy*, vol. 6, no. 4, pp. 396–403, 2021. DOI: 10.1038/s41560-021-00804-x.

[62] R. M. Darling, A. Z. Weber, M. C. Tucker, and M. L. Perry, "The influence of electric field on crossover in redox-flow batteries," *Journal of The Electrochemical Society*, vol. 163, no. 1, A5014–A5022, 2016. DOI: 10.1149/2.0031601jes.

[63] T. Lei, Y. Xu, Y. Li, L. Huang, L. Ma, D. Si, K. Wang, F. Wang, J. Liu, L. Lei, L. Cao, and Y. Yang, "Recent advances in all-iron flow batteries (AIFBs)," *Current Opinion in Electrochemistry*, vol. 52, p. 101 702, 2025. DOI: 10.1016/j.coelec.2025.101702.

[64] Z. Zhu, Y. Meng, M. Wang, Y. Yin, and W. Chen, "A high-performance aqueous iron–hydrogen gas battery," *Materials Today Energy*, vol. 19, p. 100 603, 2021. DOI: 10.1016/j.mtener.2020.100603.

[65] T. Wong, Y. Yang, R. Tan, K. E. Jelfs, X. Li, and Q. Song, "Sulfonated poly(ether-ether-ketone) membranes with intrinsic microporosity enable efficient redox flow batteries for energy storage," *Joule*, 2024. DOI: 10.1016/j.joule.2024.11.012.

[66] R. Tan, A. Wang, C. Ye, J. Li, D. Liu, B. P. Darwich, L. Petit, Z. Fan, T. Wong, A. Alvarez-Fernandez, M. Furedi, and S. Guldin, "Thin film composite membranes with regulated crossover and water migration for long-life aqueous redox flow batteries," *Advanced Science*, vol. 10, no. 17, p. 2 206 888, 2023. DOI: 10.1002/advs.202206888.

[67] S. Abbasi, Y. A. Hugo, Z. Borneman, W. Kout, and K. Nijmeijer, “Long-term performance of hydrogen-bromine flow batteries using single-layered and multi-layered wire-electrospun SPEEK/PFSA/PVDF membranes,” *Sustainable Energy & Fuels*, vol. 8, no. 7, pp. 1549–1565, 2024. DOI: 10.1039/D3SE01670F.

[68] R. P. J. Dowd, A. Verma, Y. Li, D. Powers, R. Wycisk, P. N. Pintauro, and T. V. Nguyen, “A hydrogen-vanadium reversible fuel cell crossover study,” *Journal of The Electrochemical Society*, vol. 164, no. 14, F1608–F1615, 2017. DOI: 10.1149/2.11001714jes.

[69] A. Parekh, “Recent developments of proton exchange membranes for pemfc: A review,” *Frontiers in Energy Research*, vol. 10, p. 956 132, 2022. DOI: 10.3389/fenrg.2022.956132.

[70] Y. Gao, C. Wang, H. Ye, and Y. Zhang, “Highly ion-selective sulfonated poly (4,4′-diphenylether-5,5′-bibenzimidazole) membranes for vanadium redox flow battery,” *Journal of Sulfur Chemistry*, vol. 45, no. 3, p. 2 327 288, 2024. DOI: 10.1080/17458080.2024.2327288.

[71] B. E. Anley, C.-J. Yu, T.-Y. Wu, C.-C. Huang, J.-S. Wang, and H.-C. Tsai, “Polybenzimidazole membranes doped with sulfonic acid-containing covalent organic frameworks and polymers for enhanced performance in vanadium redox flow batteries,” *ACS Applied Materials & Interfaces*, vol. 17, no. 26, 2025. DOI: 10.1021/acsami.5c00568.

[72] F. Lulay, C. Weidlich, M. Valtiner, and C. M. Pichler, “Membrane degradation in redox flow batteries,” *Green Chemistry Letters and Reviews*, vol. 16, no. 1, p. 2 274 529, 2023. DOI: 10.1080/17518253.2023.2274529.

[73] Y. A. Gandomi, D. S. Aaron, Z. B. Nolan, A. Ahmadi, and M. M. Mench, “Direct measurement of crossover and interfacial resistance of ion-exchange membranes in all-vanadium redox flow batteries,” *Membranes*, vol. 10, no. 6, p. 126, 2020. DOI: 10.3390/membranes10060126.

[74] H. L. M. T. Tsehaye X. Wang and Y. Zhang, “Modified membranes for redox flow batteries-a review,” *Membranes*, vol. 13, no. 9, p. 777, 2023. DOI: 10.3390/membranes13090777.

[75] N. Zhao, H. Riley, C. Song, Z. Jiang, K.-C. Tsay, R. Neagu, and Z. Shi, “Ex-situ evaluation of commercial polymer membranes for vanadium redox flow batteries (vrfbs),” *Polymers*, vol. 13, no. 6, p. 0926, 2021. DOI: 10.3390/polym13060926.

[76] R. Kim, H. G. Kim, G. Doo, C. Choi, S. Kim, J.-H. Lee, J. Heo, H.-Y. Jung, and H.-T. Kim, “Ultrathin nafion-filled porous membrane for zinc/bromine redox flow batteries,” *Scientific Reports*, vol. 7, p. 10 503, 2017. DOI: 10.1038/s41598-017-10850-9.

[77] L. F. Söffker, T. Turek, U. Kunz, and L. F. Arenas, “Screening of cation exchange membranes for an anthraquinone-ferrocyanide flow battery,” *ChemElectroChem*, vol. 11, no. 22, e202400516, 2024. DOI: 10.1002/celc.202400516.

[78] C. Christov and N. Moller, “Chemical equilibrium model of solution behavior and solubility in the H–Na–K–OH–Cl–HSO4–SO4–H2O system to high concentration and temperature,” *Geochimica et Cosmochimica Acta*, vol. 68, no. 6, pp. 1309–1331, 2004. DOI: 10.1016/j.gca.2003.08.017.

[79] A. G. Dickson, D. J. Wesolowski, D. A. Palmer, and R. E. Mesmer, “Dissociation constant of bisulfate ion in aqueous sodium chloride solutions to 250 °c,” *The Journal of Physical Chemistry*, vol. 94, no. 20, pp. 7978–7985, 1990. DOI: 10.1021/j100383a042.

A

List of membranes from literature

The membrane candidates identified in the literature survey were evaluated using a selectivity ratio Φ/Φ_{Naf}, where the selectivity $\Phi = \sigma/P$ is the ratio of ionic conductivity to counter-ion permeability, and Φ_{Naf} is the corresponding selectivity of Nafion NR212 (or Nafion 117 where NR212 data was unavailable) tested under the same battery chemistry as the candidate membrane. This normalisation accounts for the fact that the relevant counter-ion species, and hence the permeability values, differ between chemistries (e.g. vanadium in VRFB, iron in Fe–aqueous). The reference Nafion selectivity values used for each chemistry are listed in Table A.1. For chemistries where a direct Nafion measurement was not available in the literature, the nearest equivalent chemistry was used and noted accordingly. The full membrane candidate list with computed selectivity ratios is given in Table A.2.

Table A.1: Reference Nafion selectivity $\Phi_{\mathrm{Naf}} = \sigma/P$ used to normalise the selectivity ratio column in Table A.2, organised by battery chemistry. Values marked † were not directly available and were estimated from the nearest compatible chemistry or source (see notes).

Battery Chemistry	σ (S m^{-1})	P (m^2 s^{-1})	Φ_{Naf} (S s m^{-3})	Reference
VRFB	8.8	4.00×10^{-12}	2.20×10^{12}	[58]
ICRFB	—	—	2.16×10^{13}	[59]
Fe–aqueous	10	9.00×10^{-11}	1.11×10^{11}	[49]
Alkaline AORFB	1.1	1.50×10^{-12}	7.33×10^{11}	[60]†
PSIRFB	0.23	7.43×10^{-13}	3.10×10^{11}	[61]
Neutral AORFB	0.26	4.00×10^{-12}	6.50×10^{10}	[52]††

† Ionic conductivity measured in 1 M KOH; permeability estimated from nearest available source.
†† Permeability estimated from a similar ion like Vanadium

Table A.2: Membrane candidate list screened for Fe–H_2 RFB application. Selectivity S = σ/P and ratio Ψ/Ψ_{Naf} are calculated quantities (†). Conductivity values converted from reported ASR are marked ‡.

No.	Membrane	Type	Chemistry	IEC (meq g^{-1})	δ (µm)	σ (S m^{-1})	P (m^2 s^{-1})	$S^{\dagger}$ (S s m^{-3})	$\Psi/\Psi_{\mathrm{Naf}}{}^{\dagger}$	Ref.
1	SPI-DH-60	Sulfonated polyimide (SPI)	VRFB	—	60	10.1	2.30×10^{-13}	4.39×10^{13}	19.96	[4]
2	1.5% TPB-PBAP	Acid-doped branched poly(biphenyl pyridine)	VRFB	—	55	7.45	7.67×10^{-14}	9.71×10^{13}	44.15	[4]
3	MS-PBI	Sulfonated para-polybenzimidazole	VRFB	—	23	6.5	1.31×10^{-13}	4.96×10^{13}	22.55	[4]
4	s-OPBI 102	Sulfonated polybenzimidazole	VRFB	—	102	7	5.15×10^{-13}	1.36×10^{13}	6.18	[4]
5	bipCTF/SP-100	Covalent triazine framework composite	VRFB	—	69	2.3 ‡	1.91×10^{-12}	—	0.55	[4]
6	S/UiO-66-PS-2	SPEEK + Zr-MOF composite	VRFB	—	59	9.83	5.10×10^{-11}	1.93×10^{11}	0.09	[4]
7	SPI-B-50	Branched sulfonated polyimide	VRFB	—	40	1.64	1.18×10^{-13}	1.39×10^{13}	6.32	[4]
8	b-DPM-N3	Hydrocarbon membrane (commercial-scale)	VRFB	—	20-25	0.48 ‡	1.06×10^{-16}	—	2045.45	[4]
9	C-abSPI-10	Cross-linked asymmetric sulfonated polyimide	VRFB	—	—	—	—	—	—	[4]
10	PSSP (1–25–25–1)	PBI / sulfonated polystyrene multilayer membrane	VRFB	—	Layered: 1+25+25+1	3.6 ‡	6.85×10^{-14}	—	23.64	[4]
11	HF-SCOF nano-pipeline ICM	Sulfonated covalent organic framework membrane	VRFB	—	—	—	—	—	—	[4]
12	Gore M715.18	PFSA-based reinforced membrane (Gore)	Fe-H2	—	18	—	—	—	—	[62]
13	Gore M60111PC	PFSA-based reinforced membrane (Gore)	Fe-H2	—	60	—	—	—	—	[62]
14	Daramic 250	Microporous polyolefin separator	Fe-H2	—	250	—	—	—	—	[62]

Continued on next page…

No.	Membrane	Type / Chemistry	System	IEC (meq g^{-1})	δ (µm)	σ (S m^{-1})	P (m^2 s^{-1})	$\Phi^{\dagger}$ (S s m^{-3})	$\Phi/\Phi_{\mathrm{Naf}}{}^{\dagger}$	Ref.
15	SPEEK	Sulfonated PEEK	—	—	—	22.2	3.22×10^{-12}	6.89×10^{12}	—	[11]
16	SPEEK/PTFE-0.5%	SPEEK + PTFE filler	VRFB	—	—	2.72	8.67×10^{-12}	3.14×10^{11}	0.14	[11]
17	CrSPK45-S	Cross-linked SPEEK	VRFB	—	—	12.6	6.10×10^{-13}	2.07×10^{13}	9.39	[11]
18	TC-SPEEK/0.5	Thermally cross-linked SPEEK + ABPBI-GO	VRFB	—	—	13.4	1.70×10^{-12}	7.89×10^{12}	3.59	[11]
19	SPEEK/FCB-3	SPEEK + functional carbon black	VRFB	—	—	9.24	1.30×10^{-13}	7.11×10^{13}	32.31	[11]
20	SPEEK/S-TiO_2-3	SPEEK + sulfonated TiO_2	VRFB	—	—	2.32	1.17×10^{-12}	1.99×10^{12}	0.90	[11]
21	SPEEK72/L15	SPEEK–Lignin	VRFB	—	—	—	—	—	14.45	[11]
22	SPEEK59/L15	SPEEK–Lignin	VRFB	—	—	—	—	—	18.55	[11]
23	SPEEK50/L15	SPEEK–Lignin	VRFB	—	—	—	—	—	15.55	[11]
24	SPEEK41/L15	SPEEK–Lignin	VRFB	—	—	—	—	—	11.45	[11]
25	SPEEK-PEI	PEI-coated SPEEK	VRFB	—	—	9.1	7×10^{-13}	1.30×10^{13}	5.91	[11]
26	SPEEK/SP@PVDF	—	VRFB	—	—	10	3.30×10^{-13}	3.03×10^{13}	13.77	[11]
27	PDA/SPEEK	—	VRFB	—	—	1.25	2.78×10^{-13}	4.50×10^{12}	2.04	[11]
28	P-S-P	PAN/SPEEK/PAN	VRFB	—	—	—	—	—	—	[11]
29	SPEEK/TiO_2 nanopaper	—	VRFB	—	—	2.66	1.15×10^{-12}	2.31×10^{12}	1.05	[11]
30	S/P/P	SPEEK/PP/PFSA	VRFB	—	—	1.52	3.25×10^{-13}	4.68×10^{12}	2.13	[11]
31	Nafion/h-BN/SPEEK	—	VRFB	—	—	3.97	3.17×10^{-13}	1.25×10^{13}	5.69	[11]
32	P/S	$[PDDA/PSS]_6$	VRFB	—	—	0.26	3.12×10^{-13}	8.33×10^{11}	0.38	[11]
33	Daramic W0733	Microporous polymer separator	IRFB	—	—	—	—	—	—	[63]
34	GF 8, Whatman	Microporous glass fiber separator	Fe-H2	—	—	—	—	—	—	[64]
35	sPEEK-Trip-1.50	Sulfonated PEEK with triptycene microporosity	Alkaline/Aq AORFB	1.5	50	0.9	2.50×10^{-14}	—	49.09	[65]

Continued on next page…

No.	Membrane	Type / Chemistry	System	IEC (meq g^{-1})	δ (µm)	σ (S m^{-1})	P (m^2 s^{-1})	$\Phi^{\dagger}$ (S s m^{-3})	$\Phi/\Phi_{\mathrm{Naf}}{}^{\dagger}$	Ref.
36	sPEEK-Trip-1.55	Sulfonated PEEK with triptycene microporosity	Alkaline/Aq AORFB	1.55	50	2.3	2×10^{-14}	1.15×10^{14}	156.82	[65]
48	sPEEK-Trip-1.85	Sulfonated PEEK with triptycene microporosity	Alkaline/Aq AORFB	1.85	50	3	2×10^{-14}	—	204.55	[65]
37	PIM-EA-TB-0.3	Polymer of intrinsic microporosity (PIM-EA-TB) thin-film composite membrane on PAN support	Neutral Aq ORFB	—	0.3 (selective layer)	—	—	—	—	[66]
38	PIM-EA-TB-1.3	Polymer of intrinsic microporosity (PIM-EA-TB) thin-film composite membrane on PAN support	Neutral Aq ORFB	—	1.3 (selective layer)	0.199-0.33	—	—	—	[66]
39	PIM-EA-TB-4	Polymer of intrinsic microporosity (PIM-EA-TB) thin-film composite membrane on PAN support	Neutral Aq ORFB	—	4 (selective layer)	0.199-0.33	—	—	—	[66]
40	PIM-EA-TB-12	Polymer of intrinsic microporosity (PIM-EA-TB) thin-film composite membrane on PAN support	Neutral Aq ORFB	—	12 (selective layer)	0.199-0.33	—	—	—	[66]
41	SPF1-0	Single-layered SPEEK/PFSA/PVDF blend membrane 0/50/50 wt%	H2-Br	0.54	94	—	—	—	—	[67]
42	SPF1-8	Single-layered SPEEK/PFSA/PVDF 8/42/50 wt%	H2-Br	0.57	62	—	—	—	—	**[67]**
43	SPF2-8	Multi-layered SPEEK/PFSA/PVDF 8/42/50 wt% (layered)	H2-Br	0.61	42	—	—	—	—	**[67]**

Continued on next page…

No.	Membrane	Type / Chemistry	System	IEC (meq g^{-1})	δ (µm)	σ (S m^{-1})	P (m^2 s^{-1})	$\Phi^{\dagger}$ (S s m^{-3})	$\Phi/\Phi_{\mathrm{Naf}}{}^{\dagger}$	Ref.
44	SPF1-13	Single-layered SPEEK/PFSA/PVDF 13/37/50 wt%	H2-Br	0.62	28	—	—	—	—	[67]
45	SPF2-13	Multi-layered SPEEK/PFSA/PVDF 13/37/50 wt%	H2-Br	0.63	41	—	—	—	—	[67]
46	3M CEM	Cation-exchange membrane	VRFB	—	25/50	8.44	—	—	—	[62]
47	EBN 30	Electrospun Nafion/PVDF composite (80/20 wt%)	H2-V Fuel Cell	—	30	—	—	—	—	[68]
48	EBN 40	Electrospun Nafion/PVDF composite (80/20 wt%)	H2-V Fuel Cell	—	40	—	—	—	—	[68]
49	BPSH–BPS	Sulfonated biphenyl polysulfone copolymer	Fuel cell	1.28 meq/g	—	9.5	—	—	—	[69]
50	BisAF–BPSH	Sulfonated aromatic polymer	Fuel cell	1.6 meq/g	150	13	—	—	—	[69]
51	Nafion 117–Ce	PFSA doped with cerium	Fuel cell	0.89 mmol/g	—	—	—	—	—	[69]
52	Nafion (doped with CeO2)	PFSA doped with cerium oxide	Fuel cell	/0.84 mmol/g	35/160	8.83/17.6	—	—	—	[69]
53	SPEEK/BPO_4	SPEEK composite with borophosphate	Fuel cell	—	200	0.61	—	—	—	[69]
54	SPEEK/PSSA-g-PVDF	Composite hydrocarbon proton-exchange membrane consisting of SPEEK blended with PSSA-grafted PVDF	Fuel cell	—	50	72	—	—	—	[69]
55	AP6FSPEEK	Aminated and sulfonated poly(aryl ether ketone)	Fuel cell	1.65 mmol/g	—	8.7	—	—	—	[69]

Continued on next page…

No.	Membrane	Type / Chemistry	System	IEC (meq g^{-1})	δ (µm)	σ (S m^{-1})	P (m^2 s^{-1})	$\Phi^{\dagger}$ (S s m^{-3})	$\Phi/\Phi_{\mathrm{Naf}}{}^{\dagger}$	Ref.
56	SPEEK/NIM-SiO_2	Composite hydrocarbon proton-exchange membrane consisting of SPEEK with N-imidazole–functionalized SiO_2 inorganic filler	Fuel cell	1.73 mmol/g	110-130	22	—	—	—	[70]
57	SPAES50	Sulfonated poly(arylene ether sulfone) with 50 mol% degree of sulfonation	Fuel cell	1.89 meq/g	20	11.2	—	—	—	[69]
58	SOPBI	Sulfonated polybenzimidazole-based hydrocarbon cation-exchange membrane	VRFB	1.6 mmol/g	10	0.17 ‡	8×10^{-13}	—	0.10	[71]
59	Selemion® AMV	Anion-exchange membrane (AEM)	—	—	—	—	—	—	—	[72]
60	SPES / S-Radel®	Sulfonated poly(ether sulfone) (hydrocarbon CEM)	—	—	—	—	—	—	—	[72]
61	Composite sulfonated poly-imide/chitosan	Composite hydrocarbon CEM	—	—	—	—	—	—	—	[72]
62	Stacked NR211	PFSA	—	—	—	—	—	—	—	[73]
63	Stacked NR212	PFSA	—	—	—	—	—	—	—	[73]
64	Nafion-PEI-2.5	PFSA + polyethylenimine surface-modified CEM	VRFB	0.89 mmol/g	196	1.58 ‡	8.72×10^{-13}	—	0.82	[74]
65	Nafion-PEI-5	PFSA + PEI (thicker coating)	VRFB	0.87 mmol/g	208	1.55 ‡	2.83×10^{-13}	—	2.50	[74]
66	ZNM-5	PFSA + thin organic layer	VRFB	—	120	0.55 Ω cm^2	—	—	—	[74]
67	ZNM-15	PFSA + thin organic layer	VRFB	—	130	2.23 Ω cm^2	—	—	—	[74]

Continued on next page…

No.	Membrane	Type / Chemistry	System	IEC (meq g^{-1})	δ (µm)	σ (S m^{-1})	P (m^2 s^{-1})	$\Phi^\dagger$ (S s m^{-3})	$\Phi/\Phi_{\mathrm{Naf}}{}^\dagger$	Ref.
68	PHB12	PFSA + Polypyrrole electrodeposition	VRFB	—	—	0.783	9×10^{-13}	—	0.40	[74]
69	A9	Nafion 117 + Electrolyte soaking (9 h)	VRFB	0.733 mmol/g	—	0.33	1.70×10^{-12}	1.94×10^{11}	0.09	[74]
70	P2	Nafion 117 + Polypyrrole polymerisation via $FeCl_3$	VRFB	—	—	0.347	2.47×10^{-12}	1.40×10^{11}	0.06	[74]
71	Sulfonated Selemion AMV	AEM (Selemion AMV) + Sulfonation	VRFB	—	—	2.45 Ω cm^2	—	—	—	[74]
72	Selemion AMV (pristine)	AEM	VRFB	—	—	2.8 Ω cm^2	—	—	—	[74]
73	Modified New Selemion	Modified New Selemion + PSSS coating (2 h)	VRFB	—	—	1.25 Ω cm^2	—	—	—	[74]
74	New Selemion (Type 2)	New Selemion (Type 2)	VRFB	—	—	0.98 Ω cm^2	—	—	—	[74]
75	trPTFE/SP50	Pore-filled membrane; sulfonated poly(arylene ether ketone) (SP) impregnated into porous PTFE	VRFB	1.8 meq/g	24	0.46	7.02×10^{-13}	6.55×10^{11}	0.30	[74]
76	Porous PTFE substrate membrane (unfilled)	Porous polytetrafluo-roethylene separator	VRFB	—	—	—	3.38×10^{-12}	—	—	[74]
77	Pristine AEM (Fumasep FAP)	Pristine AEM (Fumasep FAP)	VRFB	1.16 mmol/g	60	0.55 ‡	8.73×10^{-13}	—	0.29	[74]
78	Nafion/amino-SiO_2 hybrid membrane	PFSA–amino-silica nanocomposite	VRFB	1.05 mmol/g	188	0.55 ‡	3.87×10^{-13}	—	0.64	[74]
79	Nafion/GO	Graphene-oxide modified PFSA membrane	VRFB	0.88 mmol/g	70	2.9	2×10^{-12}	—	0.66	[74]

Continued on next page…

No.	Membrane	Type / Chemistry	System	IEC (meq g^{-1})	δ (µm)	σ (S m^{-1})	P (m^2 s^{-1})	$\Phi^\dagger$ (S s m^{-3})	$\Phi/\Phi_{\mathrm{Naf}}{}^\dagger$	Ref.
80	Nafion/(WO_3) – 0.587 wt% WO_3	PFSA–WO_3 hybrid CEM	VRFB	0.8407 meq/g	—	—	9.30×10^{-12}	—	—	[74]
81	SPEEK/(WO_3) – 0.20 wt% WO_3	Sulfonated PEEK–WO_3 hybrid CEM	VRFB	1.52 meq/g	—	—	3.17×10^{-13}	—	—	[74]
82	SPEEK 43	Sulfonated poly(ether ether ketone), DS ≈ 43%	ICRFB	1.33 mmol/g	55	4.5	1.83×10^{-13}	2.46×10^{13}	1.12	[59]
83	SPEEK 47	Sulfonated poly(ether ether ketone), DS ≈ 47%	ICRFB	1.44 mmol/g	55	9.1	8.33×10^{-14}	1.09×10^{14}	4.97	[59]
84	SPEEK 52	Sulfonated poly(ether ether ketone), DS ≈ 52%	ICRFB	1.58 mmol/g	56	12.5	1.33×10^{-13}	9.40×10^{13}	4.27	[59]
85	SPEEK 57	Sulfonated poly(ether ether ketone), DS ≈ 57%	ICRFB	1.72 mmol/g	56	17.6	1.58×10^{-13}	1.11×10^{14}	5.06	[59]
86	SPEEK 62	Sulfonated poly(ether ether ketone), DS ≈ 62%	ICRFB	1.84 mmol/g	57	23	2×10^{-13}	—	5.23	[59]
87	FS-930	PFSA, CEM	VRFB	1.14 mmol/g	30	8.4	1.80×10^{-12}	4.67×10^{12}	2.12	[75]
88	DF	PFSA, CEM	VRFB	1.57 mmol/g	50	6	9.20×10^{-13}	6.52×10^{12}	2.96	[75]
89	VAN	PFSA, CEM	VRFB	—	254	0.054	1.62×10^{-11}	3.33×10^{9}	0.00	[75]
90	FAP-450	Hydrocarbon AEM	VRFB	2.18mmol/g	50	3.8	7×10^{-13}	5.43×10^{12}	2.47	[75]
91	AHA	Hydrocarbon AEM	VRFB	0.35 mmol/g	220	0.24	3.20×10^{-13}	—	0.34	[75]
92	AMV	Hydrocarbon AEM	VRFB	1.6 mmol/g	110	0.39	2.50×10^{-14}	—	7.09	[75]
93	CMV	Hydrocarbon CEM	VRFB	2.08 mmol/g	110	0.46	3.50×10^{-13}	1.31×10^{12}	0.60	[75]
94	CRIS	PFSA +Ketjen black + PVDF binder	PSIRFB	—	183	0.14 ‡	1.35×10^{-13}	—	3.37	[61]

Continued on next page…

No.	Membrane	Type / Chemistry	System	IEC (meq g^{-1})	δ (µm)	σ (S m^{-1})	P (m^2 s^{-1})	$\Phi^{\dagger}$ (S s m^{-3})	$\Phi/\Phi_{\mathrm{Naf}}{}^{\dagger}$	Ref.
95	Nafion/PP	Nafion ionomer impregnated into porous polypropylene (PP) separator	Zn-Br	—	16	70	1.26×10^{-14}	—	—	[76]
96	Neosepta AFX	Styrene-based AEM (divinylbenzene-crosslinked)	Aq soluble ORFB	1.3 meq/g	137	1.1	7.09×10^{-13}	1.55×10^{12}	23.87	[12]
97	Neosepta AHA	Styrene-based AEM	Aq soluble ORFB	1.1 meq/g	190	0.4	5.45×10^{-14}	7.34×10^{12}	112.91	[12]
98	Selemion AMV	Styrene-based AEM	Aq soluble ORFB	1.9 meq/g	104	0.46	2.21×10^{-14}	2.08×10^{13}	320.22	[12]
99	Selemion ASV	Styrene-based AEM	Aq soluble ORFB	2 meq/g	110	0.23	1.29×10^{-14}	1.78×10^{13}	274.30	[12]
100	Selemion DSV	Styrene-based AEM	Aq soluble ORFB	2.1 meq/g	93	0.8	3.74×10^{-13}	2.14×10^{12}	32.91	[12]
101	E-620	Hydrocarbon-based CEM	Aq ORFB	-	20	1.8	-	-	-	[77]
102	FS-930	PFSA-based CEM	Aq ORFB	-	30	3.2	-	-	-	[77]
103	F-1075-PK	PFSA-based CEM with PEEK reinforcement	Aq ORFB	-	75	5.4	-	-	-	[77]
104	F-1850	PFSA-based CEM	Aq ORFB	-	50	2	-	-	-	[77]
105	N-115	PFSA-based CEM	Aq ORFB	-	125	11.2	-	-	-	[77]

B

Model Parameters and Derived Quantities

B.1. Holdup Volume

The holdup volume V_R is taken as the membrane pore water volume,

$$V_R = \sigma_{\text{areal}} A \frac{\text{WU}}{\rho_{\text{water}}}, \tag{B.1}$$

where σ_{areal} is the dry membrane areal density (g cm^{-2}), WU is the equilibrium water uptake (g g^{-1}), $A = 713$ cm^2 (7.13×10^{-2} m^2) is the membrane area, and $\rho_{\text{water}} = 1.0$ g cm^{-3}. This pore volume is approximated by assuming that the absorbed water occupies the accessible pore volume of the membrane. For NR212 ($\sigma_{\text{areal}} = 0.0097$ g cm^{-2}, WU $= 0.50$ g g^{-1}), the dry membrane mass is $m_{\text{NR212}} = 713 \times 0.0097 = 6.916$ g, giving

$$V_R^{\text{NR212}} = 6.916 \times 0.50 = 3.46 \text{ cm}^3 = 3.46 \times 10^{-6} \text{ m}^3. \tag{B.2}$$

For Membrane X ($\sigma_{\text{areal}} = 0.0022$ g cm^{-2}, WU $= 0.68$ g g^{-1}), the dry membrane mass is $m_{\text{X}} = 713 \times 0.0022 = 1.569$ g, giving

$$V_R^{\text{X}} = 1.569 \times 0.68 = 1.07 \text{ cm}^3 = 1.07 \times 10^{-6} \text{ m}^3. \tag{B.3}$$

Table B.1 lists all numerical values used in the computational model described in Section 3.9. The two derived quantities requiring calculation, the membrane wet density and holdup volume V_R, are documented in Sections H and B.1 respectively.

B.2. Derivation of H-cell Fe Concentration

The exposed coupon area follows from the H-cell aperture (O-ring) diameter, $d_{\text{Hcell}} = 14.47$ mm:

$$A_{\text{Hcell}} = \pi (d_{\text{Hcell}}/2)^2 = 1.6445 \text{ cm}^2. \tag{B.4}$$

The total membrane-phase iron concentration under the H-cell electrolyte (50% SoC, $\text{Fe}_{\text{tot}} = 1.0$ mol/L, $55\,^\circ$C) follows directly from the Donnan partition coefficients already established for Membrane X (Table C.3):

$$C_{\text{Fe,R}} = K_{\text{Fe}^{2+}} c^{\text{sol}}_{\text{Fe}^{2+}} + K_{\text{Fe}^{3+}} c^{\text{sol}}_{\text{Fe}^{3+}} = (x^*)^2(0.5) + (x^*)^3(0.5) = 0.7242 + 0.8716 = 1.5958 \text{ mol/L} = 1595.8 \text{ mol/m}^3, \tag{B.5}$$

using $x^* = 1.2035$ at SoC$= 0.5$ from Table C.3. This is the concentration used directly in the k_{block} extraction (Section 3.6.2); $k_{block} = k_{obs}/C_{\text{Fe,R}}$ depends on no other quantity in this subsection.

Table B.1: Summary of all numerical parameters used in the computational model for Membrane X. Source classification: M = measured in this work; L = literature; D = derived from measured quantities; F = fitted to H-cell experimental data. Entries marked † are assumed equal to the NR211 literature value pending direct measurement.

Parameter	Symbol	Membrane X	Unit	Source
Physical constants				
Faraday constant	F	96 485	$\mathrm{C\,mol^{-1}}$	—
Ideal gas constant	R_G	8.314	$\mathrm{J\,mol^{-1}\,K^{-1}}$	—
Temperature	T	328.15	K	M
Electrolyte and operating conditions				
Total iron concentration	$c_{\mathrm{Fe,tot}}$	1000	$\mathrm{mol\,m^{-3}}$	M
Analytical H_2SO_4 concentration at SoC 0/100	$c^{\mathrm{sol}}_{H_2SO_4}$	2.5/2.0	$\mathrm{mol\,L^{-1}}$	M
Cell and reservoir geometry				
Active membrane area	A	7.13×10^{-2}	$\mathrm{m^2}$	M
Membrane thickness	δ	20	μm	M
Electrolyte tank volume	V_L	5×10^{-3}	$\mathrm{m^3}$	M
Holdup volume	V_R	1.07×10^{-6}	$\mathrm{m^3}$	D
Membrane physicochemical properties				
Ion exchange capacity	IEC	1.6	$\mathrm{meq\,g^{-1}}$	M††
Water uptake	WU	0.68	$\mathrm{g\,g^{-1}}$	M
Fixed charge concentration	c_{fix}	2.368	$\mathrm{mol\,L^{-1}}$	D
Area density	ρ_{areal}	0.0022	$\mathrm{g\,cm^{-2}}$	M
Ionic conductivity	κ	5.07–10.49	$\mathrm{S\,m^{-1}}$	L [54]
Transport parameters (effective, membrane-phase)				
Fe^{2+} diffusivity	$D_{\mathrm{Fe^{2+}}}$	1.7×10^{-10}†	$\mathrm{m^2\,s^{-1}}$	L [49]
Fe^{3+} diffusivity	$D_{\mathrm{Fe^{3+}}}$	1.428×10^{-10}†	$\mathrm{m^2\,s^{-1}}$	L [49], [50]‡
Fouling submodel				
Initial cell resistance	R_0	calibrated from data	Ω	M
Max. resistance increment	$\Delta R_{\max}$	calibrated from data	Ω	M
Blocking rate constant	k_{block}	1.162×10^{-9}	$\mathrm{m^3 mol^{-1}\,s^{-1}}$	F

† No membrane-specific measurement available; assumed equal to the NR211 literature value as a first-order approximation.

‡ Coms & LaLonde [49] directly measure $D_{\mathrm{Fe^{2+}}}$ in Nafion NR211 at $50\,^{\circ}\mathrm{C}$. $D_{\mathrm{Fe^{3+}}}$ is estimated by scaling $D_{\mathrm{Fe^{2+}}}$ by the ratio of limiting aqueous diffusivities $D^{\mathrm{aq}}_{\mathrm{Fe^{3+}}}/D^{\mathrm{aq}}_{\mathrm{Fe^{2+}}}$

†† Measured at Elestor B.V. prior to the commencement of this project

C

Ideal Donnan Equilibrium

For each membrane, the fixed-charge concentration is obtained from the ion-exchange capacity and water uptake,

$$c_{\mathrm{fix}} = \frac{\mathrm{IEC}}{\mathrm{WU}}. \tag{C.1}$$

The bulk electrolyte composition is common to all three membranes. The total analytical iron concentration is held at $1.0\ \mathrm{mol\,L^{-1}}$, while the analytical sulfuric-acid concentration decreases from $2.5\ \mathrm{mol\,L^{-1}}$ at SoC $= 0$ to $2.0\ \mathrm{mol\,L^{-1}}$ at SoC $= 1$. For a fractional state of charge s,

$$c^{\mathrm{sol}}_{\mathrm{Fe^{2+}}} = 1 - s, \quad c^{\mathrm{sol}}_{\mathrm{Fe^{3+}}} = s, \quad C_{\mathrm{H_2SO_4}} = 2.5 - 0.5s, \tag{C.2}$$

with all concentrations in $\mathrm{mol\,L^{-1}}$. The total analytical sulfate concentration,

$$S_{\mathrm{T}} = C_{\mathrm{H_2SO_4}} + c^{\mathrm{sol}}_{\mathrm{Fe^{2+}}} + \tfrac{3}{2} c^{\mathrm{sol}}_{\mathrm{Fe^{3+}}}, \tag{C.3}$$

is constant at $3.5\ \mathrm{mol\,L^{-1}}$ across the full operating range, independent of SoC.

Because the second dissociation of sulfuric acid is incomplete, the bulk electrolyte speciation is obtained from

$$\mathrm{HSO_4^-} \rightleftharpoons \mathrm{H^+} + \mathrm{SO_4^{2-}}, \qquad K_{a,2} = \frac{c^{\mathrm{sol}}_{\mathrm{H^+}}\, c^{\mathrm{sol}}_{\mathrm{SO_4^{2-}}}}{c^{\mathrm{sol}}_{\mathrm{HSO_4^-}}}, \tag{C.4}$$

with $K_{a,2} = 4.0836 \times 10^{-3}$ at $55\,^{\circ}\mathrm{C}$ [78], [79], together with the mass balances $c^{\mathrm{sol}}_{\mathrm{H^+}} + c^{\mathrm{sol}}_{\mathrm{HSO_4^-}} = 2C_{\mathrm{H_2SO_4}}$ and $c^{\mathrm{sol}}_{\mathrm{HSO_4^-}} + c^{\mathrm{sol}}_{\mathrm{SO_4^{2-}}} = S_{\mathrm{T}}$. The thermodynamic second dissociation constant of sulfuric acid was evaluated at $T = 328.15\ \mathrm{K}$ using the temperature correlation reported by Christov and Moller, which is based on the bisulfate dissociation model of Dickson et al. [78], [79]. In the present ideal treatment, activities are approximated by concentrations. Since these relations depend only on the bulk electrolyte and not on the membrane itself, the resulting bulk speciation (Table C.1) is identical for all three membranes at a given SoC.

Table C.1: Bulk electrolyte speciation, common to all three membranes, at SoC $= 0$, 0.5, and 1. All concentrations in $\mathrm{mol\,L^{-1}}$.

SoC	$c^{\mathrm{sol}}_{\mathrm{H^+}}$	$c^{\mathrm{sol}}_{\mathrm{HSO_4^-}}$	$c^{\mathrm{sol}}_{\mathrm{SO_4^{2-}}}$
0	1.50944	3.49056	0.00944
0.5	1.01404	3.48596	0.01404
1	0.52692	3.47308	0.02692

The Donnan parameter $x = \exp(-F\phi_D/RT)$ satisfies the ideal electroneutrality condition

$$c^{\mathrm{sol}}_{\mathrm{H^+}} x + 2c^{\mathrm{sol}}_{\mathrm{Fe^{2+}}} x^2 + 3c^{\mathrm{sol}}_{\mathrm{Fe^{3+}}} x^3 - c^{\mathrm{sol}}_{\mathrm{HSO_4^-}} x^{-1} - 2c^{\mathrm{sol}}_{\mathrm{SO_4^{2-}}} x^{-2} = c_{\mathrm{fix}}, \tag{C.5}$$

solved numerically for the physical positive root x^* at each SoC, using the membrane-specific c_{fix} from Eq. (C.1). The full electroneutrality expression, retaining both counter-ion and co-ion contributions, is solved directly rather than invoking the total co-ion exclusion approximation, which is only accurate when the membrane fixed-charge concentration substantially exceeds the bathing electrolyte concentration [51], a condition not clearly satisfied here given c_{fix} is comparable in magnitude to S_{T}. The partition coefficient of species i is $K_i = (x^*)^{z_i}$, the Donnan potential is $\phi_D = -(RT/F)\ln x^*$, and membrane-phase concentrations follow as $c_i^{\mathrm{mem}} = K_i\, c_i^{\mathrm{sol}}$.

Nafion NR212

$$c_{\mathrm{fix}}^{\mathrm{NR212}} = \frac{0.98}{0.50} = 1.96\ \mathrm{mol\,L^{-1}}. \tag{C.6}$$

Table C.2: Ideal Donnan equilibrium results for Nafion NR212 ($c_{\mathrm{fix}} = 1.96\ \mathrm{mol\,L^{-1}}$). All concentrations in $\mathrm{mol\,L^{-1}}$.

SoC	x^*	ϕ_D (mV)	$c_{\mathrm{H^+}}^{\mathrm{mem}}$	$c_{\mathrm{Fe^{2+}}}^{\mathrm{mem}}$	$c_{\mathrm{Fe^{3+}}}^{\mathrm{mem}}$	$c_{\mathrm{HSO_4^-}}^{\mathrm{mem}}$	$c_{\mathrm{SO_4^{2-}}}^{\mathrm{mem}}$
0	1.22177	−5.66	1.84419	1.49272	0	2.85697	0.00633
0.5	1.17018	−4.44	1.18661	0.68466	0.80118	2.97899	0.01025
1	1.14018	−3.71	0.60078	0	1.48224	3.04609	0.02070

Same-composition ratio at SoC $= 0.5$: $K_{\mathrm{Fe^{2+}}}/K_{\mathrm{Fe^{3+}}} = 1/x^* = 0.8546$.
Cross-endpoint ratio: $K_{\mathrm{Fe^{2+}}}(\mathrm{SoC{=}0})/K_{\mathrm{Fe^{3+}}}(\mathrm{SoC{=}1}) = 1.49272/1.48224 = 1.007$.

Membrane X

$$c_{\mathrm{fix}}^{\mathrm{X}} = \frac{1.61}{0.6798} = 2.368\ \mathrm{mol\,L^{-1}}. \tag{C.7}$$

Table C.3: Ideal Donnan equilibrium results for Membrane X ($c_{\mathrm{fix}} = 2.368\ \mathrm{mol\,L^{-1}}$). All concentrations in $\mathrm{mol\,L^{-1}}$.

SoC	x^*	ϕ_D (mV)	$c_{\mathrm{H^+}}^{\mathrm{mem}}$	$c_{\mathrm{Fe^{2+}}}^{\mathrm{mem}}$	$c_{\mathrm{Fe^{3+}}}^{\mathrm{mem}}$	$c_{\mathrm{HSO_4^-}}^{\mathrm{mem}}$	$c_{\mathrm{SO_4^{2-}}}^{\mathrm{mem}}$
0	1.2684	−6.72	1.9146	1.6088	0	2.7512	0.00587
0.5	1.2035	−5.24	1.2204	0.7242	0.8716	2.8965	0.00969
1	1.1671	−4.37	0.6150	0	1.5897	2.9756	0.01976

Same-composition ratio at SoC $= 0.5$: $K_{\mathrm{Fe^{2+}}}/K_{\mathrm{Fe^{3+}}} = 1/x^* = 0.831$.
Cross-endpoint ratio: $K_{\mathrm{Fe^{2+}}}(\mathrm{SoC{=}0})/K_{\mathrm{Fe^{3+}}}(\mathrm{SoC{=}1}) = 1.6088/1.5897 = 1.012$.

CMVN

$$c_{\mathrm{fix}}^{\mathrm{CMVN}} = \frac{1.4676}{0.2788} = 5.264\ \mathrm{mol\,L^{-1}}. \tag{C.8}$$

Table C.4: Ideal Donnan equilibrium results for CMVN ($c_{\mathrm{fix}} = 5.264\ \mathrm{mol\,L^{-1}}$). All concentrations in $\mathrm{mol\,L^{-1}}$.

SoC	x^*	ϕ_D (mV)	$c_{\mathrm{H^+}}^{\mathrm{mem}}$	$c_{\mathrm{Fe^{2+}}}^{\mathrm{mem}}$	$c_{\mathrm{Fe^{3+}}}^{\mathrm{mem}}$	$c_{\mathrm{HSO_4^-}}^{\mathrm{mem}}$	$c_{\mathrm{SO_4^{2-}}}^{\mathrm{mem}}$
0	1.5912	−13.13	2.4018	2.5319	0	2.1939	0.00373
0.5	1.4187	−9.89	1.4386	1.0064	1.4277	2.4572	0.00698
1	1.3379	−8.23	0.7050	0	2.3948	2.5959	0.01504

Same-composition ratio at SoC $= 0.5$: $K_{\mathrm{Fe^{2+}}}/K_{\mathrm{Fe^{3+}}} = 1/x^* = 0.705$.
Cross-endpoint ratio: $K_{\mathrm{Fe^{2+}}}(\mathrm{SoC{=}0})/K_{\mathrm{Fe^{3+}}}(\mathrm{SoC{=}1}) = 2.5319/2.3948 = 1.057$.

Comparison across membranes

Table C.5: Fixed-charge concentration and cross-endpoint Fe^{2+}/Fe^{3+} partition ratio for all three membranes, ideal Donnan model.

Membrane	c_{fix} (mol L^{-1})	Cross-endpoint ratio
NR212	1.96	1.007
Membrane X	2.368	1.012
CMVN	5.264	1.057

All three membranes are predicted, under the ideal Donnan framework, to show only a small difference in electrostatic partitioning between Fe^{2+} and Fe^{3+}, regardless of the substantial spread in c_{fix} across membranes.

D

Evaluation of Resistance Measurement Techniques for In-Situ Stack Testing

Accurate and non-invasive measurement of the total ohmic resistance of an operating Fe–H_2 cell stack is central to tracking membrane degradation over time. Two standard electrochemical techniques were evaluated for this purpose prior to the long-term cycling experiments: galvanostatic polarisation and electrochemical impedance spectroscopy (EIS). Both were applied to the cell stack with Nafion NR212 as the membrane, with the objective of establishing a reliable baseline resistance measurement protocol. As described below, each technique yielded internally consistent results but proved impractical for repeated in-situ monitoring for different reasons. The method ultimately adopted for resistance tracking during long-term cycling is described in Section 3.2.6.

D.1. Galvanostatic Polarisation

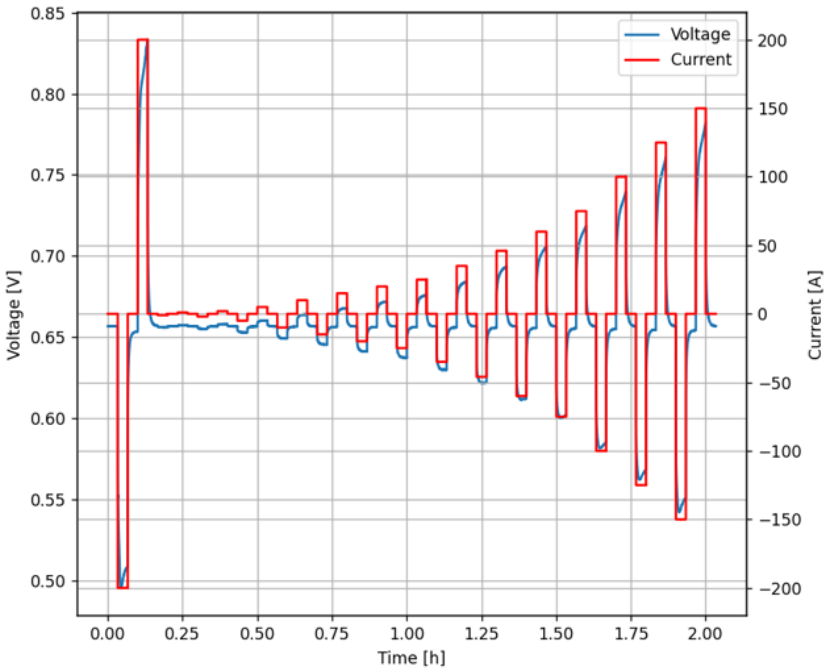


Figure D.1: Polarization test plan

The cell was first subjected to a constant-current constant-voltage (CCCV) charge–discharge cycle to determine the usable capacity. It was then charged to SoC $= 50\%$ to ensure a well-defined and reproducible operating point. The polarisation sequence consisted of repeated current pulses applied symmetrically about this SoC: the cell was held at open-circuit voltage (OCV) for 2 minutes, discharged at a fixed current for 2 minutes, returned to OCV for 2 minutes, and then charged at the same current magnitude for 2 minutes. This four-step sequence was repeated at incrementally higher current magnitudes, stepping the applied current from low values up to the maximum safe operating current of the stack. The full test occupied approximately 2–3 hours of cell time. The voltage and current plots shown in Figure D.1

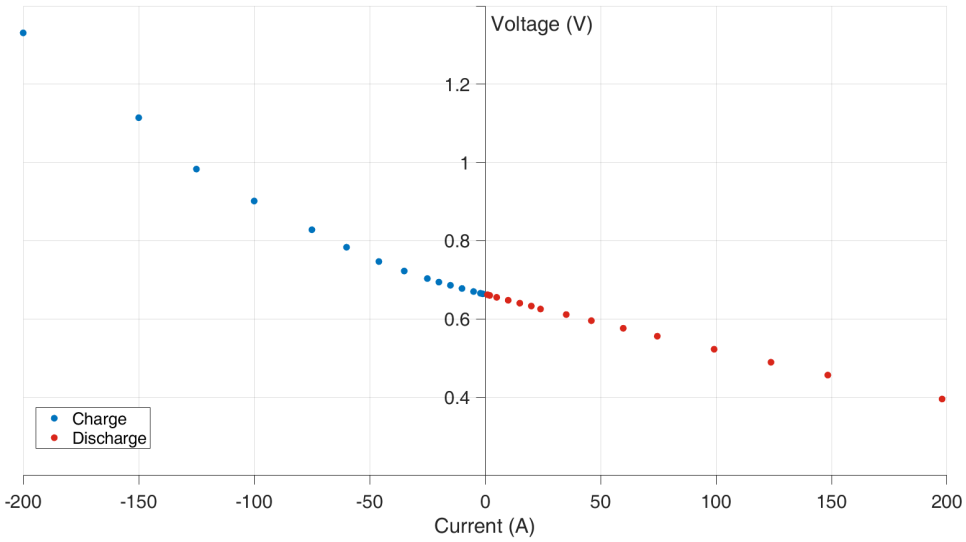


Figure D.2: Voltage versus current plot from polarization

The stabilized voltage response at each current step was recorded at steady state and plotted against current to produce a polarisation curve as shown in Figure D.2. A linear fit to the ohmic region of the V–I curve yields the total ohmic resistance of the cell as the slope of the fit. For Nafion NR212, the polarisation measurement yielded:

$$R_{\mathrm{pol,charge}} = 1.8\ \mathrm{m\Omega}, \qquad R_{\mathrm{pol,discharge}} = 1.4\ \mathrm{m\Omega}$$

confirming a strongly ohmic response in the operating current range, visible in Figure D.3 . The asymmetry between charge and discharge resistance is consistent with the direction-dependent ionic transport through the membrane and electrode kinetics at the two half-cells.

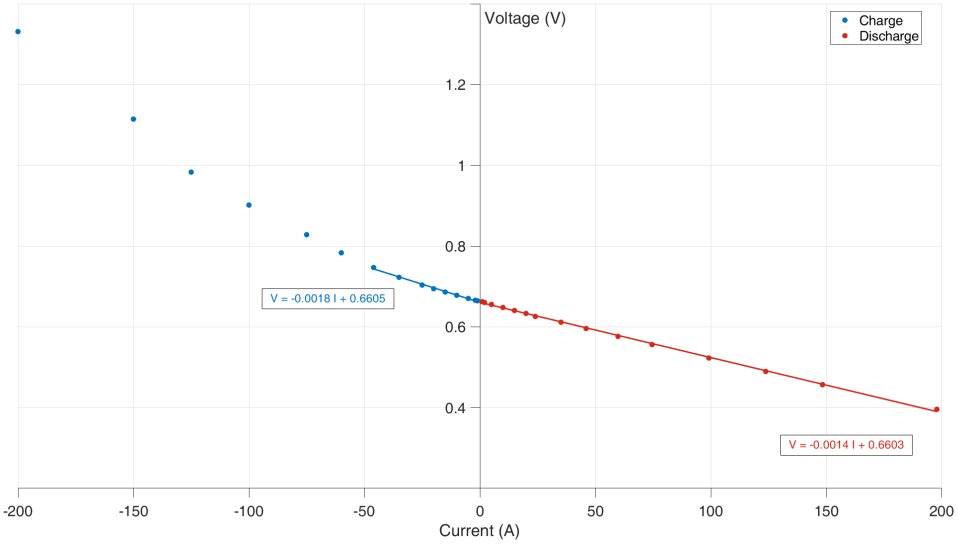


Figure D.3: Linear region of polarization

Despite the resistance being close to the value obtained from EIS, the polarisation method is unsuitable as a routine resistance tracking tool for a few reasons. First, each measurement requires the cell to be driven across a wide range of current densities, from near-zero up to the maximum operating current. The resulting repeated electrochemical cycling of the electrolyte and the associated current-induced degradation of the membrane-electrode interface means that each polarisation test constitutes an accelerated ageing event. Performing such a test after every charge–discharge cycle would systematically distort the membrane degradation trajectory that the measurement is intended to characterise. Second, the test duration of approximately 2–3 hours per measurement is prohibitively long relative to the typical cycle period of the stack, making it impractical to acquire resistance data with sufficient temporal resolution to track gradual resistance evolution.

D.2. Electrochemical Impedance Spectroscopy

EIS measurements were performed using a Bio-Logic VMP3 potentiostat/galvanostat at SoC $= 50\%$ with the cell at OCV. A sinusoidal voltage perturbation of 10 mV amplitude was applied over a frequency range of 1 MHz to 100 mHz, with three repetitions collected per frequency point. The resulting Nyquist spectrum was fitted to an equivalent circuit of the form $R_1 + Q_2/R_2$, comprising an ohmic resistance R_1 in series with a constant-phase element Q_2 in parallel with a charge-transfer resistance R_2. This circuit corresponds to the impedance expression:

$$Z(f) = R_1 + \frac{R_2}{R_2 Q_2 (2\pi f)^{a_2} + 1} \tag{D.1}$$

where f is frequency, Q_2 is the CPE magnitude, and a_2 is the CPE exponent ($0 < a_2 \leq 1$, with $a_2 = 1$ recovering ideal capacitive behaviour). The ohmic resistance R_1 is read directly from the high-frequency real-axis intercept of the Nyquist plot, and the charge-transfer resistance R_2 is recovered from the diameter of the depressed semicircle. For Nafion NR212, five consecutive EIS spectra, shown in Figure D.4, were acquired to assess reproducibility.

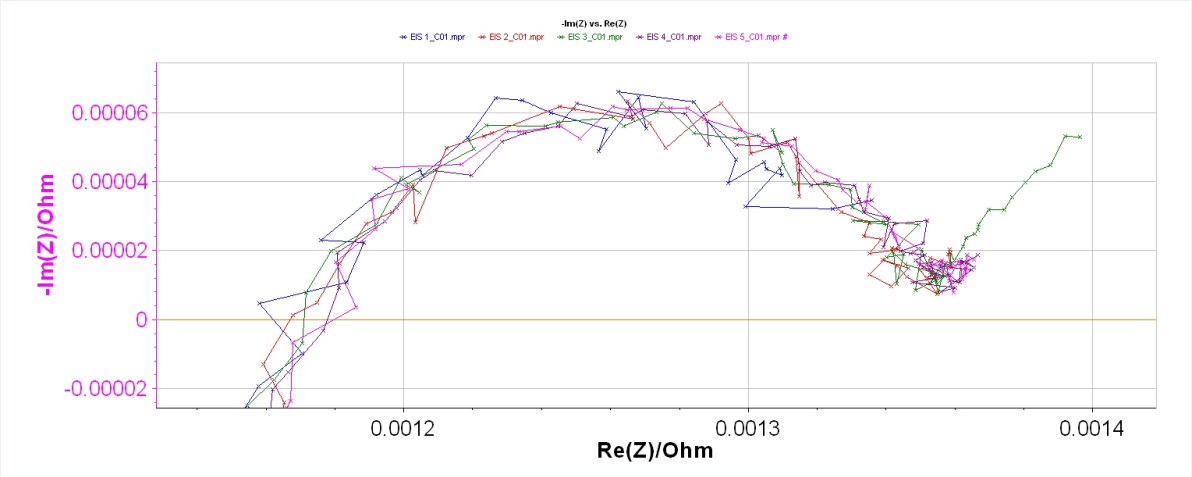


Figure D.4: EIS measuremnts for NR212

Each of the five spectra was individually fitted in ZFit using the same equivalent circuit, $L_1 + R_1 + (R_2/Q_2)$, shown in Figures D.5–D.9. In each figure, the green markers denote the real-axis intercepts used to extract R_1 (high frequency) and $R_1 + R_2$ (low frequency). The red curve in each figure represents the fitted curve. Averaged across the five fits, this yielded $R_1 = 1.172$ mΩ and $R_2 = 0.152$ mΩ, giving a total modelled impedance of $R_{\text{tot}} = 1.324$ mΩ. These values are in good agreement with the polarisation result.

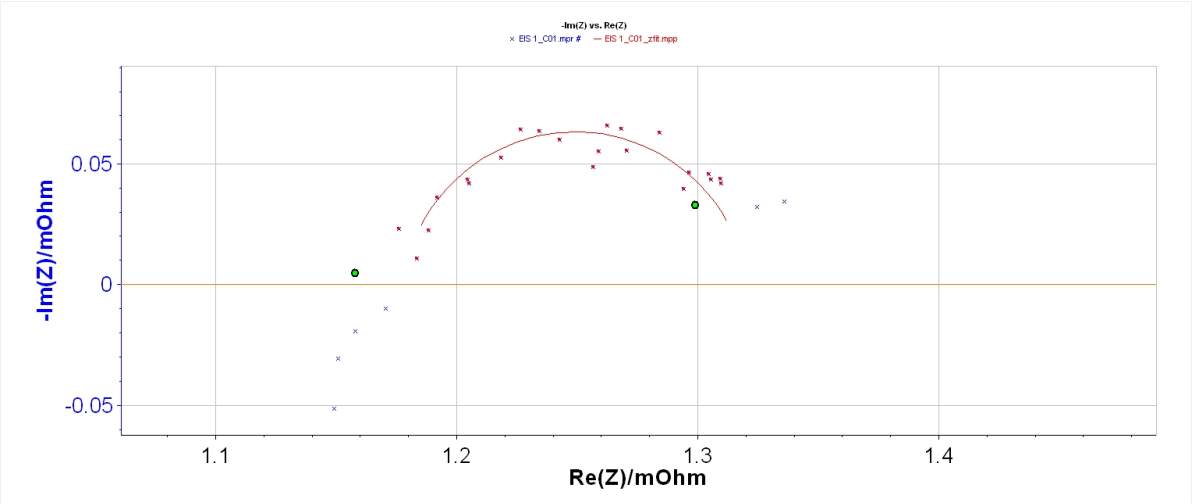


Figure D.5: Equivalent circuit fit for NR212, Spectrum 1.

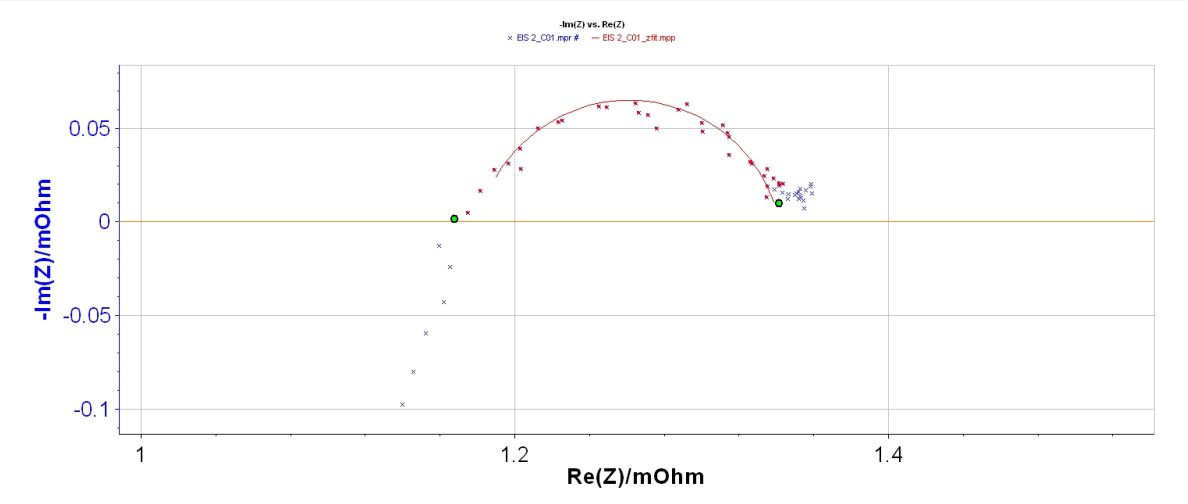


Figure D.6: Equivalent circuit fit for NR212, Spectrum 2.

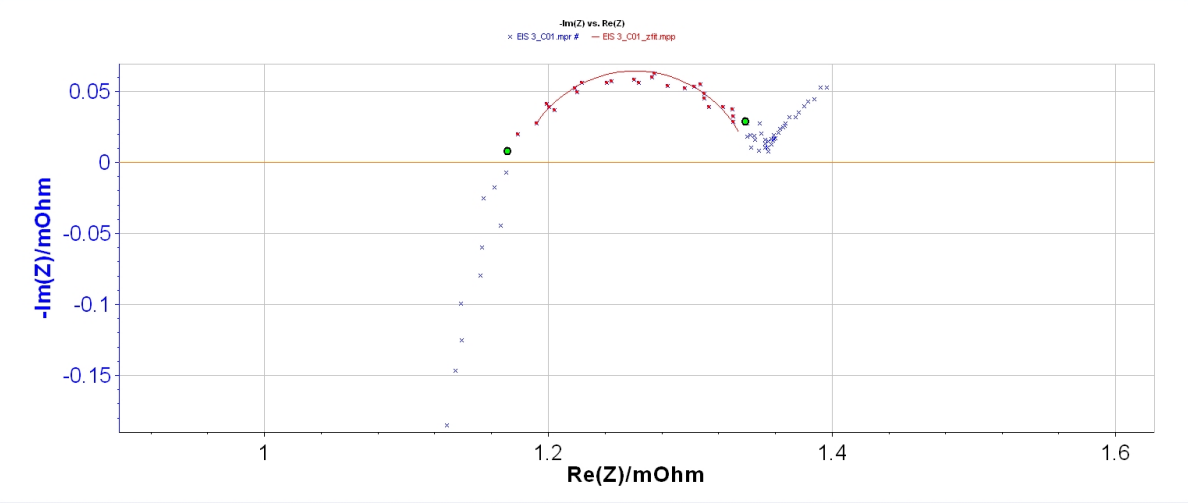


Figure D.7: Equivalent circuit fit for NR212, Spectrum 3.

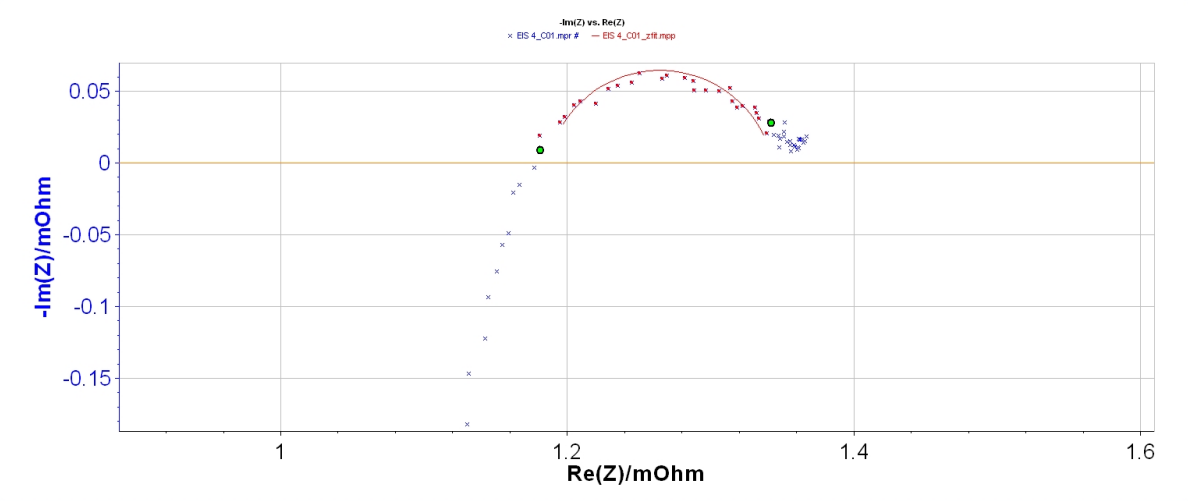


Figure D.8: Equivalent circuit fit for NR212, Spectrum 4.

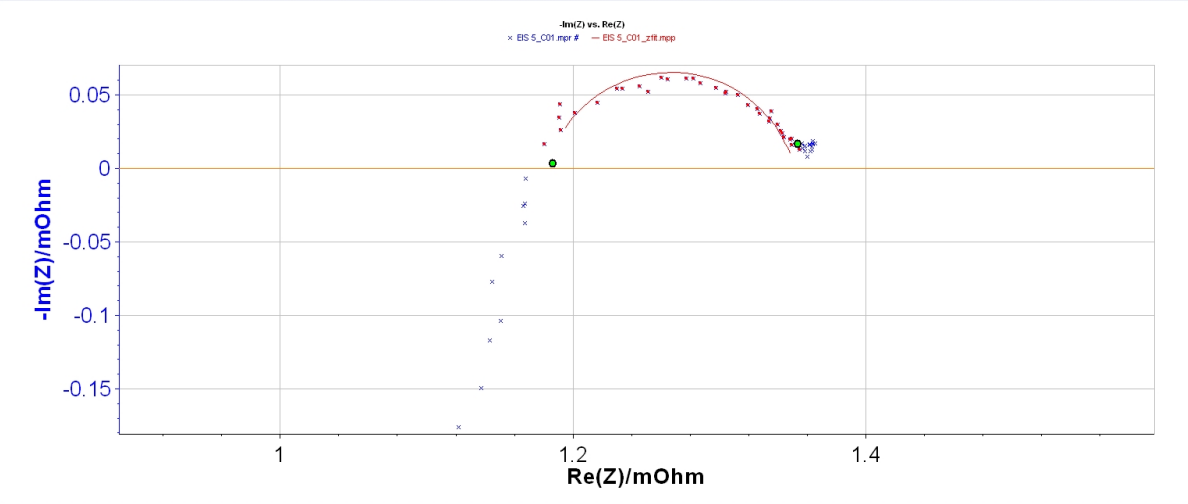


Figure D.9: Equivalent circuit fit for NR212, Spectrum 5.

Although EIS provides a physically richer decomposition of the impedance than polarisation, separating ohmic from charge-transfer contributions, it suffers from two significant practical limitations in large-format RFB cell stacks. First, the presence of inductive artefacts at high frequencies, arising from the large cell geometry and current-carrying cables, distorts the Nyquist spectrum and can compromise the high-frequency intercept determination. These inductive effects are well-documented in large-scale RFB systems and were observed to render individual spectra unreliable; only by averaging multiple spectra and filtering the inductive tail could a stable R_1 be extracted. Repeated acquisitions on the same stack, under nominally identical conditions, frequently produced qualitatively different spectra, ranging from erratic, self-intersecting traces to anomalous large-amplitude excursions with no resolvable interfacial arc, indicating that individual in-stack EIS measurements were neither reliable nor reproducible in this configuration. Multiple failed attempts to perform EIS measurements were encountered before having success, examples of which are depicted in Figures D.10–D.15. Second, and more critically for routine monitoring, sometimes, a single EIS acquisition covering the full frequency range from 1 MHz to 100 mHz required more than a day of measurement time at the required number of repetitions per frequency point. This makes EIS fundamentally incompatible with the requirement of measuring resistance at the end of each charge–discharge cycle, which typically spans only a few hours.

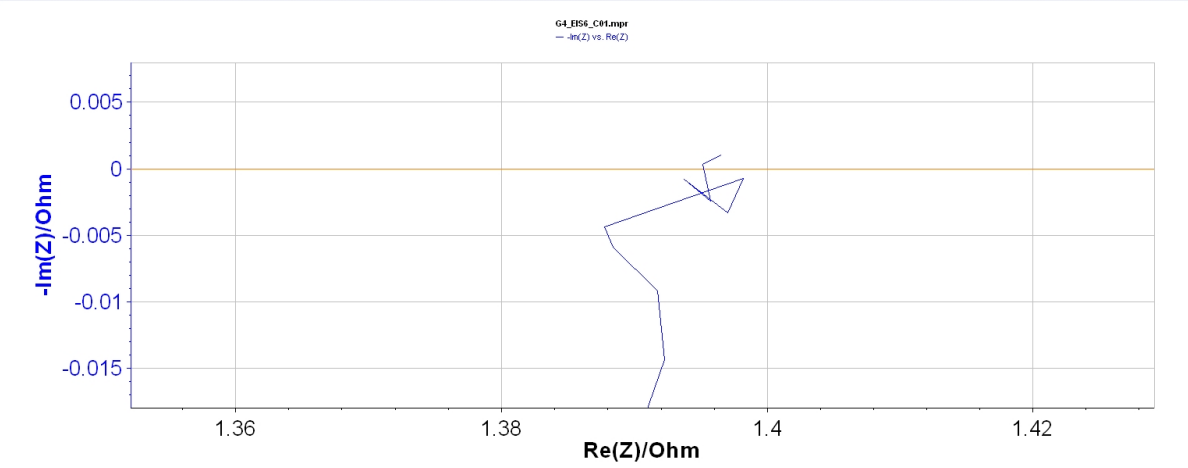


Figure D.10: Erratic, self-intersecting trace with no resolvable arc.

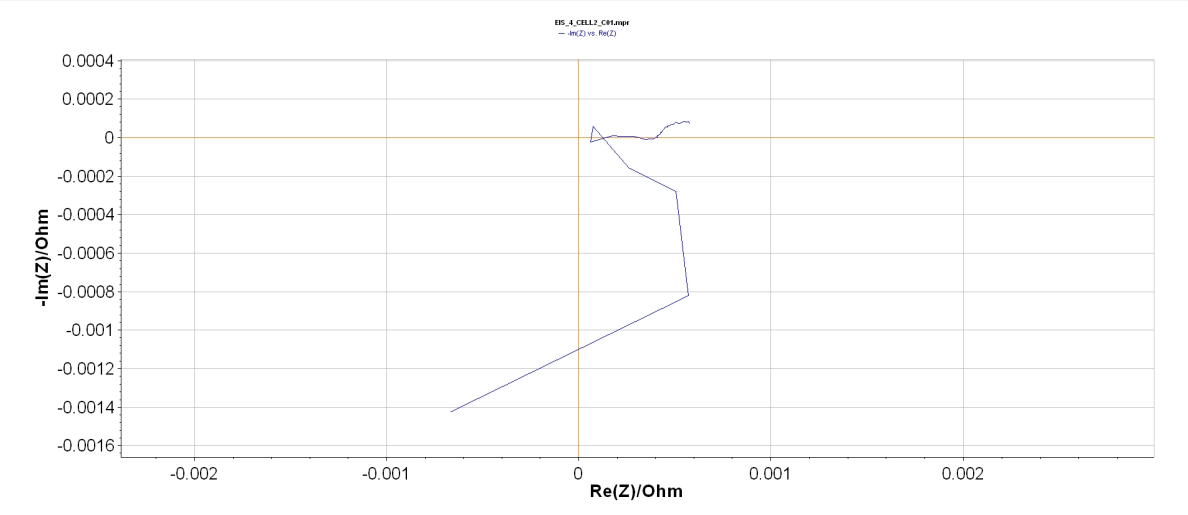


Figure D.11: Small axis-crossing loop followed by an anomalous excursion.

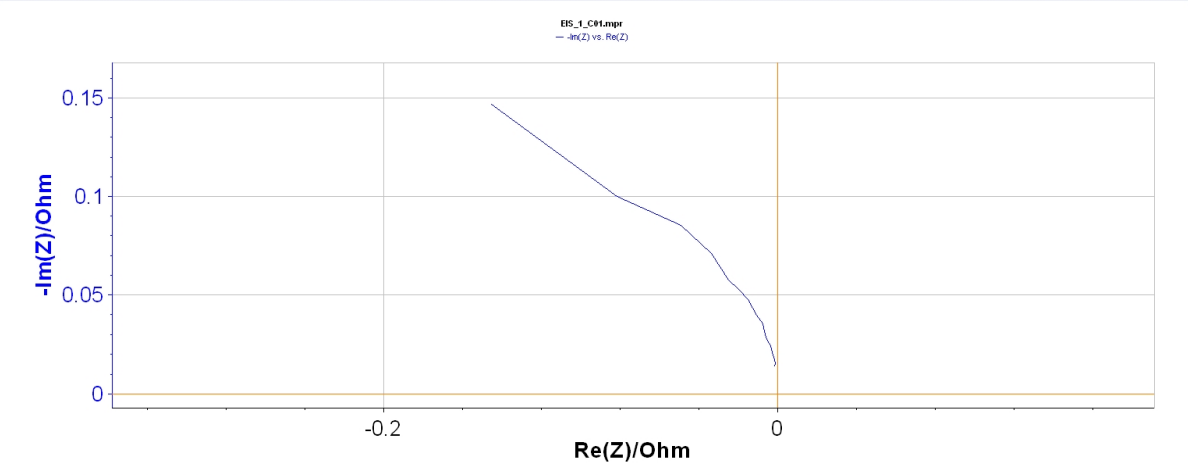


Figure D.12: Monotonically declining trace, no discernible capacitive arc.

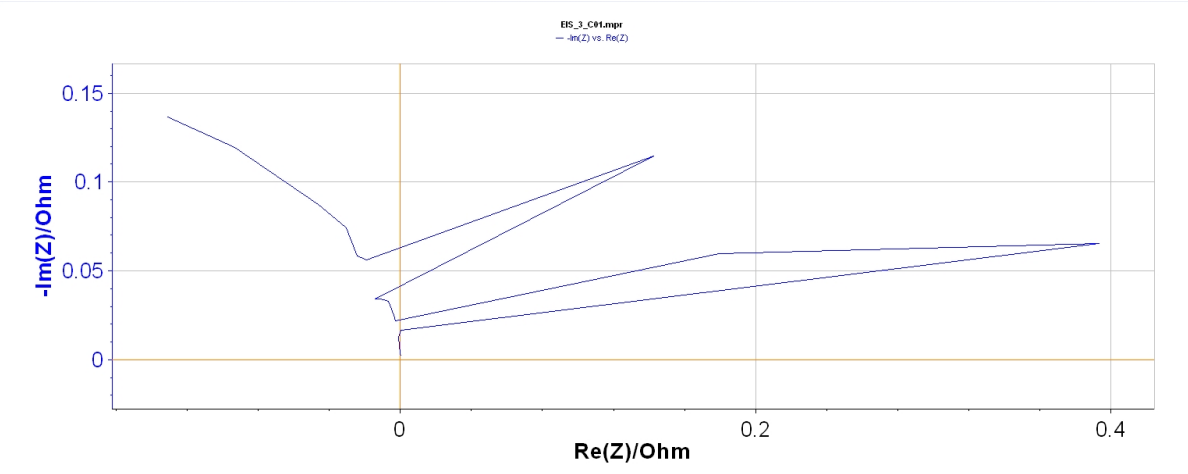


Figure D.13: Overlapping, self-crossing loops indicative of drift during acquisition.

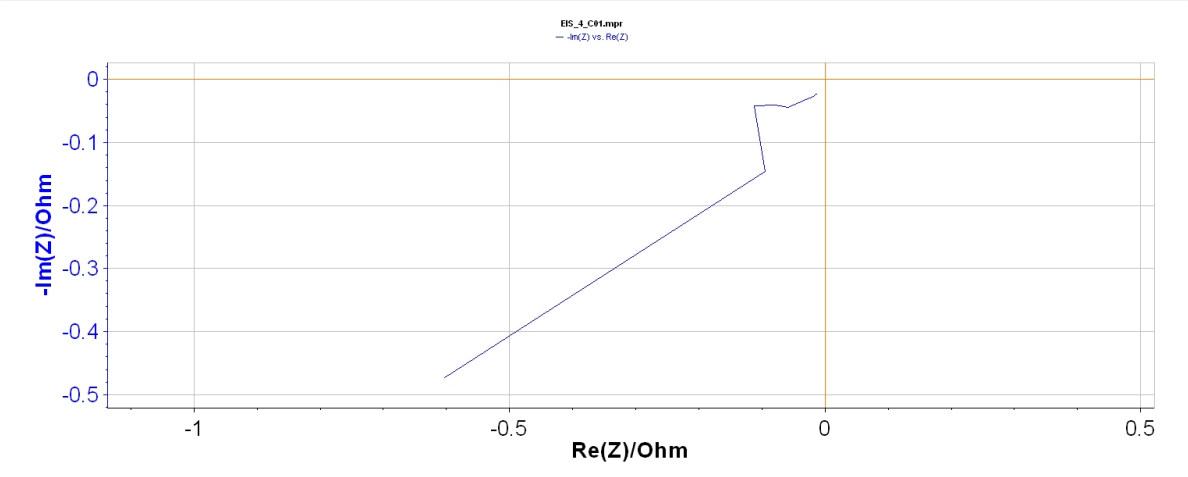


Figure D.14: Large-amplitude excursion dominating the spectrum.

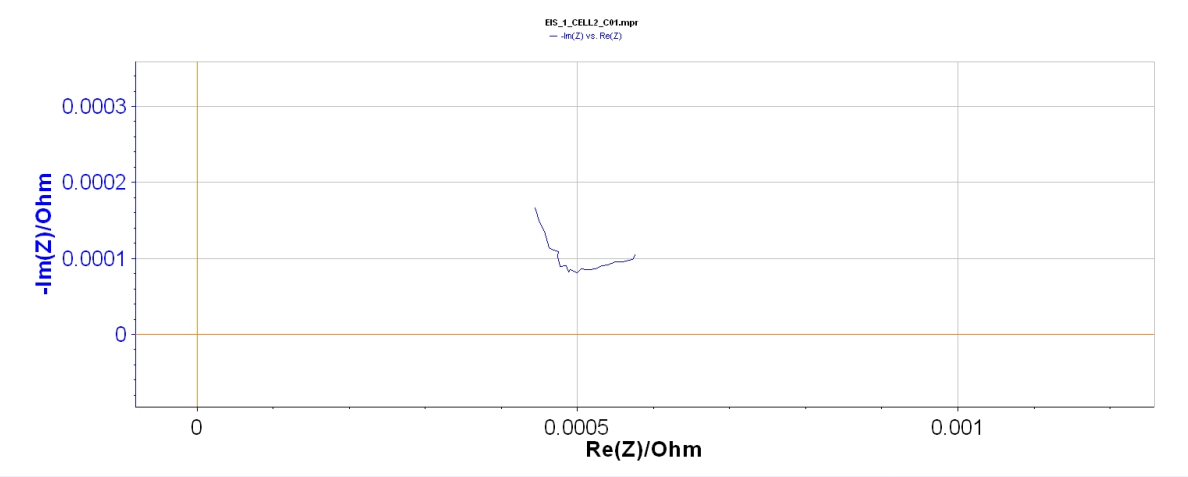


Figure D.15: Near-featureless trace confined to an anomalously narrow impedance range.

D.3. Summary and Conclusion

The polarisation and EIS measurements are in mutual agreement and confirm that the ohmic resistance of the NR212 cell is approximately 1.4–1.8 mΩ under operating conditions, with the charge-transfer contribution adding a further $\sim$0.15 mΩ. The cross-validation of the two independent techniques confirms that both are accurate. However, neither is suitable as a routine in-situ monitoring tool: polarisation causes incremental membrane ageing and requires 2–3 hours per test, while EIS suffers from inductive artefacts and requires more than one day per measurement. Table D.1 summarises the key characteristics of each technique.

Table D.1: Comparison of resistance measurement techniques evaluated for in-situ stack monitoring.

Method	Result (NR212)	Limitation	Suitable for routine monitoring?
Polarisation	$R = 1.4$ mΩ (discharge), 1.8 mΩ (charge); $R^2 = 0.999$	Incremental membrane ageing per test; 2–3 h per measurement	No
EIS	$R_{\text{ohmic}} = 1.172$ mΩ; $R_{\text{CT}} = 0.152$ mΩ	Inductive artefacts at high frequency; >24 h per measurement	No

These findings motivated the adoption of an alternative resistance extraction approach based on the

instantaneous voltage step at the onset of each galvanostatic half-cycle, which is described in Section 3.2.6.

E

MATLAB Code for model

The complete MATLAB implementation of the resistance model is publicly available at https://github.com/rishab-247/MATLAB-code---resistance-model.

F

Iron-Cation Interference in NaOH Titration of NaCl Extracts

The conventional ion-exchange-capacity (IEC) procedure for a proton-form cation-exchange membrane involves displacement of membrane-associated protons by $\mathrm{Na^+}$, followed by titration of the released acid with NaOH. The calculation assumes that the hydroxide consumed at the selected endpoint originates exclusively from membrane-derived proton equivalents.

This assumption is not valid when the NaCl extract contains dissolved iron. Ferric iron consumes hydroxide through hydrolysis and precipitation, while ferrous-iron-containing solutions exhibit a handling-dependent titration response. Consequently, the NaOH endpoint cannot be converted uniquely into either membrane IEC or retained-iron content without an independent determination of the iron concentration and chemical state.

Dummy solutions of known composition were therefore titrated to determine whether a reproducible correction could be applied. The purpose of these tests was to evaluate whether NaOH titration remained selective for proton equivalents in the presence of iron.

F.1. Dummy-Solution Preparation

Separate $250\ \mathrm{mL}$ dummy solutions were prepared in a common matrix containing

- $14.61\ \mathrm{g}$ NaCl, corresponding to $1.000\ \mathrm{mol\,L^{-1}}$;
- $34.667\ \mathrm{mg}$ pure-$\mathrm{H_2SO_4}$ equivalent;
- either ferrous or ferric sulfate at the concentration specified below.

The ferrous dummy solutions each contained $165\ \mathrm{mg}\ \mathrm{FeSO_4 \cdot 7H_2O}$. Two nominally identical ferrous solutions were used to compare stirred and unstirred handling conditions. The standard ferric solution contained $145\ \mathrm{mg}\ \mathrm{Fe_2(SO_4)_3 \cdot 5H_2O}$, while a second ferric solution contained $290\ \mathrm{mg}$, corresponding to twice the ferric concentration.

All measurements were performed using $15\ \mathrm{mL}$ aliquots and $0.0200\ \mathrm{mol\,L^{-1}}$ NaOH. The common sulfuric-acid contribution was calculated from

$$n_{\mathrm{H_2SO_4},250} = \frac{0.034667}{98.08} = 0.353456\ \mathrm{mmol}. \tag{F.1}$$

Complete neutralisation requires two hydroxide equivalents per mole of sulfuric acid:

$$\mathrm{H_2SO_4 + 2OH^- \longrightarrow SO_4^{2-} + 2H_2O}. \tag{F.2}$$

The formal acid-equivalent content in a $15\ \mathrm{mL}$ aliquot was therefore

$$n_{\mathrm{acid},15} = 2(0.353456)\frac{15}{250} = 0.042415\ \mathrm{mmol}. \tag{F.3}$$

At the stated NaOH concentration, this corresponds to

$$V_{\mathrm{acid}} = \frac{0.042415\ \mathrm{mmol}}{0.0200\ \mathrm{mmol\,mL^{-1}}} = 2.1207\ \mathrm{mL}. \tag{F.4}$$

This acid contribution was subtracted from the total NaOH consumption of each iron-containing dummy solution.

The iron contents of the $15\ \mathrm{mL}$ aliquots were

$$n_{\mathrm{Fe^{2+}}} = \frac{0.165}{278.01}\frac{15}{250} = 0.035610\ \mathrm{mmol}, \tag{F.5}$$

$$n_{\mathrm{Fe^{3+},standard}} = 2\frac{0.145}{489.95}\frac{15}{250} = 0.035514\ \mathrm{mmol}, \tag{F.6}$$

$$n_{\mathrm{Fe^{3+},double}} = 2\frac{0.290}{489.95}\frac{15}{250} = 0.071028\ \mathrm{mmol}. \tag{F.7}$$

F.2. Ferric-Iron Interference

Upon addition of NaOH, ferric iron undergoes hydrolysis and precipitation. The net reaction for complete precipitation can be represented as

$$\mathrm{Fe^{3+}} + 3\mathrm{OH^-} \longrightarrow \mathrm{Fe(OH)_3(s)}. \tag{F.8}$$

Hydroxide consumed by this reaction is not distinguishable from hydroxide used to neutralise membrane-derived acid.

For the standard ferric solution, the endpoint was $7.4463\ \mathrm{mL}$, corresponding to

$$n_{\mathrm{NaOH,total}} = 7.4463(0.0200) = 0.148926\ \mathrm{mmol}. \tag{F.9}$$

After subtraction of the acid contribution,

$$n_{\mathrm{NaOH,Fe^{3+}}} = 0.148926 - 0.042415 = 0.106511\ \mathrm{mmol}. \tag{F.10}$$

The apparent hydroxide consumption per mole of ferric iron was therefore

$$\nu_{\mathrm{Fe^{3+}}} = \frac{0.106511}{0.035514} = 2.999 \approx 3.00\ \mathrm{mol\,OH^-\ mol^{-1}\,Fe^{3+}}. \tag{F.11}$$

For the doubled ferric concentration, the endpoint was $12.0847\ \mathrm{mL}$:

$$n_{\mathrm{NaOH,total}} = 12.0847(0.0200) = 0.241694\ \mathrm{mmol}, \tag{F.12}$$

$$n_{\mathrm{NaOH,Fe^{3+}}} = 0.241694 - 0.042415 = 0.199279\ \mathrm{mmol}, \tag{F.13}$$

$$\nu_{\mathrm{Fe^{3+}}} = \frac{0.199279}{0.071028} = 2.806\ \mathrm{mol\,OH^-\ mol^{-1}\,Fe^{3+}}. \tag{F.14}$$

The standard-concentration result is essentially identical to the three-equivalent consumption expected for $\mathrm{Fe(OH)_3}$ precipitation. Doubling the ferric content increased the iron-associated NaOH consumption from 0.1065 to $0.1993\ \mathrm{mmol}$, confirming that the endpoint interference is strongly dependent on the ferric-iron content. The increase was not perfectly proportional, indicating that a single fixed blank correction or universal stoichiometric correction would not describe all concentrations under the tested conditions.

F.3. Ferrous-Iron and Handling-Dependent Interference

Ferrous iron can consume hydroxide through precipitation as ferrous hydroxide,

$$\mathrm{Fe}^{2+} + 2\mathrm{OH}^- \longrightarrow \mathrm{Fe(OH)_2(s)}, \tag{F.15}$$

and the resulting ferrous hydroxide may subsequently oxidise during exposure to air:

$$4\mathrm{Fe(OH)_2(s)} + \mathrm{O_2} + 2\mathrm{H_2O} \longrightarrow 4\mathrm{Fe(OH)_3(s)}. \tag{F.16}$$

These coupled processes can alter the shape and apparent endpoint of the titration curve. Importantly, oxidation does not by itself imply that the net hydroxide requirement must increase from two to three equivalents per initial mole of Fe^{2+}. The experiment therefore evaluates endpoint reproducibility rather than assigning a unique oxidation stoichiometry.

For the solution stirred overnight, the recorded endpoint was $4.0049\ \mathrm{mL}$:

$$n_{\mathrm{NaOH,total}} = 4.0049(0.0200) = 0.080098\ \mathrm{mmol}, \tag{F.17}$$
$$n^{\mathrm{app}}_{\mathrm{NaOH,Fe^{2+}}} = 0.080098 - 0.042415 = 0.037683\ \mathrm{mmol}, \tag{F.18}$$
$$\nu^{\mathrm{app}}_{\mathrm{Fe^{2+}}} = \frac{0.037683}{0.035610} = 1.058. \tag{F.19}$$

For the unstirred solution, the recorded endpoint was $3.5537\ \mathrm{mL}$:

$$n_{\mathrm{NaOH,total}} = 3.5537(0.0200) = 0.071074\ \mathrm{mmol}, \tag{F.20}$$
$$n^{\mathrm{app}}_{\mathrm{NaOH,Fe^{2+}}} = 0.071074 - 0.042415 = 0.028659\ \mathrm{mmol}, \tag{F.21}$$
$$\nu^{\mathrm{app}}_{\mathrm{Fe^{2+}}} = \frac{0.028659}{0.035610} = 0.805. \tag{F.22}$$

The two nominally identical ferrous solutions therefore differed by

$$\Delta V_{\mathrm{EP}} = 4.0049 - 3.5537 = 0.4512\ \mathrm{mL}, \tag{F.23}$$

equivalent to $0.009024\ \mathrm{mmol}$ NaOH. The acid-corrected apparent coefficients, 1.058 and 0.805, do not correspond to a single well-defined complete-precipitation stoichiometry. The experiment therefore demonstrates that the endpoint of a ferrous-iron-containing sample depends on handling and reaction kinetics.

F.4. Implication for IEC and Iron-Uptake Measurements

Table F.1 summarises the corrected results.

Table F.1: NaOH consumption by the iron-containing dummy solutions after subtraction of the common acid contribution.

Condition	V_{EP} (mL)	n_{Fe} (mmol)	$n^{\mathrm{app}}_{\mathrm{NaOH,Fe}}$ (mmol)	ν^{app} (mol OH^-/mol Fe)
Fe^{3+}, standard	7.4463	0.035514	0.106511	2.999
Fe^{3+}, doubled	12.0847	0.071028	0.199279	2.806
Fe^{2+}, stirred overnight	4.0049	0.035610	0.037683	1.058
Fe^{2+}, unstirred	3.5537	0.035610	0.028659	0.805

The dummy-solution tests demonstrate that NaOH consumption in an iron-containing NaCl extract is not selective for membrane-derived proton equivalents. Ferric iron contributes approximately three hydroxide equivalents per mole under the standard test condition, while the ferrous response is handling-dependent and cannot be represented by one reproducible coefficient. The endpoint therefore depends on the unknown iron concentration, oxidation state, hydrolysis and precipitation behaviour, and sample-handling history.

Consequently, NaOH titration of an iron-containing extract cannot provide an unambiguous measurement of either membrane IEC or retained-iron loading. A single blank subtraction or universal post-hoc correction is not sufficient. This limitation applies specifically to iron-containing extracts; it does not invalidate conventional acid–base IEC titration of iron-free membranes prepared and exchanged under controlled conditions.

For the immersion experiments, retained iron was therefore quantified by UV–Vis spectrophotometry using the 1,10-phenanthroline method described in Section 3.5. All dissolved Fe^{3+} was reduced to Fe^{2+} before complexation, so the measurement reports total dissolved iron. The separate nominally Fe^{2+}-rich and Fe^{3+}-rich immersion conditions were compared using this total-iron measurement. The UV–Vis method therefore avoids the acid–base endpoint interference demonstrated here, although it does not independently resolve the original oxidation state of iron in a mixed extract.

G

Model Verification: Comparison Against Known Analytical Limits and Exploratory Immobile Sink

Before the model is used to interpret experimental resistance data, its numerical implementation is checked against four limiting cases for which the expected behaviour can be predicted from first principles, independent of any fitted parameter. These checks isolate individual terms in the governing equations (diffusion, migration, Faradaic conversion, and the fouling kinetics) one at a time, so that a discrepancy can be traced to a specific mechanism rather than the model as a whole. This is a test of whether the equations have been solved correctly, distinct from the comparison against experimental data presented elsewhere, which tests whether the equations themselves are physically appropriate.

Zero applied current

The membrane flux of each ionic species is described by the Nernst–Planck equation, which combines a diffusive term (driven by the concentration gradient) and a migrative term (driven by the electric field within the membrane):

$$N_i = -D_i \frac{\partial c_i}{\partial x} + z_i D_i \frac{F}{RT} c_i E, \tag{G.1}$$

where N_i is the flux of species i, D_i its effective diffusivity, z_i its valence, c_i its local concentration, and E the electric field within the membrane, taken to be directly proportional to the applied current, $E = i/\kappa$. With no current applied, $E = 0$, and Eq. (G.1) reduces to simple Fickian diffusion,

$$N_i = -D_i \frac{\partial c_i}{\partial x}. \tag{G.2}$$

With no current, no Fe^{2+} is converted to Fe^{3+} or vice versa, so the state of charge in the electrolyte tank is expected to remain essentially constant. A small residual drift is still physically reasonable: Fe^{2+} and Fe^{3+} diffuse at different rates and partition differently under the Donnan equilibrium, so even under pure diffusion the two species can cross over from the tank at slightly different rates, producing a very small change in the tank's state of charge over time.

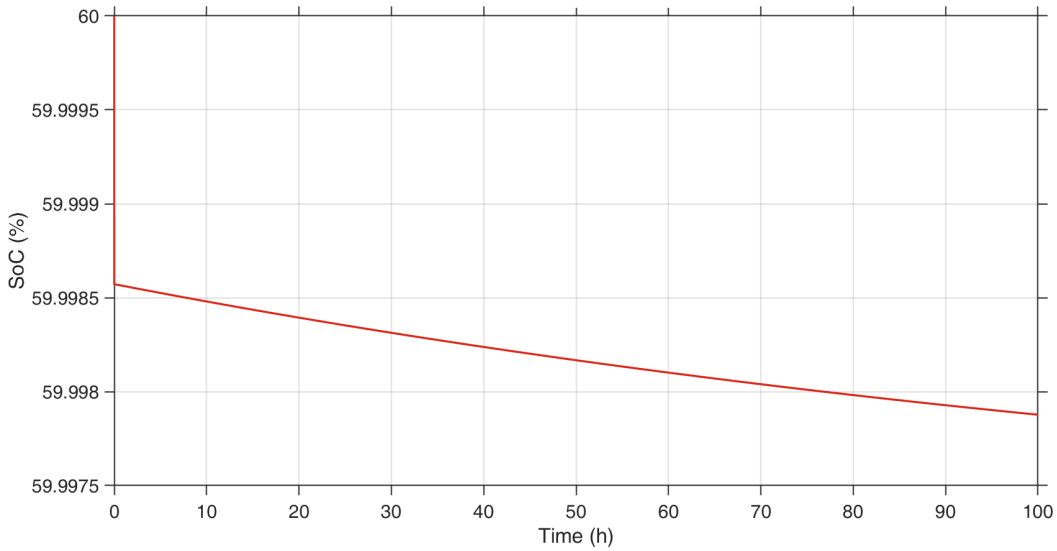


Figure G.1: State of charge in the electrolyte tank over 100 h at zero applied current. The brief initial adjustment corresponds to the holdup reservoir filling from its initial empty state toward a quasi-steady partitioned concentration, and involves only a small fraction of the tank's total iron inventory.

The state of charge changed by only 2.1×10^{-5} (in fractional terms) over 100 h, which is smaller than the relative error tolerance used by the numerical solver. No systematic drift beyond this level was observed, confirming that no unintended charge-transfer reaction occurs in the absence of an applied current.

Membrane thickness scaling

Under pure diffusion, the flux from Eq. (G.1) (with $E = 0$) across a membrane of thickness δ can be approximated, for a quasi-steady linear concentration profile, as

$$N_i \approx D_i \, \frac{c_i^{(0)} - c_i^{(\delta)}}{\delta}, \tag{G.3}$$

where $c_i^{(0)}$ and $c_i^{(\delta)}$ are the concentrations at the two membrane faces. Equation (G.3) predicts that the flux is inversely proportional to the membrane thickness: doubling δ should halve N_i, for an otherwise identical membrane and boundary conditions. This check compares the crossover flux computed for two artificial membrane thicknesses (50 μm and 100 μm), with the applied current held at zero so that only diffusive transport is active.

The ratio of the two computed fluxes was 2.0000, in exact agreement with the value of 2 predicted by Eq. (G.3). This confirms that the diffusive part of the membrane transport model responds correctly to a change in membrane thickness.

Applied-current scaling, charge and discharge

Two independent predictions follow directly from Faraday's law and from the migrative term in Eq. (G.1):

1. Faraday's law states that the charge required to convert a fixed amount of Fe^{2+} to Fe^{3+} (or vice versa) is fixed, so the time needed to reach a given state of charge should be inversely proportional to the applied current: doubling the current should halve the time required.
2. Since $E = i/\kappa$, the migrative term in Eq. (G.1) scales linearly with the applied current, while the diffusive term does not. The migration-driven contribution to the crossover flux should therefore also scale linearly with current: doubling the current should double this contribution.

Both predictions were tested starting from a state of charge of 50%, running the model once toward full charge (SoC $\rightarrow$ 95%) and once toward full discharge (SoC $\rightarrow$ 5%), at applied currents of 25 A and

50 A, to confirm that both behaviours hold in either direction and are not an artefact of one particular current convention.

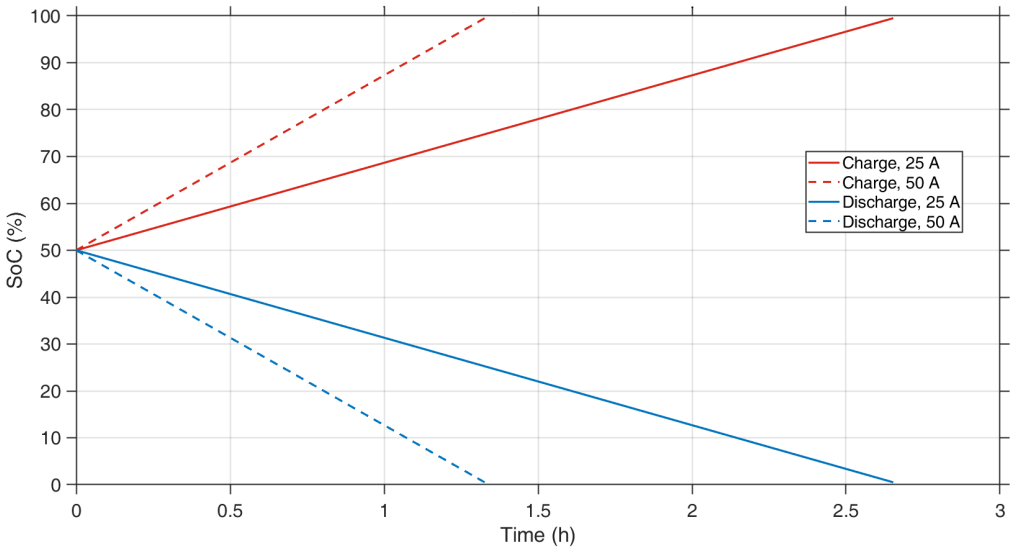


Figure G.2: State of charge versus time for charge and discharge at 25 A and 50 A, starting from SoC $= 50\%$.

Table G.1: Observed time and migratory-flux scaling ratios between 25 A and 50 A, compared against the value of 2 expected from Faraday's law and the linear field–current relationship in Eq. (G.1).

	Time ratio	Migratory flux ratio
Charge	2.047	1.986
Discharge	1.920	1.964

Both ratios agree with the expected value of 2 to within a few percent, in both directions. The small deviations are consistent with the discrete time steps used by the numerical solver rather than any physical or implementation error, and the agreement between the charge and discharge directions indicates that the model treats both directions of current flow consistently.

Blocking rate constant set to zero

The membrane resistance is related to the blocked fraction θ by

$$R(t) = R_0 + \Delta R_{\max}\,\theta(t), \tag{G.4}$$

where θ evolves according to the site-blocking kinetics

$$\frac{d\theta}{dt} = k_{\mathrm{block}}\,C_{\mathrm{Fe},R}\,(1-\theta). \tag{G.5}$$

If the blocking rate constant k_{block} is set to zero, Eq. (G.5) gives $d\theta/dt = 0$ for all time, so θ remains at its initial value of zero throughout the simulation. Substituting $\theta = 0$ into Eq. (G.4) then gives $R(t) = R_0$ for all time, since there is no mechanism by which sites can become occupied.

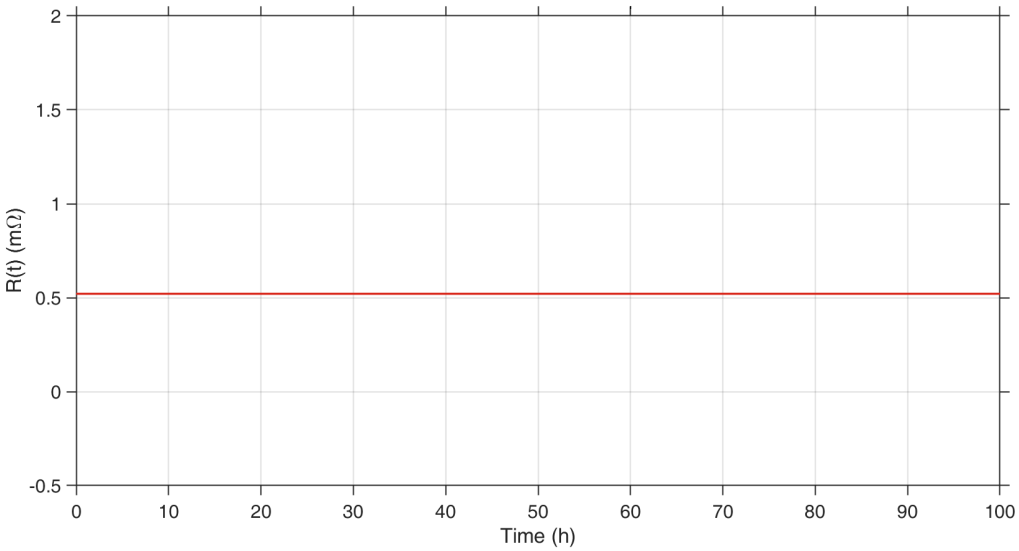


Figure G.3: Resistance versus time over 100 h with $k_{\mathrm{block}} = 0$.

Both θ and the resistance remained unchanged from their initial values throughout the simulation, to within numerical precision, confirming that Eqs. (G.4)–(G.5) were implemented as intended and that the fouling submodel introduces no resistance growth when the blocking rate constant is disabled.

Summary

All four checks reproduced the behaviour expected from the underlying physical principles: no spurious charge-transfer reaction at zero current, correct inverse scaling of diffusive flux with membrane thickness, correct scaling of both reaction time and migratory flux with applied current in both charge and discharge directions, and no fouling-driven resistance growth when the blocking rate constant is switched off. These checks confirm that the governing equations have been implemented correctly, and are complementary to the comparison against experimental resistance data presented in Section 4.5, which addresses whether the equations themselves capture the physical behaviour of the system.

G.1. Exploratory Mobile-to-Immobilised Iron Sink

An exploratory six-state model was evaluated to determine whether explicit removal of iron from the effective hydrogen-side mobile inventory affected the predicted resistance trajectory. The additional state, n_{imm}, was defined by

$$\frac{dn_{\mathrm{imm}}}{d\theta} = n_{\mathrm{Fe},R}, \tag{G.6}$$

where

$$n_{\mathrm{Fe},R} = n_{2,R} + n_{3,R}. \tag{G.7}$$

Combining Equation (G.6) with the resistance-growth relationship gives

$$\frac{dn_{\mathrm{imm}}}{dt} = \frac{k_{\mathrm{block}}}{V_{R,\mathrm{eff}}} n_{\mathrm{Fe},R}^2 \left(1 - \theta\right). \tag{G.8}$$

The corresponding amount was removed from the Fe^{2+} and Fe^{3+} mobile inventories in proportion to their instantaneous mole fractions. The resulting global balance was

$$n_{2,L} + n_{3,L} + n_{2,R} + n_{3,R} + n_{\mathrm{imm}} = \mathrm{constant}. \tag{G.9}$$

The model was run with this mobile-inventory sink both enabled and disabled, while all other inputs and parameters were held constant. The comparison gave

Table G.2: Influence of the exploratory mobile-iron sink on the model–experiment agreement for the common valid comparison interval with $t \geq 80\ \mathrm{h}$.

Case	R^2	NRMSE (%)
Sink enabled	0.9393	6.369
Sink disabled	0.9394	6.365

The corresponding differences, $\Delta R^2 = 0.0001$ and $\Delta\mathrm{NRMSE} = -0.005$ percentage points, are negligible. The sink-enabled formulation produced a final effective immobilised inventory of approximately $1.766\ \mathrm{mmol}$. This value is not interpreted as a quantitative prediction of sulfonate-bound membrane iron because the closure was not independently calibrated, was not constrained by IEC, and did not distinguish Fe^{2+} from Fe^{3+} retention.

The resistance trajectory therefore did not identify or require a separate immobilised-iron state. The sink was consequently omitted from the nominal model in accordance with model parsimony, and the reported principal model output is the effective resistance-growth state $\theta(t)$.

H

Additional data and figures

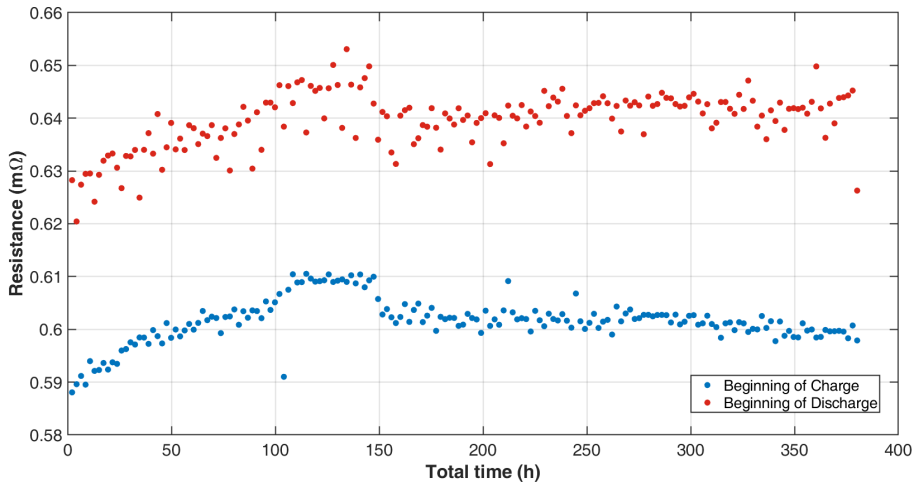


Figure H.1: Resistance evolution recorded for the NR212 stack, showing anomalous behavior possibly attributed to a valve and system faults during the experiment. Due to this, the dataset was excluded from the main analysis.

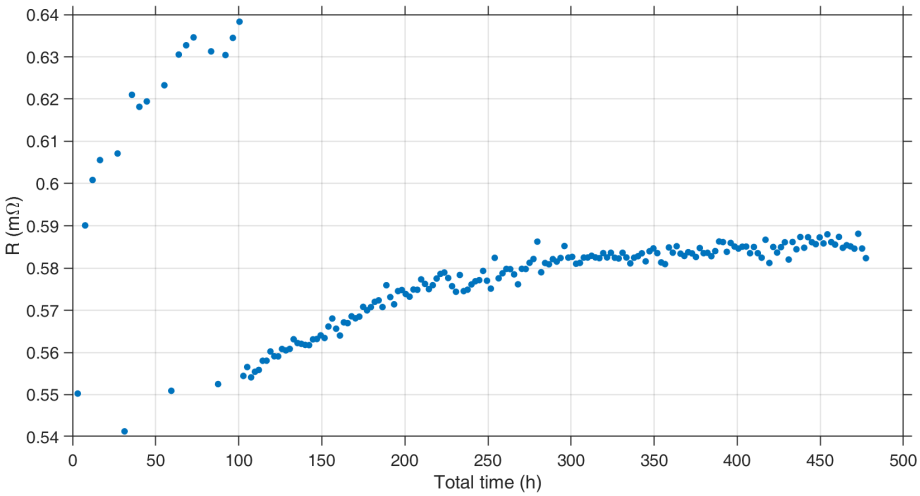


Figure H.2: Resistance evolution recorded for the Membrane X , showing the resistance during initial lower power cycles at 35W. Due to this issue, the initial dataset was excluded from the main analysis.

Membrane	Dry mass (g)	Conc. from UV-Vis (M)	Total Fe (mmol)	Fe uptake (mmol g^{-1})
Membrane X	0.1754	0.00205	0.1025	0.584
NR212	0.7777	0.00195	0.0975	0.125

Table H.1: UV-Vis-derived Fe uptake for the NR212 and Membrane X samples collected from the affected stacks (Section 3.2.7). Values are provided for completeness; not used for quantitative analysis due to the unreliability of the source samples.

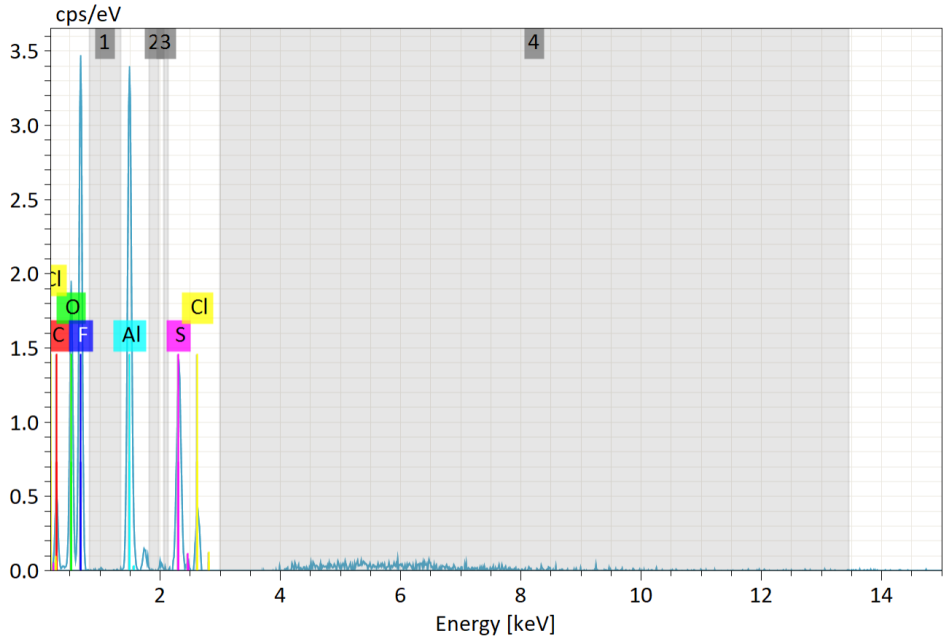


Figure H.3: EDS spectrum of Spectrum 1, the particulate visible in Figure 4.5a (pristine NR212), containing Al, S, and Cl. This feature is attributed to external contamination.

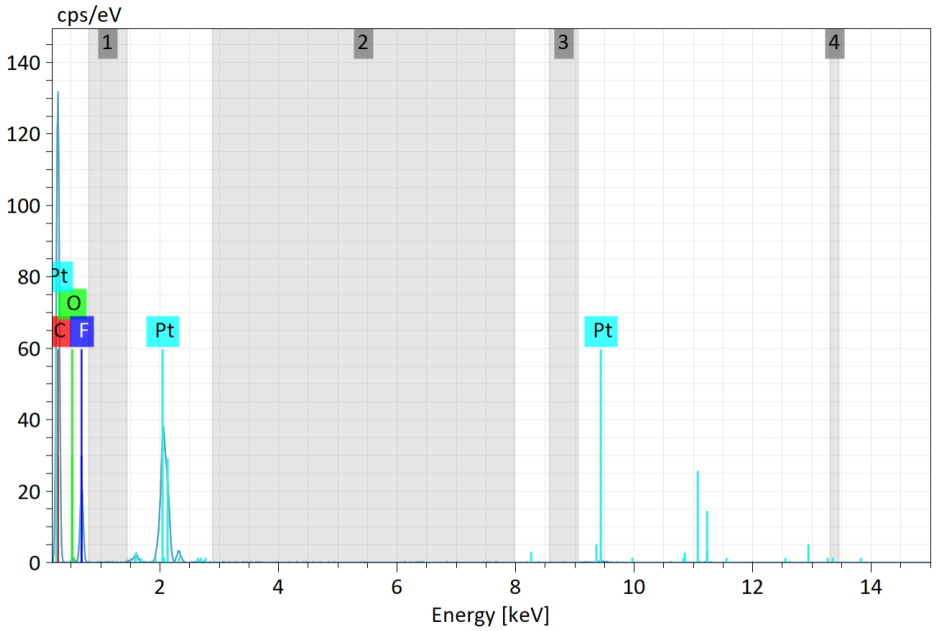


Figure H.4: EDS spectrum of Spectrum 1, a Pt/S-bearing particulate visible in Figure 4.7a (cycled NR212, Field 2), consistent with the catalyst-derived contamination reported in Figure 4.6.

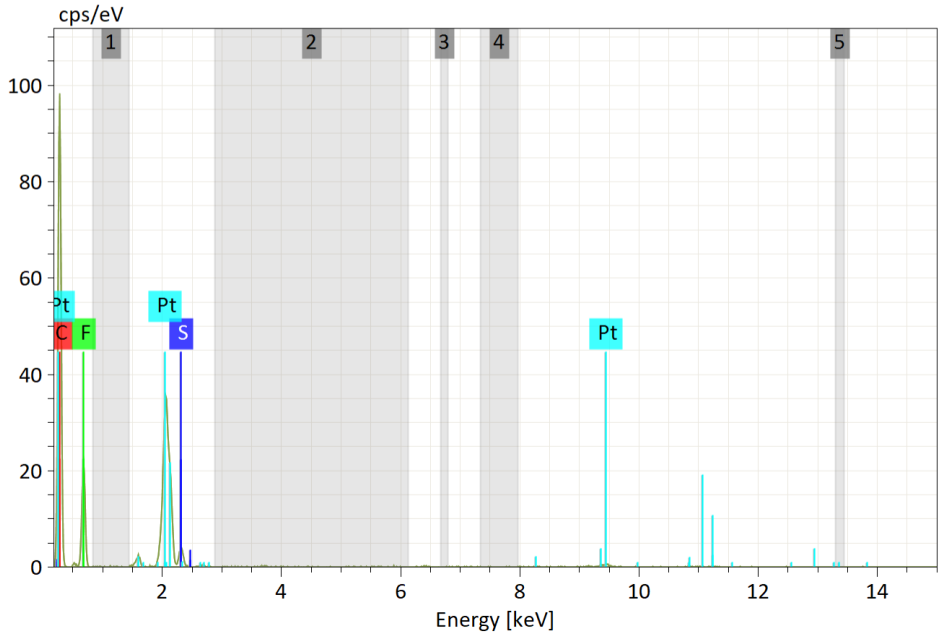


Figure H.5: EDS spectrum of Spectrum 2, a Pt/S-bearing particulate visible in Figure 4.7a (cycled NR212, Field 2), consistent with the catalyst-derived contamination reported in Figure 4.6.

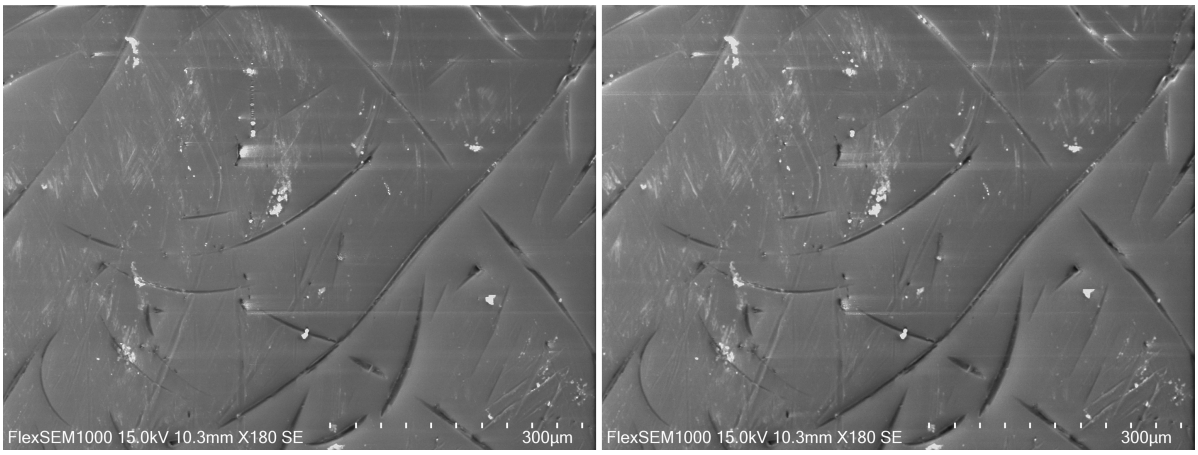
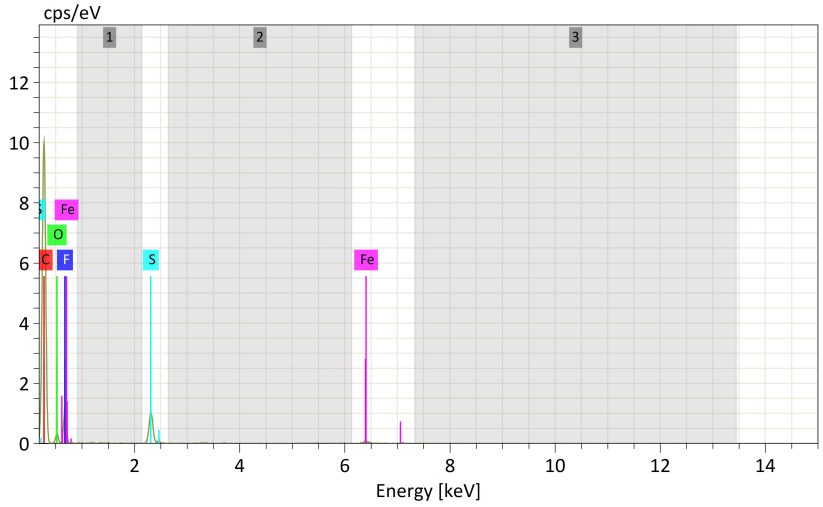
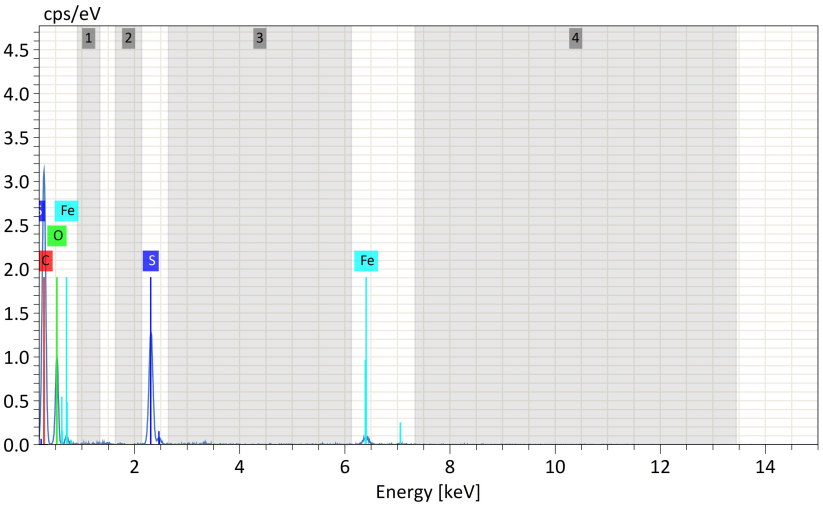


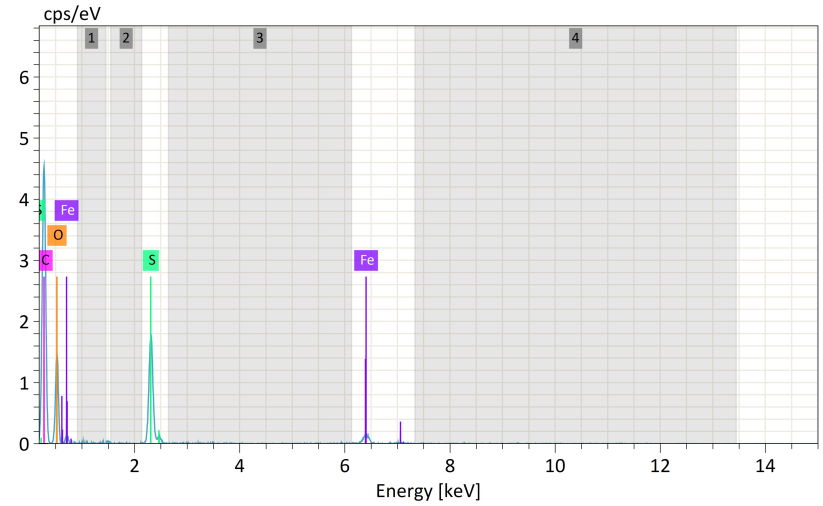
Figure H.6: Secondary-electron images of the same field of view on Membrane X, acquired consecutively (15 kV, 180×). Left: first acquisition. Right: second acquisition.



(a) Spectrum 1

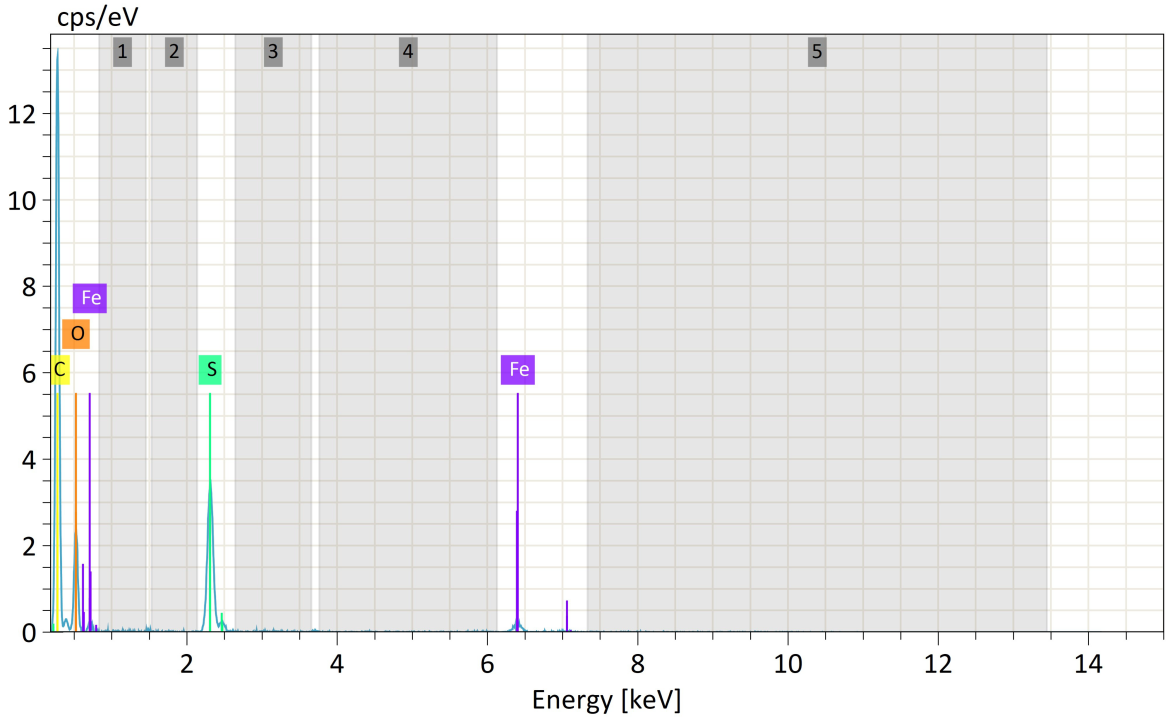


(b) Spectrum 4

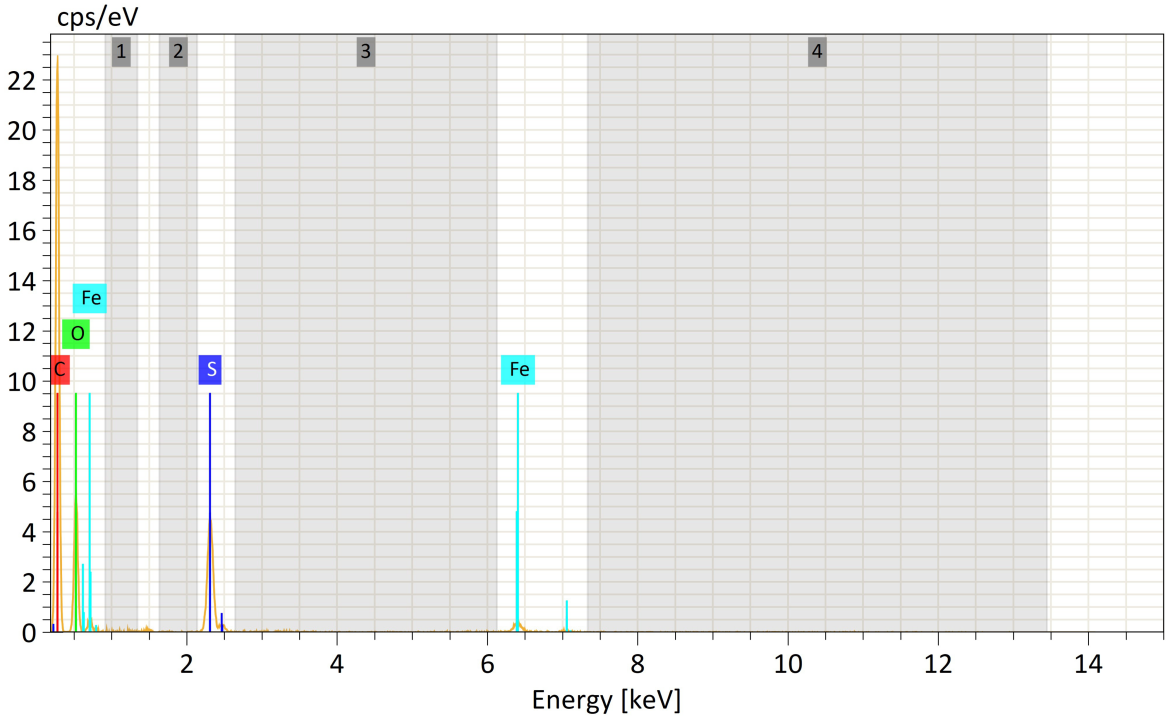


(c) Spectrum 5

Figure H.7: Remaining EDS point spectra from Field 1 of fouled Membrane X; SEM context for this field is shown in Figure 4.9a. Spectrum 1 is the only point in the full dataset with a detectable F signal (F 6.70 at%, Fe 0.35 at%). Spectra 4 and 5 are plain C/O/S-dominated matrix points (Fe 0.83 and 1.01 at%, respectively), consistent with Spectra 2 and 3 of the same field shown in Figure 4.9.

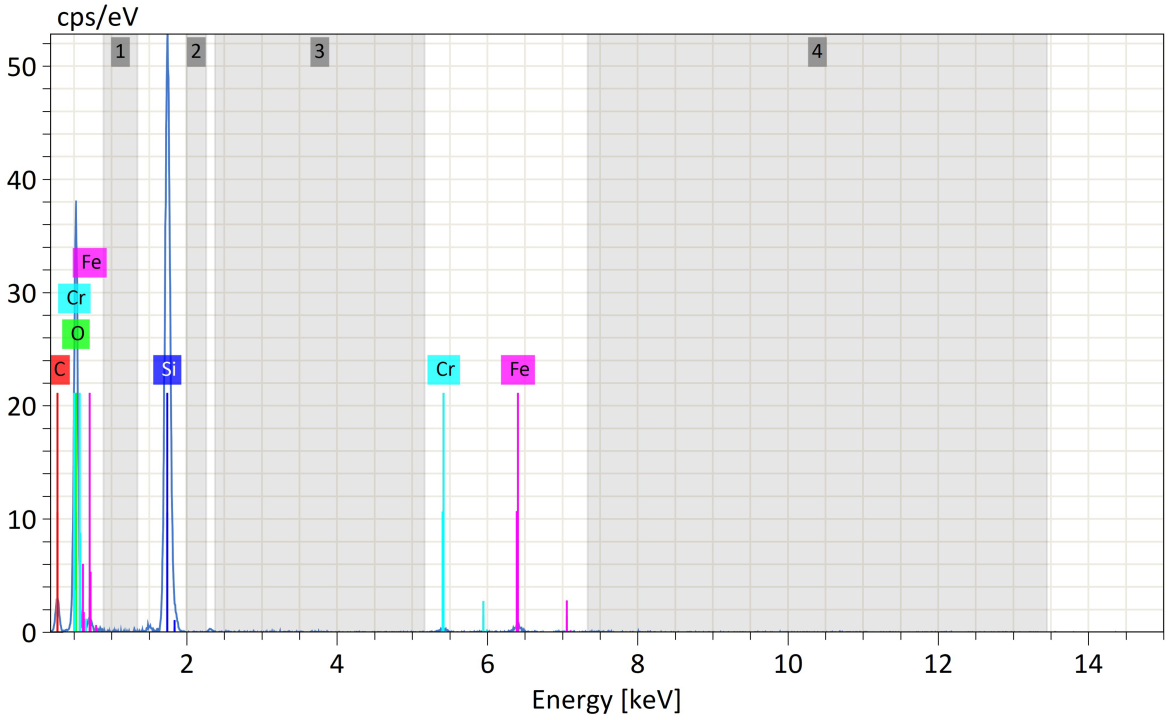


(a) Spectrum 1

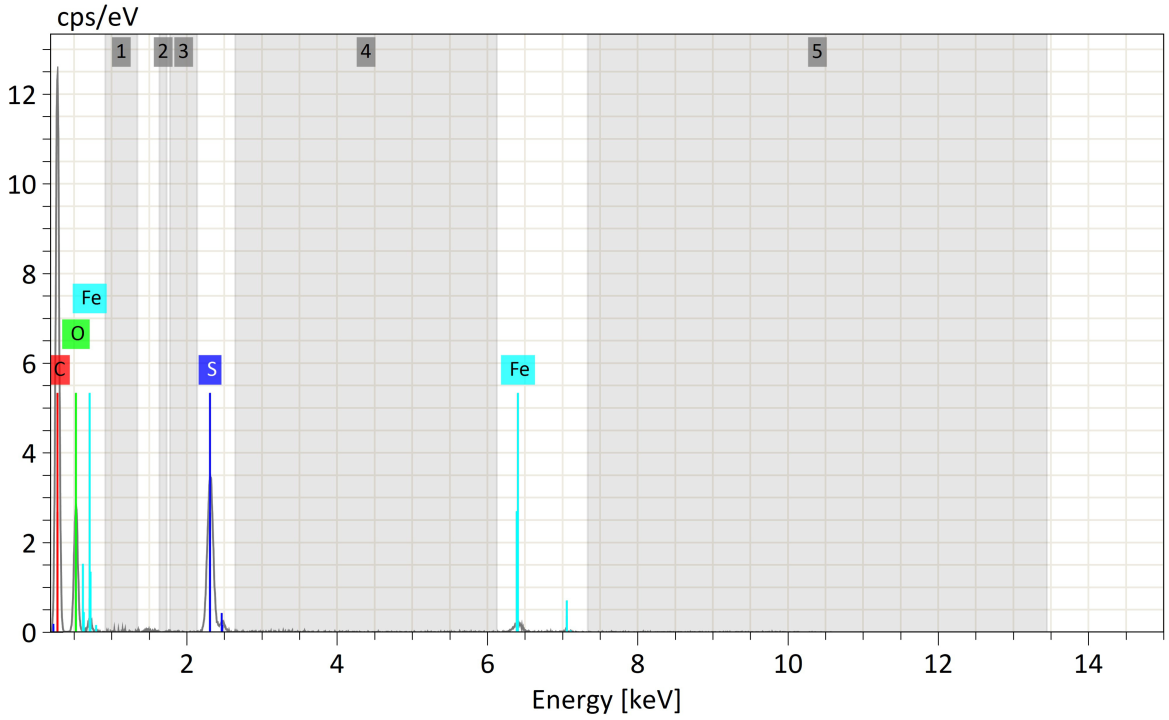


(b) Spectrum 4

Figure H.8: Remaining EDS point spectra from Field 3 of fouled Membrane X (part 1 of 2); SEM context for this field is shown in Figure 4.10a. Spectra 1 and 4 are plain C/O/S-dominated matrix points (Fe 0.73 and 0.80 at%, respectively).



(a) Spectrum 5



(b) Spectrum 6

Figure H.9: Remaining EDS point spectra from Field 3 of fouled Membrane X (part 2 of 2). Spectrum 5 is the Si-contaminated point discussed in Section 4.2.2 (Si 18.81 at%, Cr 0.38 at%, Fe 0.95 at%, unnormalized sum 119.48%), attributed to an external contaminant rather than an iron-bearing deposit. Spectrum 6 is a plain matrix point (Fe 0.80 at%).

Field	Pt.	C	O	F	S	Ca	Si	Cr	Fe	Sum (raw, %)
1	1	87.72	4.13	6.70	1.09	–	–	–	0.35	100.00
1	2	73.63	24.09	–	1.56	0.20	–	–	0.52	100.00
1	**3**	**74.07**	**23.11**	–	**2.14**	–	–	–	**0.68**	**100.00**
1	4	74.98	21.68	–	2.51	–	–	–	0.83	100.00
1	5	74.68	21.89	–	2.42	–	–	–	1.01	100.00
2	1	74.21	24.63	–	0.92	–	–	–	0.24	100.00
2	2	74.24	23.71	–	1.64	–	–	–	0.42	100.00
2	3	69.18	27.66	–	2.35	–	–	–	0.81	100.00
2	4	72.66	24.69	–	1.96	–	–	–	0.69	100.00
2	5	71.98	25.51	–	1.86	–	–	–	0.65	100.00
3	**1**	**35.28**	**50.81**	**0.00**	**7.54**	–	–	–	**6.37**	**45.95**
3	2	78.24	18.59	–	2.44	–	–	–	0.73	100.00
3	3	73.43	20.15	–	4.44	–	–	–	1.98	61.71
3	4	74.47	22.74	–	2.12	–	–	–	0.66	100.00
3	5	74.13	23.14	–	1.94	–	–	–	0.80	100.00
3	6	22.59	57.28	–	–	–	18.81	0.38	0.95	119.48
3	7	75.70	21.08	–	2.42	–	–	–	0.80	100.00

Table H.2: Full EDS point spectrum dataset for fouled Membrane X (17 points, 3 fields of view). Values are atomic percent (at.%), normalized basis. “Sum (raw)” is the unnormalized mass total prior to renormalization; values below 100% indicate degraded X-ray collection. Dashes: element not detected. Bold rows: spectra presented in full in Section 4.2.2. Field 3, Point 6 shows a high Si signal, indicating an unrelated contamination particle.

Sample	m_{dry} (g)	$m_{\mathrm{wet},1}$ (g)	$m_{\mathrm{wet},2}$ (g)	$m_{\mathrm{wet},3}$ (g)	$\bar{m}_{\mathrm{wet}}$ (g)	WU (%)
1	0.1241	0.2071	0.2063	0.2022	0.2052	65.35
2	0.1110	0.1854	0.1841	0.1807	0.1834	65.23
3	0.0869	0.1560	0.1429	0.1467	0.1485	70.92
4	0.1039	0.1756	0.1704	0.1735	0.1732	66.67
5	0.0841	0.1492	0.1435	0.1406	0.1444	71.74
					Mean WU	68%

Table H.3: Water uptake measurements for Membrane X. Five samples were pre-treated per supplier recommendation, dried at 80 °C overnight, and soaked in ultrapure water for at least 4 hours between each wet mass measurement. The water uptake of each sample is calculated from the average of the three wet mass readings; the reported value is the mean across all five samples.

Sample	m_{dry} (g)	n_{NaOH} (mmol)	IEC (meq g^{-1})
1	0.2223	0.3156	1.42
2	0.1719	0.2762	1.61
3	0.1815	0.2686	1.48
4	0.2058	0.2990	1.45
5	0.1894	0.2612	1.38
		Mean IEC	1.47

Table H.6: Ion exchange capacity measurements for CMVN.

Sample	m_{dry} (g)	$m_{\mathrm{wet},1}$ (g)	$m_{\mathrm{wet},2}$ (g)	$m_{\mathrm{wet},3}$ (g)	$\bar{m}_{\mathrm{wet}}$ (g)	WU (%)
1	0.4034	0.5241	0.5283	0.5189	0.5238	29.84
2	0.3741	0.4878	0.4807	0.4847	0.4844	29.48
3	0.4621	0.5916	0.5919	0.5938	0.5924	28.20
4	0.3799	0.4819	0.4740	0.4799	0.4786	25.98
5	0.3853	0.4956	0.4748	0.4848	0.4851	25.89
					Mean WU	28%

Table H.4: Water uptake measurements for CMVN. Five samples were dried at 80 °C overnight, and soaked in ultrapure water for at least 4 hours between each wet mass measurement. The water uptake of each sample is calculated from the average of the three wet mass readings; the reported value is the mean across all five samples.

Sample No.	Mass of sample (g)	
	NR212	Membrane X
1	0.0774	0.0178
2	0.0775	0.0168
3	0.0764	0.0178
4	0.0776	0.0170
5	0.0778	0.0177
6	0.0785	0.0178
7	0.0773	0.0173
8	0.0782	0.0175
9	0.0789	0.0180
10	0.0781	0.0177
Average	0.07777	0.01754
Area density (g cm^{-2})	0.009699	0.002188

Table H.5: Area density of Nafion NR212 and Membrane X, determined from circular punched samples of diameter 3.195 cm (area $= 8.018\ \mathrm{cm}^2$). The resulting area density and dry mass are used to determine the iron uptake in the membrane samples from the stack (mol $\mathrm{g}_{\mathrm{dry}}^{-1}$).

Listing H.1: MATLAB implementation of the saturating exponential fit (Equation 3.6) applied to the in-situ BOC resistance data.

```
clc; clear; close all;

data  = readtable('data.xlsx');

x_raw = data{:,2};
y_raw = data{:,4};

valid = ~isnan(x_raw) & ~isnan(y_raw);
x = x_raw(valid);
y = y_raw(valid);

model_exp = @(p, x) p(1) + p(2) .* (1 - exp(-p(3) .* x));

p0 = [y(1), y(end)-y(1), 1/x(end)];

opts = optimoptions('lsqcurvefit', ...
    'Display',                  'iter', ...
    'TolFun',                   1e-10,  ...
    'TolX',                     1e-10,  ...
    'MaxFunctionEvaluations',   5000);

lb = [0, 0, 0];
ub = [inf, inf, inf];

p_exp = lsqcurvefit(model_exp, p0, x, y, lb, ub, opts);

y_pred   = model_exp(p_exp, x);
R2_exp   = 1 - sum((y-y_pred).^2) / sum((y-mean(y)).^2);
RMSE_exp = sqrt(mean((y-y_pred).^2));

x_fine = linspace(min(x), max(x)*1.1, 500);
y_fine = model_exp(p_exp, x_fine);

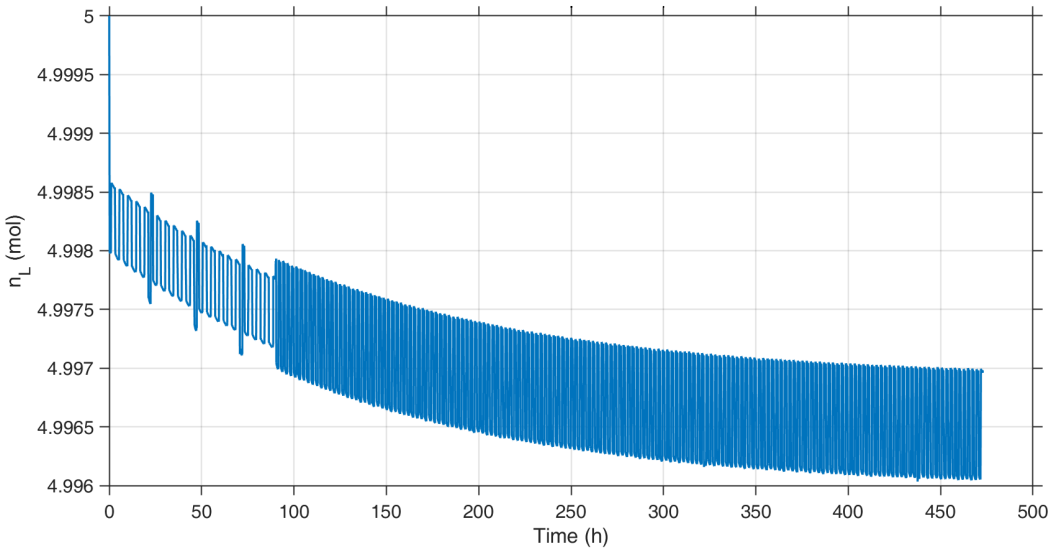
y_mOhm      = y * 1000;
y_fine_mOhm = y_fine * 1000;

c1 = [0.00 0.45 0.74];
c2 = [0.85 0.15 0.10];

figure('Name', 'Exponential saturation fit');
scatter(x, y_mOhm, 50, c1, 'filled'); hold on;
plot(x_fine, y_fine_mOhm, '-', 'Color', c2, 'LineWidth', 2);
xlabel('Total time (h)');
ylabel('R (m\Omega)');
legend('Data', 'Fitted curve', 'Location', 'best');
grid on;

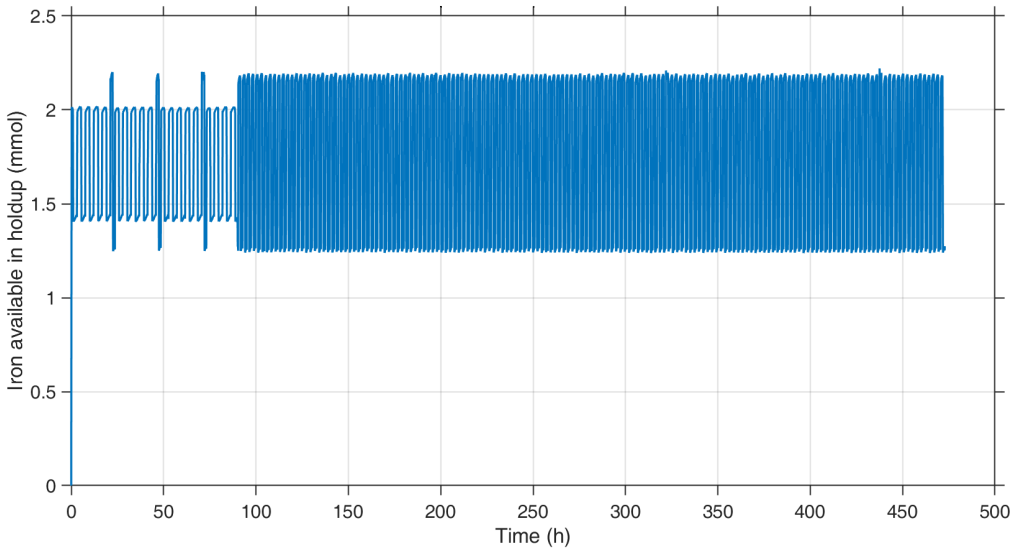
tau  = 1 / p_exp(3);
t_99 = -log(1 - 0.99) / p_exp(3);

theta_now = (y(end) - p_exp(1)) / p_exp(2);
```

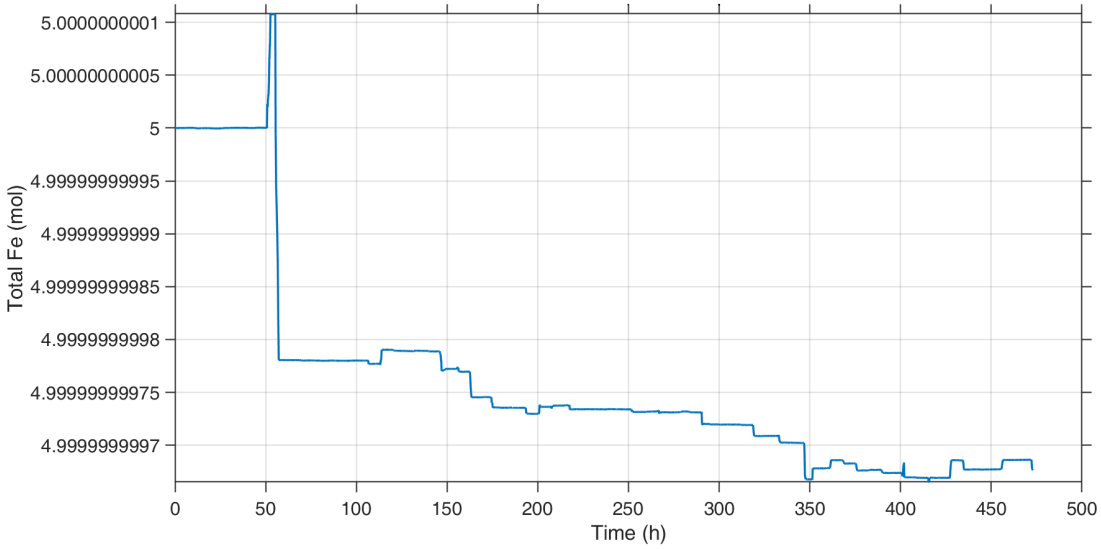


(a) Liquid-phase Fe holdup n_L.

Figure H.10: Model verification checks on Fe mass conservation and holdup dynamics (part 1 of 2).



(a) Fe available in membrane holdup.



(b) Total Fe mass balance.

Figure H.11: Model verification checks on Fe mass conservation and holdup dynamics (part 2 of 2).

Declaration of the use of AI tools

In the course of developing this project report, various digital tools, including Artificial Intelligence (AI)-powered assistants, data analytics software, and modeling environments, were utilized to enhance the quality, precision, and coherence of the deliverables. The use of these tools was guided by academic integrity, transparency, and the goal of producing technically rigorous and professionally formatted outcomes.

AI tools, such as natural language generation models, were selectively employed to assist with the structuring and refinement of complex technical sections, LaTeX formatting, and generation of well-formulated academic prose. These tools functioned as language and structure aids, helping to translate complex ideas into clear, well-organized text. AI-assisted tools were additionally used during the development of the Matlab-based transport and fouling models presented in this work, primarily for code structuring, syntax troubleshooting, and debugging support.

The adoption of such tools is in line with modern engineering practice and reflects the evolving role of AI in supporting technical communication, coding, and research productivity. Similar tools are increasingly used in professional engineering environments to streamline reporting, optimize documentation, and improve collaboration.

Ultimately, the integration of AI and software tools contributed to a clearer and more professional report, without compromising academic standards or the integrity of the research.